Cellular Dynamical Mean-field Theory in large Impurity Clusters

Dissertation

der Mathematisch-Naturwissenschaftlichen Fakultät

der Eberhard Karls Universität Tübingen

zur Erlangung des Grades eines

Doktors der Naturwissenschaften

(Dr. rer. nat.)

vorgelegt von

Marcel Klett

aus Ludwigsburg

Tübingen

2020

Gedruckt mit Genehmigung der Mathematisch-Naturwissenschaftlichen Fakultät der Eberhard Karls Universität Tübingen.

Tag der mündlichen Qualifikation:	20.10.2020
Stellvertretender Dekan:	Prof. Dr. József Fortágh
1. Berichterstatter:	Prof. Dr. Sabine Andergassen
2. Berichterstatter:	Prof. Dr. Giorgio Sangiovanni

EBERHARD KARLS
UNIVERSITÄT
TÜBINGEN

Dissertation

Cellular Dynamical Mean-field Theory in large Impurity Clusters

Eingereicht von:

Marcel Klett

November 24, 2020

Hauptberichter: Prof. Dr. Sabine Andergassen
Mitberichter: Prof. Dr. Giorgio Sangiovanni

Institut für Theoretische Physik
Universität Tübingen
Auf der Morgenstelle 14, 72076 Tübingen

Abstract

Even after decades of intense research, the single band Hubbard model representing the fundamental model for interacting quantum systems and electronic correlations remains an unsolved cornerstone paradigm in theoretical solid state physics. Within the non-perturbative dynamical mean-field theory (DMFT), the lattice problem is mapped to a self-consistent auxiliary quantum impurity model leading to a local approximation of the self-energy. Nonlocal correlations can be included by the real-space cluster extension of the DMFT (CDMFT). Enlarging the unit cell makes the calculation of a numerically exact solution in CDMFT very challenging. We here use a quantum Monte-Carlo approach in the imaginary-time space in order to solve the self-consistency equations for different cluster sizes. In order to restore the broken translational symmetry re-periodization schemes for the Green function, the self-energy, or its cumulants have been introduced. However, these suffer from ambiguity and may even lead to convergence problems when attempted inside the self-consistency loop. The comparison to numerically exact diagrammatic quantum Monte Carlo calculations shows that introducing a so-called centerfocused extrapolation (CFE) to approximate the lattice self-energy yields very accurate results. Moreover, the CFE converges faster with the cluster size than previous periodization schemes. We here perform a detailed CDMFT analysis for the single-band Hubbard model on the 2D square lattice, reaching real-space cluster sizes of up to 9×9 sites. In addition to spectral properties, we also compute two-particle correlation functions which are not accessible in DMFT. Using benchmarks against diagrammatic Monte Carlo at high temperature, we show that the cluster spin susceptibility can be extrapolated to the exact result at large cluster size. In particular, the exponential decay of spin-spin correlations is very well captured by CDMFT calculations, even when correlations extend beyond the size of the cluster. We further present results at lower temperature T and larger U than the range currently accessible with diagrammatic Monte Carlo methods techniques. The CDMFT+CFE represents therefore a powerful computational tool to access the physics of non-local correlations beyond dynamical mean-field theory.

Zusammenfassung

Auch nach Jahrzehnten intensiver Bemühungen bleibt das Einband-Hubbard-Modell, eines der fundamentalen Modells zur Beschreibung eines wechselwirkenden Quantensystems sowie Elektron-Elektron Korrelationen, ein ungelöstes Paradigma in der theoretischen Physik der kondensierten Materie. Mit Hilfe der nichtpertubativen dynamischen Zentralfeldtheorie (DMFT), wird das Gitterproblem auf ein selbstkonsistentes quanten Stoerstellenmodell projiziert, was eine lokale Näherung für die Selbstenergie liefert. Nicht lokale Korrelationen können durch eine Realraumvergrößerung der DMFT Methode (CDMFT) miteinbezogen werden. Das Vergrößern der Einheitszelle macht die Berechnung der numerisch exakten Lösung in CDMFT jedoch sehr anspruchsvoll. In dieser Arbeit benutzen wir einen quanten Monte-Carlo Ansatz, um die Selbstkonsistenz Gleichung der CDMFT für verschieden große Einheitszellen zu lösen. Um die gebrochene Translationsinvarianz wiederherzustellen, werden Reperiodisierungsmethoden für die Greensfunktion, die Selbstenergie und die sogennanten Kumulanten eingeführt. Diese sind jedoch nicht eindeutig und können im schlimmsten Fall auch zu Konvergenzproblemen führen, wenn diese Reperiodisierungsmethoden innerhalb der Selbstkonsistenzgleichung benutzt werden. Der Vergleich mit numerisch exakten diagrammatischen Monte-Carlo Berechnungen zeigt, dass die in dieser Arbeit eingeführte Reperiodisierungsmethode (CFE) der Selbstenergie sehr gute Übereinstimmung liefert. Zudem konvergiert die CFE Methode schneller in der Größe der Einheitszelle als andere, zuvor bekannte Reperiodisierungsmöglichkeiten.

In dieser Arbeit führen wir eine detaillierte Analyse der CDMFT Methode des Einband-Hubbard-Modells in zwei Dimensionen durch und erreichen dabei Einheitszellen bis zu der Größe 9×9. Zusätzlich zu spektralen Eigenschaften berechnen wir außerdem auch Zweiteilchen-Korrelationsfunktionen die nicht in DMFT berechnet werden können. Durch das Vergleichen von diagrammatischen Monte-Carlo Datenpunkte bei hohen Temperaturen können wir zeigen, dass die Cluster Spinsuszeptibilität zur exakten Lösung führt, sofern man sie zu unendlich großen Einheitszellen extrapoliert. Insbesondere wird der exponentielle Zerfall der Spin-Spin Korrelationen sehr gut durch CDMFT Rechnungen beschrieben, auch dann wenn Korrelationen längerreichweitig sind als das Cluster selbst. Außerdem zeigen wir Resultate für tiefere Temperaturen und größere Wechselwirkungen, als im Moment mit Hilfe der diagrammatischen Monte-Carlo Berechnung möglich sind. Die CDMFT+CFE Methode verkörpert damit ein mächtiges Werkzeug um die Phyisk der nichtlokalen Korrelationen, weit über die Möglichkeiten der DMFT hinaus, zu beschreiben.

Contents

I. Introduction

Interacting electrons in solids can lead to a lot of exciting physical phenomena like superconductivity, ferro- or anti-ferromagnetism and the so-called Mott insulator. All of the afore mentioned effects are due to the electrons being highly correlated which means we cannot treat the system as an ensemble of independent particles. Moreover, we have to take into account the fermionic correlation of the electrons. The electron-electron interactions in the Hamiltonian, even in the most simple way, like in the Kondo or Hubbard lattice model are not analytically solvable in two or higher dimensions. In recent years a lot of effort was put into developing new approaches to tackle this problem numerically. The dramatic increase in computational power in the last decades, lead to increasingly sophisticated approaches to describe interacting electrons in solids. One approximation method of handling the many-body Hamiltonian of electrons in solids is the so-called Dynamical mean-field theory (DMFT) [1]. Even though this theory becomes exact only by treating infinite dimensions, it still can describe different phases found in the Hubbard model like the Mott insulating phase (paramagnetic insulator) or the antiferromagnetic (ordered) phase in two-dimensions shown in figure 1.1. There are different

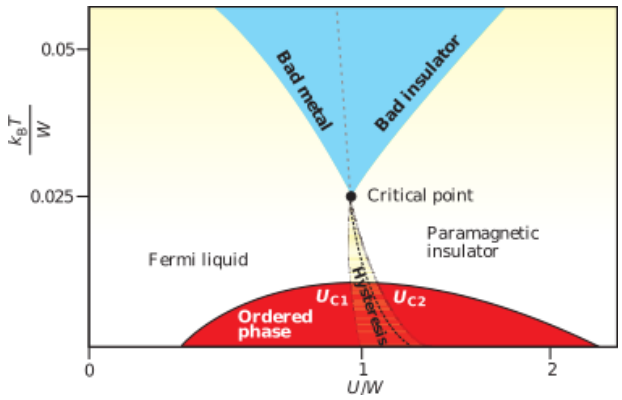

FIGURE 1.1.: Phase diagram of the two-dimensional Hubbard model obtained by using DMFT. Taken from [2].

ways to numerically solve the DMFT self-consistency: Besides the exact diagonalization, which is limited due to the exponential growth of the Hilbert space of the system, the most common way of finding a solution is the numerically exact quantum Monte-Carlo (QMC) approach. Over the years the QMC algorithms improved drastically, leading to more stable solutions in the lower temperature regime. Besides the success of low temperature DMFT solutions, a variety of proposals [3] were introduced to overcome the locality of the initial DMFT idea and to access the physics of non-local correlations. In general those extensions can be divided into two classes, diagrammatic approaches like DΓA [4–8], dual fermions [9–11], dual bosons [12] or ohter mehtods [13–21] and cluster extensions, e.g in momentum space (DCA) [22–24] or cellular dynamical mean-field theory (CDMFT) [25–27] which expands the unit cell used in DMFT in real space.

In this work we answer the question of how non-local correlations included in CDMFT calculations affects observables on the one- and two-particle level. To do this we investigate

calculations with different cluster sizes and analyze their effects on the two-dimensional Hubbard model.

The work is structured in the following way: In chapter II we introduce and discuss the methods and numerical tools needed to understand the results presented in this work. In chapter III we show one-particle results for the two-dimensional Hubbard model within the DMFT framework, where besides a discussion of the Mott metal-to-insulator (MIT) and a phase diagram for the anti-ferromagnetic transition, also calculations away from half-filling are discussed. In the next part of this work we introduce the real-space extension of the DMFT method, the so-called CDMFT framework. The first part of this chapter consists of comparing results on the one-particle level, like the MIT and the anti-ferromagnetic phase diagram for different cluster sizes, with DMFT. The next part includes a new periodization method based on a combination of an infinite size cluster extrapolated self-energy and a center-focussed approach neglecting unwanted border effects inside the cluster, which we call CFE-method. Its description, advantages and benchmarks with numerically exact diagrammatic Monte-Carlo data is not only presented in this part of this work, but represents also an essential part of the publication [28]. The last part of the chapter contains a discussion of the dynamical two-particle properties of the spin-spin and the charge-charge susceptibility. Besides showing real-space data inside the cluster, we also extend the introduced extrapolation scheme to the two-particle level to further enhance our results like done also for the one-particle level. In chapter V we present CDMFT results for the Hubbard model on a two-dimensional triangular lattice. We also discuss a CDMFT unit cell of the triangular lattice we also discuss the influence of non-local correlations by comparing DMFT with CDMFT results on the one-particle level. In the last chapter VI a summary of this work is given, as well as an outlook to potential future applications of the CFE method.

II. Methods and theory

In the present chapter we introduce the formalism of the used methods providing their theoretical background.

1. The Green's function formalism

In general Green's functions are used in the theory of solving ordinary and partial differential equations. In many-particle physics we can define a single-particle Green's function

$$G(\boldsymbol{r}\sigma t, \boldsymbol{r}'\sigma' t') = -\mathrm{i}\Theta(t-t') \left\langle \left[\psi_\sigma(\boldsymbol{r},t)\psi^\dagger_\sigma(\boldsymbol{r}',t')\right]_{B/F} \right\rangle \tag{2.1}$$

with the Heaviside stepfunction $\Theta(x)$ and the definition of the anti-/commutator

$$[\alpha,\beta]_B = [\alpha,\beta] = \alpha\beta - \beta\alpha \tag{2.2a}$$

$$[\alpha,\beta]_F = \{\alpha,\beta\} = \alpha\beta + \beta\alpha \tag{2.2b}$$

where the shortcuts are given by B for bosons and F for fermions. In the definition of the Green's function of equation (2.1) the field operator $\psi_\sigma(\boldsymbol{r},t)$ appear, this opperator annihalites a particle with spin σ at position $\boldsymbol{r}$ and time t, whereas the conjugated operator creates a particle.

A famous case encountered in theory is the Green's function of noninteracting electrons. In this case the Hamiltonian in momentum space reads

$$H = \sum_{k,\sigma} \varepsilon_k c^\dagger_{k,\sigma} c_{k,\sigma} \tag{2.3}$$

and is obviously diagonal in the k-space representation and therefore the fourier transformation of the Green's function (2.1) is as well

$$G(\boldsymbol{k}\sigma, t-t') = -\mathrm{i}\left\langle c_{\boldsymbol{k},\sigma}(t) c^\dagger_{\boldsymbol{k},\sigma}(t') \right\rangle \ . \tag{2.4}$$

In equation (2.4) we implied translational invariance of the system by taking into account that the Green's function in real space only depends on the relative distance of the two particles $|\boldsymbol{r}-\boldsymbol{r}'|$. We can rewrite the Green's function of noninteracting electrons in terms of using a full set of eigenstates $\{|n\rangle\}$ of the full Hamiltonian to obtain the so called *Lehmann representation*.

$$G(\nu,\omega) = \frac{1}{Z}\sum_{n,n'} \frac{\langle n|c_\nu|n'\rangle \langle n'|c^\dagger_\nu|n\rangle}{\omega + E_n - E_{n'} + \mathrm{i}\eta} \left(\mathrm{e}^{-\beta E_n} + \mathrm{e}^{-\beta E_{n'}}\right) \tag{2.5}$$

In equation (2.5) we included the partition function

$$Z = \mathrm{tr}\, \mathrm{e}^{-\beta H} \ , \tag{2.6}$$

as well as the small parameter $\eta \to 0$. If we define the spectral function A to be

$$A(\omega,\nu) = -2\mathrm{Im}G(\nu,\omega) \ , \tag{2.7}$$

we can use the Lehmann representation to get the relation

$$G(\omega,\nu) = \int \frac{\mathrm{d}\omega'}{2\pi} \frac{A(\nu,\omega)}{\omega - \omega' + \mathrm{i}\eta} \ . \tag{2.8}$$

1.1. Imaginary-Time Green's function

The Green's function formalism is often used in order to determine physical observables. In this subsection we will introduce a mathematical method which will map the time to an imaginary variable $t \to \mathrm{i}\tau$. This mapping has no physical meaning, but is helpful to deal with perturbation theories which are a quintessential method in correlated many-body physics for finite temperatures. Analogous to the retarded Green's function in real-time of equation (2.4) we can define an imaginary-time Green's function, also called Matsubara Green's function

$$G(\nu, \tau, \mu, \tau') = -\left\langle T_\tau c_\nu(\tau) c_\mu^\dagger(\tau') \right\rangle \,, \tag{2.9}$$

where T_τ is the time-ordering operator defined as

$$T_\tau c_\alpha(\tau) c_\beta^\dagger(\tau') = \begin{cases} c_\alpha(\tau) c_\beta^\dagger(\tau'), & \tau > \tau' \\ \pm c_\beta^\dagger(\tau') c_\alpha(\tau), & \tau' > \tau \end{cases} \,, \tag{2.10}$$

here $\pm$ refers to the bosonic case (plus) and fermionic case (minus). The imaginary-time has the properties of $0 < \tau$ and $\tau' < \beta$. The inverse temperature is defined as

$$\beta = \frac{1}{k_B T} \,, \tag{2.11}$$

with the Boltzman constant k_B. The time dependence t of operators is now shifted to operators dependent on the imaginary time τ. According to the Heisenberg picture we can shift the τ dependence of an operator $A(\tau)$ into an unitary operator $U(\tau)$ in the following way

$$A(\tau) \equiv U(\tau) A U^\dagger(\tau) = \mathrm{e}^{\tau H} A \mathrm{e}^{-\tau H} \,. \tag{2.12}$$

For a time independent Hamiltonian the imaginary-time Green's function only depends on the time difference of $\tau - \tau'$ in which case we can rewrite equation (2.9) to

$$G(\nu, \tau, \mu, \tau') = -\left\langle T_\tau c_\nu(\tau) c_\mu^\dagger(0) \right\rangle \,. \tag{2.13}$$

As in the retarded case we can derive the Lehmann representation of the Matsubara Green's function, first in the imaginary-time space

$$\begin{aligned} G(\nu, \tau) &= -\left\langle c_\nu(\tau) c_\nu^\dagger(0) \right\rangle \\ &= -\frac{1}{Z} \sum_{n,m} \mathrm{e}^{-\beta E_n} \left\langle n \left| \mathrm{e}^{\tau H} c_\nu(\tau) \mathrm{e}^{-\tau H} \right| m \right\rangle \left\langle m \left| c_\nu^\dagger \right| n \right\rangle \,, \\ &= -\frac{1}{Z} \sum_{n,m} \mathrm{e}^{-\beta E_n} \mathrm{e}^{\beta(E_n - E_m)\tau} \left| \left\langle m \left| c_\nu^\dagger \right| n \right\rangle \right|^2 \end{aligned} \tag{2.14}$$

which can be Fourier transformed into the frequency space

$$\begin{aligned} G(\nu, \mathrm{i}\omega_n) &= -\frac{1}{Z} \sum_{n,m} \mathrm{e}^{-\beta E_n} \left| \left\langle m \left| c_\nu^\dagger \right| n \right\rangle \right|^2 \int_0^\beta \mathrm{d}\tau \, \mathrm{e}^{\beta(E_n - E_m)\tau} \mathrm{e}^{\mathrm{i}\omega_n \tau} \\ &= \frac{1}{Z} \sum_{n,m} \mathrm{e}^{-\beta E_n} \frac{\left| \left\langle m \left| c_\nu^\dagger \right| n \right\rangle \right|^2}{\mathrm{i}\omega_n + E_n - E_m} \left(\mathrm{e}^{-\beta E_n} + \mathrm{e}^{-\beta E_m} \right) \,. \end{aligned} \tag{2.15}$$

where we introduced the so-called Matsubara frequency

$$\mathrm{i}\omega_n = \begin{cases} \frac{(2n+1)\pi}{\beta} & \text{fermions} \\ \frac{n\pi}{\beta} & \text{bosons} \end{cases} \qquad n = -\infty, \ldots -1, 0, 1, \ldots \infty \; . \tag{2.16}$$

By comparing equations (2.5) and (2.15) we can simply relate the normal retarded Green's function to imaginary-time Matsubara Green's function by performing an analytical continuation

$$\omega + \mathrm{i}\eta = \mathrm{i}\omega_n \; . \tag{2.17}$$

2. Self-energy

In quantum mechanics the self-energy Σ of a particle describes an energy which is caused by the effect due to the interaction with all other particles in the system. In the case of strongly correlated electron systems the electron self-energy arises from the electron moving in its surrounding. Effects like repulsion of the moving electron from other electrons in the vicinity leading to a polarization of the moving particle are included in the self-energy.

In the interacting case the Green's function includes the self-energy which in general is momentum and frequency dependent via

$$G(k, \mathrm{i}\omega_n) = \left(\mathrm{i}\omega_n - \varepsilon_k - \Sigma(k, \mathrm{i}\omega_n)\right)^{-1} \; . \tag{2.18}$$

The real part of the self-energy shifts the poles of the Green's function along the real axis, while the imaginary part is proportional to the life-time of the electrons.

3. Two particle Green's function

In general a two-particle Green's function is defined as

$$G^2(t, t') = -\mathrm{i}\Theta(t - t') \left\langle \left[A(t), A(t') \right] \right\rangle \; , \tag{2.19}$$

where $A(t)$ is any two particle operator, which will lead to the task of calculating a four operator mean value after performing the commutator in equation (2.19). In comparison to the single-particle Green's function defined in (2.1) the second order Green's function (2.19) describes the response of the quantum system involving two particles.

We now show that two particle Green's functions are directly related to single-particle properties like the self-energy and vice versa. In order to see the connection we derive the equation of motion for the single-particle Green's function

$$\begin{aligned} G(\boldsymbol{r}\sigma t, \boldsymbol{r}'\sigma' t') &= -\mathrm{i}\Theta(t - t') \left\langle \left[\psi_\sigma(\boldsymbol{r}, t), \psi^\dagger_\sigma(\boldsymbol{r}', t') \right]_{B/F} \right\rangle \\ \mathrm{i}\partial_t G(\boldsymbol{r}\sigma t, \boldsymbol{r}'\sigma' t') &= (-\mathrm{i}) \left(\mathrm{i}\partial_t \Theta(t - t') \right) \left\langle \left[\psi_\sigma(\boldsymbol{r}, t), \psi^\dagger_{\sigma'}(\boldsymbol{r}', t') \right]_{B/F} \right\rangle \\ &\quad + (-\mathrm{i})\Theta(t - t') \left\langle \left[\mathrm{i}\partial_t \psi_\sigma(\boldsymbol{r}, t), \psi^\dagger_{\sigma'}(\boldsymbol{r}', t') \right]_{B/F} \right\rangle \\ &= \delta(t - t')\delta(\boldsymbol{r} - \boldsymbol{r}') + (-\mathrm{i})\Theta(t - t') \left\langle \left[\mathrm{i}\partial_t \psi_\sigma(\boldsymbol{r}, t), \psi^\dagger_{\sigma'}(\boldsymbol{r}', t') \right]_{B/F} \right\rangle \; , \end{aligned} \tag{2.20}$$

where the following two relations are used: The derivation of the Heaviside step function is the delta function and for the field operators we find the commutation rule

$$\left[\psi_\sigma(\boldsymbol{r}), \psi_\sigma^\dagger(\boldsymbol{r}')\right]_{B/F} = \delta(\boldsymbol{r}-\boldsymbol{r}') \ . \tag{2.21}$$

Equation (2.24) can be more simplified by evaluating the time derivative of the field operator using the Heisenberg picture of time dependent operators

$$\begin{aligned} \mathrm{i}\partial_t \psi_\sigma(\boldsymbol{r},t) &= \mathrm{i}\partial_t \left[\mathrm{e}^{\mathrm{i}tH}\psi_\sigma(\boldsymbol{r})\mathrm{e}^{-\mathrm{i}tH}\right] \\ &= \mathrm{i}\left[\mathrm{e}^{\mathrm{i}tH}\mathrm{i}H\psi_\sigma(\boldsymbol{r})\mathrm{e}^{-\mathrm{i}tH} - \mathrm{e}^{\mathrm{i}tH}\psi_\sigma(\boldsymbol{r})\mathrm{i}H\mathrm{e}^{-\mathrm{i}tH}\right] \\ &= -\mathrm{e}^{\mathrm{i}tH}\left[H\psi_\sigma(\boldsymbol{r}) - \psi_\sigma(\boldsymbol{r})H\right]\mathrm{e}^{-\mathrm{i}tH} = -[H,\psi_\sigma(\boldsymbol{r})](t) \ , \end{aligned} \tag{2.22}$$

where we assumed that the Hamiltonian in (2.22) is time independent. It is always possible to divide the Hamiltonian into two separate parts

$$H = H_0 + H_{\mathrm{int}} \ ,$$

where H_0 is the kinetic part of the Hamiltonian leading to

$$-[H_0,\psi_\sigma(\boldsymbol{r})] = \frac{1}{2m}\int \mathrm{d}\boldsymbol{r}' \left[\psi_\sigma^\dagger(\boldsymbol{r}')\nabla_{\boldsymbol{r}'}^2\psi_\sigma(\boldsymbol{r}'),\psi_\sigma(\boldsymbol{r})\right] = -\frac{1}{2m}\nabla_{\boldsymbol{r}}^2\psi_\sigma(\boldsymbol{r}) \ , \tag{2.23}$$

inserting this result into the equation of motion (2.24) we find

$$\left(\mathrm{i}\partial_t + \frac{1}{2m}\nabla_{\boldsymbol{r}}\right) G(\boldsymbol{r}\sigma t,\boldsymbol{r}'\sigma' t') = \delta(t-t')\delta(\boldsymbol{r}-\boldsymbol{r}') - \mathrm{i}\Theta(t-t')\left\langle\left[-[H_{\mathrm{int}},\psi_\sigma(\boldsymbol{r})](t),\psi_{\sigma'}(\boldsymbol{r}',t')\right]_{B/F}\right\rangle \ , \tag{2.24}$$

with the second part of the right-hand side being a correction of the free particle Green's function. If we think of a general interaction involving two-particle operators

$$H_{\mathrm{int}} = \sum_{i,j,k,\ell}\alpha_{i,j,k,\ell}\psi_i^\dagger\psi_j^\dagger\psi_k\psi_\ell \ , \tag{2.25}$$

we identify two and even higher order Green's function as the correction to the free particle Green's function, which leads to a one to one correspondence of the introduction of the self-energy on the one-particle level, to correction of higher order Green's function in terms of the equation of motion.

4. Two-dimensional Hubbard Model

The Hubbard model [29] is one of the widely used model in the field of strongly-correlated electron systems, since it provides the simplest model to study the effects of electron correlations. In presence of strong correlations between the electrons the Hubbard model gives rise to a number of interesting phenomena like insulating states, magnetic order or even a superconducting gap.

The Hubbard Hamiltonian consists of a kinetic term, allowing the electrons to move from site to site while containing their spin, and an interaction term representing an onsite repulsion of the strength U. This two-particle interaction models the screened Coulomb interaction of an

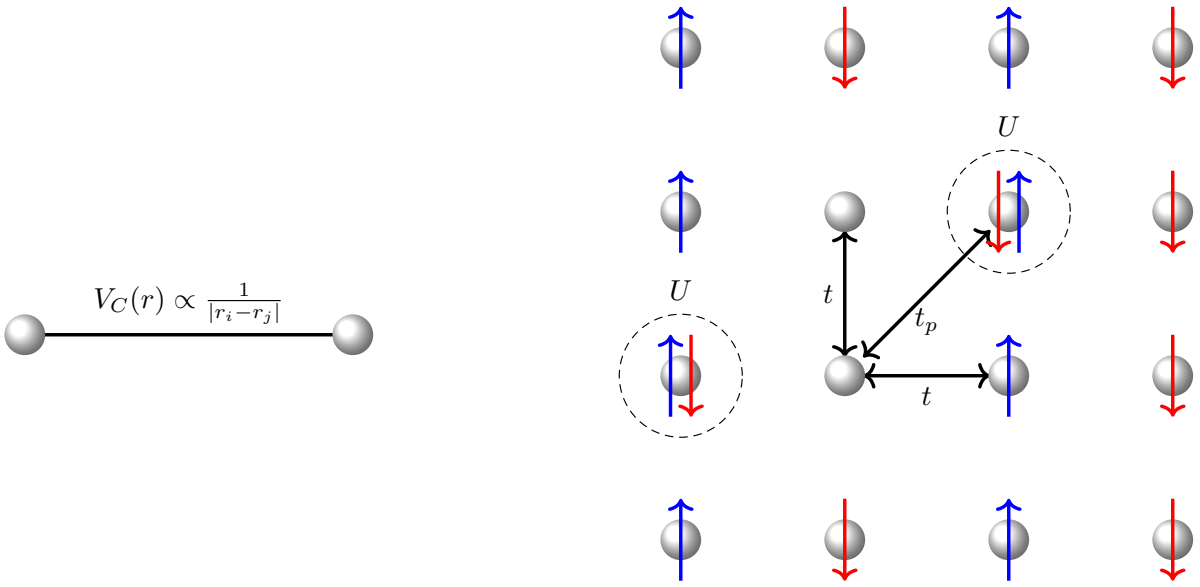

Figure 2.1.: Left: Visual illustration of the $1/r$ decaying Coulomb potential of two electrons. Right: Two-dimensional lattice of the Hubbard model with nearest-neighbor hopping t and next-nearest neighbor hopping t_p. Two electrons are able to occupy the same lattice site for an energy cost of U.

electron on a single site which makes the interaction a local quantity. In general the Hamiltonian can be written as

$$H = -\sum_{\sigma,\langle i,j\rangle} t_{i,j}\left[c^\dagger_{i,\sigma}c_{j,\sigma} + c^\dagger_{j,\sigma}c_{i,\sigma}\right] + \mu\sum_i n_i + U\sum_i n_{i,\uparrow}n_{j,\downarrow}\,, \tag{2.26}$$

where $\langle i,j\rangle$ labels the hopping terms on the lattice with amplitude $t_{i,j}$ and μ is the chemical potential. A sketch of the Hubbard model defined on a two-dimensional lattice is given in figure 2.1.

In the next part we give a detailed description of how to obtain a local model in second quantization (2.26) starting from the pure lattice problem. We start with the stationary Schrödinger equation

$$H\,|\psi\rangle = E\,|\psi\rangle \tag{2.27a}$$

and in real-space representation:

$$\left(\frac{-\hbar^2}{2m}\Delta + V(\mathbf{r})\right)\psi(\mathbf{r}) = E\psi(\mathbf{r})\,. \tag{2.27b}$$

In the case of many electrons/particles like in a solid, the wave function $\psi(\mathbf{r})$ in (2.27b) is a many-body wavefunction, which reads:

$$\psi(\mathbf{r}) \to \psi(\mathbf{r}_0, \mathbf{r}_1, \ldots, \mathbf{r}_N)\,. \tag{2.28}$$

Considering the potential to represent the Coulomb interaction we set $V(\mathbf{r})$ in equation (2.27b) to

$$V(\mathbf{r}) = -\sum_{\mathbf{r}_i,\mathbf{r}_j}\frac{q}{|\mathbf{r}_i - \mathbf{r}_j|}\,. \tag{2.29}$$

Equation (2.28) is a N-particle wave-function which is not yet symmetrized. For Bosons the wave-function has to be the same while exchanging a particle

$$\psi(\mathbf{r}_0, \mathbf{r}_1, \ldots, \mathbf{r}_N) = \psi(\mathbf{r}_1, \mathbf{r}_0, \ldots, \mathbf{r}_N) \ , \tag{2.30}$$

while for electrons and in general the fermionic case a minus sign has to appear in order to fulfill the Fermi statistics

$$\psi(\mathbf{r}_0, \mathbf{r}_1, \ldots, \mathbf{r}_N) = -\psi(\mathbf{r}_1, \mathbf{r}_0, \ldots, \mathbf{r}_N) \ . \tag{2.31}$$

Hence a general basis B of the Hilbertspace $\mathcal{H}$ for a many-body wavefunction of N particles is a tensor product of N single-particle wavefunctions, summed over all possible permutations p

$$B = \sum_p \Pi \psi(\boldsymbol{r}_0) \otimes \psi(\boldsymbol{r}_1) \otimes \ldots \otimes \psi(\boldsymbol{r}_N) \ , \tag{2.32}$$

where Π is $+1$ for bosons and -1 for fermions. Until now the N-particle basis is orthogonal but not normalized. The orthonormal basis then reads

$$B_b = \left\{ \frac{1}{\sqrt{N! n_{\alpha 1}! \ldots n_{\alpha N}}} \sum_p |\alpha_{p1}\rangle \otimes \ldots \otimes |\alpha_{pN}\rangle \right\} \qquad \text{for bosons} \tag{2.33}$$

$$B_f = \left\{ \frac{1}{\sqrt{N! n_{\alpha 1}! \ldots n_{\alpha N}}} \sum_p (-1)^{\#p} |\alpha_{p1}\rangle \otimes \ldots \otimes |\alpha_{pN}\rangle \right\} \qquad \text{for fermions} \tag{2.34}$$

where $\#p$ counts the number of permutations. In theory it is possible to just replace the wave function $\psi(\mathbf{r})$ in the stationary Schrödinger equation (2.27b) with the orthonormal basis state B_f of equation (2.34) which would lead to an nonlinear differential equation with $2N$ (two-dimensional model) degrees of freedom. In order to correctly simulate the whole solid, our lattice model would contain millions of particles, which makes the solution of the stationary Schrödinger equation in the first quantization an infeasible task. We now perform a transformation to go over to the second quantization of our original problem of the many-body wave function. To do this we introduce a new Hilbertspace, the so-called Fock space. A state $|\phi\rangle$ in Fock space does not include a product state of single particle states like (2.34), but has an occupation representation

$$|\phi\rangle = |n_{\alpha_1}, n_{\alpha_2} \ldots n_{\alpha_N}\rangle \ , \tag{2.35}$$

where n_{α_i} is the number of particles in the quantum state α_i, which for example could be a combination of a spin and an orbital index. For fermions only one particle can be in the same state. A general Fock state is a combination of all possible occupations weighted by a factor λ, hence

$$|\psi\rangle = \sum_{n_1, n_2, \ldots n_N} \lambda(n_1, n_2, \ldots n_N) \, |n_1, n_2, \ldots, n_3\rangle \ , \tag{2.36}$$

where we set $n_i = n_{\alpha_i}$ compared to equation (2.35). Obviously the Fock space preserves the total particle number which always leads to the sum rule

$$\sum_i n_i = N \ . \tag{2.37}$$

We can rewrite the general Fock state in equation (2.36) in real space by introducing field operators

$$\Psi(\mathbf{r}) = \sum_\nu \psi_\nu(\mathbf{r}) a_\nu \ , \qquad \Psi(\mathbf{r}) = \sum_\nu \psi_\nu^*(\mathbf{r}) a_\nu^\dagger \ , \tag{2.38}$$

where $a_\nu / a_\nu^\dagger$ is a general operator (boson or fermion) which annihilates/creates a particle in quantum state ν weighted by $\psi_n(\mathbf{r})$ which is an ordinary first quantisized wave function. Now we replace the many-body wave function in (2.27b) by the corresponding field operators and find

$$\begin{aligned} H = &\sum_\sigma \int \mathrm{d}\mathbf{r}\, \Psi_\sigma^\dagger(\mathbf{r}) \frac{-\hbar^2}{2m} \nabla^2 \Psi_\sigma(\mathbf{r}) \\ &+ \sum_{\sigma,\sigma'} \int \mathrm{d}\mathbf{r} \int \mathrm{d}\mathbf{r}'\, \Psi_\sigma^\dagger(\mathbf{r}) \Psi_{\sigma'}^\dagger(\mathbf{r}') \frac{1}{|\mathbf{r}-\mathbf{r}'|} \Psi_{\sigma'}^\dagger(\mathbf{r}) \Psi_\sigma^\dagger(\mathbf{r}) \,. \end{aligned} \tag{2.39}$$

For the transition from equation (2.39) involving integrals over the whole real space to the Hubbard model in equation (2.26) only containing lattice sites, we use the up to now undefined wave functions of the definition of the field operators in (2.38).

In this part we introduce the concept of the so-called Wannier functions. Wannier functions are a complete set of orthogonal functions and can be used to represent the wave function in (2.38). There are many ways to create Wannier functions like the maximal localized Wannier functions [30]. In this work we follow the original proposal of Wannier [31] published in 1937, where the Wannier basis is introduced as

$$\phi_{i,\alpha}(\mathbf{r}) = \frac{1}{N} \sum_{\mathbf{k}} \mathrm{e}^{-\mathrm{i}\mathbf{k}\mathbf{R}_i} \psi^B_{\mathbf{k},\alpha}(\mathbf{r}) \,, \tag{2.40}$$

and is connected by an unitary transformation to the Bloch function of the solid

$$\psi^B_{\mathbf{k},\alpha}(\mathbf{r}) = \mathrm{e}^{-\mathrm{i}\mathbf{k}\mathbf{r}} u_{\mathbf{k},\alpha}(\mathbf{r}) \,, \tag{2.41}$$

where $u_{\mathbf{k}}(\mathbf{r})$ has the same periodicity as the original lattice, N is the number of sites in the lattice and $\mathbf{R}_i$ is the position of the atom i in the lattice. We note that in this work we use the Born-Oppenheimer approximation, as well as no relativistic corrections. The Bloch functions in (2.41) are orthogonal, hence

$$\int \mathrm{d}\mathbf{r} \left(\psi^B_{\mathbf{k}',\alpha'}(\mathbf{r})\right)^* \psi^B_{\mathbf{k},\alpha}(\mathbf{r}) = \delta_{\alpha,\alpha} \delta(\mathbf{k}-\mathbf{k}') \,. \tag{2.42}$$

For the kinetic term we find by insertion of the Wannier functions (2.40)

$$\begin{aligned} H_{\mathrm{kin}} &= \sum_\sigma \int \mathrm{d}\mathbf{r}\, \Psi_\sigma^\dagger(\mathbf{r}) \frac{-\hbar^2}{2m} \nabla^2 \Psi_\sigma(\mathbf{r}) \\ &= \sum_\sigma \sum_{i,j} \underbrace{\int \mathrm{d}\mathbf{r}\, \phi^*_{i,\sigma}(\mathbf{r}) \frac{-\hbar^2}{2m} \nabla^2 \phi^*_{j,\sigma}(\mathbf{r})}_{\equiv -t_{i,j}} c_i^\dagger c_j \,. \end{aligned} \tag{2.43}$$

The magnitude of the parameter $t_{i,j}$ depends only on the choice of Wannierfunctions. Hubbard's original idea goes back to a strong, s-orbital like localization of a Wannier function $\phi_{i,\alpha}$ at the lattice site $\mathbf{R}_i$. Keeping in mind this idea it can be shown (see [31]) that not only close neighboring sites $\langle i,j \rangle$ show a non-zero integral for t_{ij} in (2.43), but also the Coulomb potential reduces to the onsite term

$$H_{\mathrm{Coulomb}} = \sum_{\sigma,\sigma'} \int \mathrm{d}\mathbf{r} \int \mathrm{d}\mathbf{r}'\, \Psi_\sigma^\dagger(\mathbf{r}) \Psi_{\sigma'}^\dagger(\mathbf{r}') \frac{1}{|\mathbf{r}-\mathbf{r}'|} \Psi_{\sigma'}^\dagger(\mathbf{r}) \Psi_\sigma^\dagger(\mathbf{r})$$

$$= \underbrace{\int \mathrm{d}\mathbf{r} \int \mathrm{d}\mathbf{r}'\, \phi^*_{i,\uparrow}(\mathbf{r})\phi_{i,\uparrow}(\mathbf{r})\phi^*_{i,\downarrow}(\mathbf{r}')\phi_{i,\downarrow}(\mathbf{r}')}_{\equiv U} n_{i,\uparrow}n_{i,\downarrow} \,, \tag{2.44}$$

neglecting all intra-site interactions. In the picture of localized s-orbitals this makes sense, since the integral would become zero when one Wannier function is localized at site j, having no overlap with site i. This approximation is highly dependent on the choice of Wannier basis, still the Hubbard model using the idea of strongly localized s-wave Wannier function is the most common choice when it comes to simulate a solid taking into account interacting electrons via the Coulomb interaction.

5. Approximate solutions of the Hubbard model

Even though there is no exact solution of the two dimensional Hubbard model we discuss certain limits where an approximation provides insight to the ground state and its magnetic properties of the Hubbard model.

5.1. The non-interacting case

We start with the easiest approximation by just neglecting the coulomb interaction in (2.26), i.e. $U = 0$. The ground state then is described by a free Fermi gas and reads

$$|GS\rangle = \prod_{k<k_F} \prod_{\sigma} c^\dagger_{\sigma,k} |0\rangle \,, \tag{2.45}$$

where k_F is the Fermi momentum and $|0\rangle$ represents the vacuum state.

To investigate the magnetization properties of the ground state we apply a constant homogeneous magnetic field in z-direction

$$H_B = -g\frac{\mu_B}{2} B_z \,,$$

with μ_B being the Bohr magneton and g the so-called g-factor which can be approximated by the value of 2 in the case of electrons. The application of a magnetic field will lead to a lowering of the energy for the electrons if they align parallel to the magnetic field, which inevitable leads to an imbalance of total electrons with up and down spins

$$|n_\uparrow - n_\downarrow| = \delta_n \,.$$

This difference can be related to the change in the density of states. The density of states (DOS) is defined as

$$D(E) = \frac{\mathrm{d}n}{\mathrm{d}E} \,. \tag{2.46}$$

The occupation of states changes close to the Fermi energy, hence

$$\delta_n = \mathrm{d}_n = D_F E = D_F \mu_B B_z \,.$$

The change of magnetization is then given by

$$\delta_m = \frac{g\mu_B}{2}\delta_n = D_F (g\mu_B)^2 B_z \,, \tag{2.47}$$

which lead to the so-called Pauli susceptibility

$$\chi_{\text{pauli}} = \frac{\delta_m}{B} = D_F (g\mu_B)^2 \,. \tag{2.48}$$

5.2. The weak correlation limit

For small, but not vanishing, values of U we still expect the electrons to behave nearly as free fermions. Indeed one can show that for small interactions the system is in a so-called Fermi liquid regime, where the dispersion relation of the electrons is the same as for the ideal Fermi gas but the particles have a renormalized mass and propagate through the solid as so-called quasi-particles

$$\varepsilon_{QP}(Ik) = \frac{m}{m^*}\varepsilon(Ik) \; . \tag{2.49}$$

The magnetization properties of the low coupling Regime $t \gg U$ can be understood nicely if we take the approach of the Hartree-Fock approximation, which exchanges the two-particle coulomb interaction into one-particle operators weighted by a mean-field approximation, hence

$$H_{\text{int}} = \sum_i U n_{i,\uparrow} n_{i,\downarrow} \to H_{\text{int}}^{HF} = \sum_i U n_{i,\uparrow} \left\langle n_{i,\downarrow} \right\rangle + \left\langle n_{i,\uparrow} \right\rangle n_{i,\downarrow} + \left\langle n_{i,\uparrow} \right\rangle \left\langle n_{i,\downarrow} \right\rangle \; . \tag{2.50}$$

We assume an ferromagnetic solution

$$\langle n_{i,\sigma} \rangle = \frac{n}{2} + \sigma m \; ,$$

where $m = (n_\uparrow + n_\downarrow)/2$ represents the total magnetization and $n = n_\uparrow + n_\downarrow$ is the particle number. Substituting in equation (2.50) and rewriting the single-particle operator in terms of the spin operator S_Z leads to

$$H_{\text{int}}^{HF} = U \sum_i \left[-2mS_z + m^2 + \frac{n^2}{4} \right] \; . \tag{2.51}$$

The solution of the interaction Hamiltonian in (2.51) in combination with the kinetic term is a known problem and the solution

$$\varepsilon^{HF}(\boldsymbol{k}) = \varepsilon(\boldsymbol{k}) + \frac{nU}{2} - \sigma m U + \frac{g}{2}\mu_B h_z \sigma \; , \tag{2.52}$$

can be found for the energy, where the last part in the left-hand side of equation (2.52) is the Zeeman splitting which stems from a magnetic field. We are now able to find an expression for the magnetization at the zero temperature limit $T \to 0$

$$M_z = -g\mu_B m = \chi_{\text{pauli}} \left[h_z - \frac{2}{g\mu_B} U m \right] = \chi_{\text{pauli}} \left[h_z - \frac{2}{g^2\mu_B^2} U M_z \right] \; , \tag{2.53}$$

which leads to the so-called Stoner susceptibility

$$\chi_{\text{St}} = \frac{\chi_{\text{pauli}}}{1 - 2g^2\mu_B^2 U \chi_{\text{pauli}}} \; . \tag{2.54}$$

The susceptibility χ_{St} exhibits a critical interaction of $U_C = 2/D_F$, which means that even for small, but not vanishing interaction values U, the susceptibility can show a divergence and because of this the ground state is unstable against a ferromagnetic order.

5.3. The strong correlation limit

For the large interaction limit $U \gg t$ and for half filling the Hubbard model transforms into the so-called Heisenberg model which reads

$$H = -J \sum_i \boldsymbol{S}_i \cdot \boldsymbol{S}_{i+1} \,. \tag{2.55}$$

The transition from the Hubbard to the Heisenberg model in the strong correlation regime can be understand in a simple figurative way. When the Coulomb interaction U is large, such as the kinetic gain of energy of a hopping process is way lower than the amount of potential energy which has to be paid if two electrons are on the same lattice site, the system is *frozen* out. In the half-filled case we find exactly one electron per site, which does not move. The kinetic term as well as the interaction term reduce to zero in the Hubbard model and electrons only interact magnetically via their spin with each other. The state of the Heisenberg model is a priori not clear and even if the Hamiltonian in (2.55) looks simple, it cannot be solved in two-dimensions without the use of approximations. Nonetheless it is possible to make statements about the model, the parameter J in equation (2.55) and especially the sign of J gives implication of the favored magentic state the Heisenberg model will take. For $J < 0$ the spins of neighboring sites will align anti-parallel to each other (anti-ferromagnetic), whereas for $J > 0$ the spins will try to minimize the energy by aligning parallel to each other leading to a ferromagnetic ordering of the whole system.

6. Dynamical Mean-Field Theory

The dynamical mean-field theory (DMFT) consists of a mapping from a known lattice problem with a large number of degrees of freedom onto an effective impurity model with a small number of degrees of freedom. In the extreme limit, where the coordination number of the lattice is infinite, the dynamical mean-field theory is not an approximation anymore and describes the full solution of the lattice problem.

The main idea behind the mapping of a full lattice problem onto a smaller impurity problem is the physical picture of electrons on the impurity interacting with an external bath of electrons surrounding the impurity. Using the Hubbard model (2.26) as an example for a many-body Hamiltonian we can write down the action in imaginary time, for the mapping from the lattice model onto a single-site impurity

$$S_I = -\int_0^\beta \mathrm{d}\tau \int_0^\beta \mathrm{d}\tau' \sum_{\sigma,i} c^\dagger_{i,\sigma}(\tau)\mathcal{G}^{-1}(\tau-\tau')c_{i,\sigma}(\tau') + U\int_0^\beta \sum_i n_{i,\uparrow}(\tau)n_{i,\downarrow}(\tau') \,. \tag{2.56}$$

Since we are using a mapping of the lattice model onto a single-site impurity there is no summation over the orbital indices i in (2.56). We can identify the field $\mathcal{G}(\tau-\tau')$ in (2.56) as the effective Weissfield. In general the Weissfield describes the annihilation of an electron on the impurity at imaginary time τ while an electron is created on the impurity at time τ'. Electrons on the impurity are created/annihilated by the means of jumping from the surrounding electron bath on the impurity and vice versa. The difference to classical mean-field theories lies in the dependence on the imaginary time of the Weissfield $\mathcal{G}(\tau-\tau')$, which allows to take into account local temporal fluctuation while spatial fluctuations are frozen out on the mean-field

level [1]. We note that even though the Weissfield is the bare Green's function, describing the impurity, it is a non-local quantity, moreover it is connected to the self-consistency condition

$$\mathcal{G}(\mathrm{i}\omega_n)^{-1} = \left(\sum_k [\mathrm{i}\omega_n + \mu - \varepsilon_k - \Sigma(\mathrm{i}\omega_n)] \right)^{-1} + \Sigma(\mathrm{i}\omega_n) \tag{2.57}$$

where $\Sigma(\mathrm{i}\omega_n)$ describes the self-energy and ε_k is the dispersion relation of the lattice model. Using the self-consistent equation (2.57) we can write down the DMFT cycle

1. Create the Weissfield $\mathcal{G}(\mathrm{i}\omega_n)$ according to (2.57) by using $\Sigma(\mathrm{i}\omega_n)$.
2. Solve the impurity problem.
3. Calculate the impurity self-energy:
$$\Sigma_{\mathrm{imp}}(\mathrm{i}\omega_n) = \mathcal{G}^{-1}(\mathrm{i}\omega_n) - G^{-1}_{\mathrm{imp}}(\mathrm{i}\omega_n) \; . \tag{2.58}$$
4. Demand that the impurity self-energy is equal to the lattice self-energy: $\Sigma_{\mathrm{imp}}(\mathrm{i}\omega_n) = \Sigma(\mathrm{i}\omega_n)$
5. Repeat step 1-4 until convergence is reached.

Even though one of the major success of the dynamical mean-field theory is able to describe the Mott metal-to-insulator transition in finite dimensions, it is still a theory with severe limitations. Those limitations are especially visible in the regime of low dimensional systems and low temperatures, where the physics are dominated by non-local correlations. Being able to only render local physics makes it also impossible to study non-local spin-correlations like the d-wave superconductivity in the pure DMFT approach.

7. Quantum Monte-Carlo as Impurity Solver

In the introduction of the dynamical mean-field theory we introduced a mapping of a lattice problem onto a quantum impurity problem. Up to now we did not mention how to solve such a quantum impurity model. To this end we briefly introduce and discuss the powerful continuous-time quantum Monte-Carlo solver (CT-QMC) which provides a numerical foundation in order to solve the DMFT approach. For further inside and knowledge about CT-QMC we recommend the following review [32].

We start by a basic reformulation of a quantum impurity problem taking the following form

$$H_I = H_{\mathrm{loc}} + H_{\mathrm{bath}} + H_{\mathrm{hyb}} \; . \tag{2.59}$$

We divide the whole impurity problem H_I into three sub parts. The first one is H_{loc} which describes the local parts of the impurity, so every interaction of orbitals inside the in general multi-orbital impurity is gathered in this part. Next we define the Hamiltonian of the thermal electron bath surrounding the impurity labeled as H_{bath} where the bath can be interpreted as infinitely many harmonic oscillators with a continuous energy spectrum coupled to the impurity via H_{hyb}. The next step persists in the elimination of the thermal bath degree of freedom. In order to achieve this we can rewrite the partition function Z in an imaginary time representation which leads to the following equation, compare equations (8) and (9) in [32]

$$Z = \int \mathcal{D}[d^\dagger, d] \mathrm{e}^{-S} \tag{2.60}$$

with the defintion of the action

$$S = \sum_{ab} \int_0^\beta \int_0^\beta \mathrm{d}\tau \, \mathrm{d}\tau' \, d_a^\dagger(\tau) \left[(\partial_\tau + E_{ab}) + \Delta_{ab}(\tau - \tau') \right] d_b(\tau') + \int_0^\beta \mathrm{d}\tau \, H_{\mathrm{loc.}}(\tau) \; . \tag{2.61}$$

In equation (2.60) the operators $d^\dagger / d$ are creation/annihilation operators on the impurity. The indices a, b appearing in the action defined in equation (2.61) are labels for the orbitals living on the impurity and E_{ab} then describes the energy of the orbitals a, b. $\Delta_{a,b}(\tau - \tau')$ is the so-called hybridization function which wraps all the important information about the coupling between the impurity and the thermal bath.

Equations (2.60) and (2.61) are the basis of all types of impurity solvers, for example the exact diagonalization method (ED), the numerical renormalization group (NRG) and the density matrix renormalization group (DMRG). In this work we are only using the CT-QMC approach to solve the impurity problem. We start with a reformulation of the original impurity Hamiltonian (2.59) into the general form

$$H_I = H_1 + H_2 \; . \tag{2.62}$$

The next step is to transform the partition function $Z = \mathrm{e}^{\beta H_I}$ into the interaction representation with respect to H_a and expand the result in powers of H_b, one then arrives at the following equation for the partition function Z, as can be found in equation (19) of [32]

$$Z = \sum_k (-1)^k \int_0^\beta \mathrm{d}\tau \ldots \int_{\tau_{k-1}}^\beta \mathrm{d}\tau_k \times \mathrm{Tr} \left[\mathrm{e}^{-\beta H_a} H_b(\tau_k) H_b(\tau_{k-1}) \ldots H_b(\tau_1) \right] \; . \tag{2.63}$$

The trace in equation (2.63) represents a sampling over all orders k and all times $\tau_1 \ldots \tau_k$. Since the partition function defined in (2.63) contains a sampling over all times $\tau_1 \ldots \tau_k$ we start from a theory formulated in a continuous time (CT) representation, while the sampling over all orders and times is done in a quantum Monte-Carlo (QMC) procedure leading to the combined name of CT-QMC. The choice of H_a and H_b of equation (2.62) can be chosen arbitrarily. The two most common choices are $H_b = H_{\mathrm{hyb}}$ which is called CT-HYB and $H_b = H_{\mathrm{loc}}$ labeled as CT-INT. In this work all results are obtained by using the CT-INT approach.

7.1. Statistical mean value in the Monte-Carlo approach

Before discussing the CT-INT impurity solver, we mention some general basics of classical and quantum Monte-Carlo approaches. They are always used when a large phase space has to be sampled like the one found in equation (2.63). Solving the integral

$$Z = \int_{\mathcal{C}} \mathrm{d}\boldsymbol{x} p(\boldsymbol{x}) \; , \tag{2.64}$$

using the (quantum) Monte-Carlo method, the index $\mathcal{C}$ indicates the sampling over the whole phase space, $\boldsymbol{x}$ is a point in phase space and $p(\boldsymbol{x})$ describes a weight of the phase space point $\boldsymbol{x}$. If we think of the classical Monte-Carlo method $p(\boldsymbol{x})$ would be described by the Maxwell-Boltzmann weight. The statistical mean value of an observable A can be then calculated via

$$\langle A \rangle = \int_{\mathcal{C}} \mathrm{d}\mathcal{A}(\boldsymbol{x}) p(\boldsymbol{x}) \; . \tag{2.65}$$

The statistical mean value (2.65) can be approximated by selecting $\boldsymbol{M}_i$ configurations obtained by a Monte-Carlo method with a probability $p(\boldsymbol{x})/Z$ and then taking an average over this configurations like described in [32]

$$\langle A \rangle = \frac{1}{M} \sum_{i}^{M} \mathcal{A}_i p(\mathbf{x}_i) \ . \tag{2.66}$$

In order to use the equal sign between the left and right part of equation (2.66) we have to take in consideration the central limit theorem, which states that the equal sign is valid if we draw enough random configurations M_i in (2.66).

8. CT-INT

The CT-INT introduced 2004 by Rubtsov and Lichtenstein [33] was the first continuous-time solver to tackle a quantum impurity problem. Once again following the guideline of the review [32] we want to briefly summarize the steps and needs of an CT-INT solver by taking the single-band impurity problem as an example. We can divide the action of the impurity problem S introduced in (2.56) into a bare part S_0 and interacting part S_I as the following

$$S_0 = -\int_0^\beta \mathrm{d}\tau \int_0^\beta \mathrm{d}\tau' \sum_{\sigma,i} c^\dagger_{i,\sigma}(\tau) \mathcal{G}^{-1}(\tau - \tau') c_{i,\sigma}(\tau') \tag{2.67}$$

$$S_I = U \int_0^\beta \sum_i n_{i,\uparrow}(\tau) n_{i,\downarrow}(\tau') \ . \tag{2.68}$$

Expanding the action in terms of powers of the interaction U leads to the following equation (see equation (51) in [32])

$$\frac{Z}{Z_0} = \sum_{k=0}^{\infty} \frac{(-U)^k}{k!} \int_0^\beta \mathrm{d}\tau_1 \ldots \mathrm{d}\tau_k \left(\prod_\sigma \det \mathbb{D}^\sigma_k \right) \ , \tag{2.69}$$

with

$$[\mathbb{D}^\sigma_k]_{i,j} = \mathcal{G}^\sigma(\tau_i - \tau_j) \ . \tag{2.70}$$

Equation (2.69) can now be treated by the use of continuous-time sampling where we resign on further discussions and refer one last time to [32] pointing out all difficulties of this continuous-time sampling and giving proposals to overcome those in a numerically efficient way.

9. The infamous fermionic sign problem

We start this section by stating that the fermionic sign problem, also called negative-sign problem, is a NP hard problem [34], which means if we would find a generic solution of the fermionic sign problem we would have also found a solution to solve all other NP problems in a polynomial time P. From time to time it is found that NP hard problems are actually in the class of P problems, but there is not a single known polynomial solution for a NP complete problem even though decades of intensive research were committed to it. It is believed that those solutions are not existent and a prove of $NP \neq P$ remains one of the unsolved mathematical millennium problems which the Clay Mathematics Institute would reward with a

one million dollar prize for a solution. NP here stands for non-deterministic polynomial time and in principle finding a solution of a NP hard problem can be done in a polynomial time if we have access to an infinite amount of computational power. In reality we are not blessed with infinite computational power and therefore the fermionic sign problem has no generic solution even though an ansatz to solve a NP hard problem can be checked in polynomial time to give the right solution.

Having stated that there is no generic solution of this problem, at least not in the foreseen future, to discuss the origin of the sign problem and which impact it has on quantum Monte-Carlo solutions in the DMFT framework. To do so we want to resume starting from the statistical average of Monte-Carlo calculations defined in equation (2.65). In a classical approach the statistical weights $p(\mathbf{x})$ are in fact the Boltzmann weights for a given system and therefore can be directly interpreted as probabilities since these weights are always positive. In the quantum Monte-Carlo approach the statistical weights of $p(\boldsymbol{x})$ are not necessarily positive-definite, for example by sampling over a quantum Monte-Carlo configuration leading to an odd number of fermionic exchanges leads to an overall minus sign. To avoid non positive-definite weights in the Monte-Carlo procedure defined in equation (2.66), one can simply redefine the expectation value in the Monte-Carlo approach as

$$\langle A \rangle = \frac{\sum_i^M \mathcal{A}_i p(\mathbf{x}_i)}{\sum_i^M p(\mathbf{x}_i)} = \frac{\sum_i^M \mathcal{A}_i s(i) |p(\mathbf{x}_i)| / \sum_i |p(\mathbf{x}_i)|}{\sum_i^M s(i) |p(\mathbf{x}_i)| / \sum_i |p(\mathbf{x}_i)|} = \frac{\langle As \rangle^B}{\langle s \rangle^B} \,, \tag{2.71}$$

with $s(i) = \text{sign}[p(\mathbf{x}_i)]$. Equation (2.71) is now again always positive-definite since we are sampling with respect to a bosonic system, which is indicated by the superscript B. It can be shown [34] that the sign average decays exponentially with the system's particle number N

$$\langle s \rangle = Z/Z^B = \mathrm{e}^{-\beta N \Delta f} \,, \tag{2.72}$$

where β is the inverse temperature of consideration and Δf describes the difference of the free energy between the fermionic system under investigation to that of the corresponding bosonic one [34]. Reinserting equation (2.72) into (2.71) gives rise to an exponential growth of the statistical error in dependence of the particle number N and the inverse temperature β.

10. Analytical Continuation

In the following section we discuss the transition from imaginary time Green's functions $G(\tau)$, and their respective Fourier transform, the so called Matsubara Green's function $G(\mathrm{i}\omega_n)$, back to real time/frequency objects $G(t)/G(\omega)$. Since the imaginary time approach is only a mathematical trick to make many-body calculations easier in terms of perturbation approaches, a direct relation to measurable quantities are not available. With the help of a so-called analytical continuation the shift from imaginary time space to real time and measurable quantities is performed. In practice the analytical continuation is not trivially done by the replacement $\mathrm{i}\omega_n \to \omega$ since the kernel of this mapping is ill-conditioned [35]. Ill-conditioned in this case means that a small change in the input, i.e. $G(\mathrm{i}\omega_n)$, has a huge impact in the output of the real-frequency object $G(\omega)$. Since the results of this work are produced within the Quantum Monte-Carlo framework we can not avoid statistical noise in our data which would lead to a huge problem by performing the simplest analytical continuation possible $\mathrm{i}\omega_n \to \omega$. To this end a lot of different approaches of analytical continuations have been proposed such as

the maximum entropy method [36–38] which is used throughout as the standard analytical continuation method in this work, algorithms based on the singular-value decomposition [39] (SVD), machine learning [40] approaches or stochastic methods [41–45].

11. The maximum entropy method

As mentioned above, the real frequency data in this work is obtained by performing an analytical continuation in the maximum entropy method (maxent) framework. In terms of the numerical structure a TRIQS application of maxent [35] exists and is used. In the following we shortly discuss the mathematical ideas behind the maxent method. We consider a Matsubara Green's function $G(\mathrm{i}\omega_n)$ which is connected on the whole complex plane z, with exceptions of the real-space poles below zero, through the spectral function A via

$$G(z) = \int \mathrm{d}\omega \frac{A(\omega)}{z - \omega} \,, \tag{2.73}$$

where in general G and A are matrix valued objects. In this case every element transforms according to equation (2.73) independently. We can Fourier transform equation (2.73) with respect to z into the imaginary time space (including the inverse temperature β)

$$G(\tau) = \int \mathrm{d}\omega \frac{\mathrm{e}^{\omega\tau}}{1 + \mathrm{e}^{-\omega\beta}} A(\omega) \,. \tag{2.74}$$

Since the fraction in the integrand of (2.74) is purely real the imaginary part of the spectral function $A(\omega)$ is only connected to the imaginary part of $G(\tau)$, the same holds for the real parts of both sides of the equation. In terms of handling equation (2.74) numerically we first use a known reformulation of (2.74)

$$\mathbf{G} = \mathbf{K}\mathbf{A} \,, \tag{2.75}$$

where the so-called kernel $\mathbf{A}$ is a matrix valued function

$$K_{i,j} = \frac{\mathrm{e}^{\omega_j \tau_i}}{1 + \mathrm{e}^{-\omega_j \beta}} \,. \tag{2.76}$$

Up to this point one can calculate $G(\tau)$ with the knowledge of $A(\omega)$ without any problems using equation (2.75), the problem arises by doing the inversion, i.e. , calculating the spectral function with the help of the Green's function

$$\mathbf{A} = \mathbf{K}^{-1}\mathbf{G} \,. \tag{2.77}$$

Equation (2.77) is ill-posed since any small change of $\mathbf{K}$ leads to a huge one in $\mathbf{A}$, resulting in a very large condition number of $\mathbf{K}$ due to the exponential decay with ω and τ. In general the task of an analytical continuation is not to solve equation (2.77) directly, but to find the best approximation for $\mathbf{A}$. Following the easiest path one could think of the concept of misfit measurement

$$\chi^2(\mathbf{A}) = (\mathbf{K}\mathbf{A} - \mathbf{G})^T \mathbf{C}^{-1} (\mathbf{K}\mathbf{A} - \mathbf{G}) \,, \tag{2.78}$$

with a covariance matrix $\mathbf{C}$ and then use the minimized χ. However this approach fails in terms of an uncontrollable error [46]. The maxent method consists of adding an entropy term $S(A)$ and the minimization of

$$Q_\alpha(\mathbf{A}) = \frac{1}{2}\chi^2(\mathbf{A}) - \alpha S(\mathbf{A}) \,. \tag{2.79}$$

The parameter α is called a hyperparmeter and is something which has to be chosen by hand. There are several ways to determine/chose α which can be found in [35]. For the entropy it is shown that every non-negative function $A(\omega)$ leads to [47]

$$S(\omega) = \int \mathrm{d}\omega \left[A(\omega) - D(\omega) - A(\omega) \log \frac{A(\omega)}{D(\omega)} \right] , \tag{2.80}$$

where $D(\omega)$ is a default model.

To conclude we remark that the analytical continuation is never an exact way of reproducing a real time Green's function $G(\omega)$ of his Matsubara counter apart $G(\mathrm{i}\omega_n)$. Moreover there is no magical solution to the ill-defined problem of the analytical continuation, where every method can only extract known information of the system and has to somehow estimate missing informations. In this work this estimation of missing in-formations is done by the maximal entropy approach.

III. Results of dynamical mean-field theory calculations

In this chapter we use the dynamical mean-field theory to solve the Hubbard model in two dimensions. Besides taking a look at the the self-energy we will also discuss the different phases arising in the Hubbard model depending on the interaction strength U by calculating spectral functions with the analytical continuation.

1. Phase diagram of the two-dimensional Hubbard model

In the following we consider the half-filled case of the two-dimensional Hubbard model (2.26) with fixed chemical potential $\mu = U/2$, and only nearest neighbor hopping t. For a fixed inverse temperature of $\beta t = 5$, self-energies for different values of U are shown in the left panel of figure 3.1. Using the converged self-energies we determine the spectral function of the local Green's function which is shown in the right panel of figure 3.1. Starting from the weak coupling regime, i.e. small U values, to large interactions, we can analyze the spectral function evolving.

In the weak coupling regime $U/t = 5$ the system possesses a peak in the spectral function at $\omega = 0$. This peak can be explained by following the Landau theory of Fermi liquids. In general a Fermi liquid is a system of interacting Fermi particles with spin $1/2$. At the basis of the Landau theory of Fermi liquids stands the assumption that the excitation spectrum follows the same principle as the ideal Fermi gas. The interaction of the fermions between each other is taken into account by the concept of quasi-particles [48]. In the regime of weak interaction the quasi-particles are propagating fermions with different effective mass than the original, undressed fermions in the non-interacting case. Hence the peak in the spectral function for $U/t = 5$ is the so-called quasi-particle peak following from the mass renormalization of the fermions.

For large interaction values $U \gg t$ the system is in an insulating state. This is shown in figure 3.1 for the interaction $U/t = 15$. The insulating behavior is clearly visible in the spectral function as a gap is present at the Fermi energy $\omega = 0$. Taking a closer look at the spectral function we can even read out the interaction strength by measuring the distance between the two maximums of the positive and negative peaks. Those peaks are called upper respectively lower Hubbard band and are separated by the interaction value of U. This can be explained by thinking of the simple picture of a half-filled lattice, where each lattice site is occupied by one electron with either spin up or down. Moving one electron from one site to another leads to a net energy gain of t while the double occupation features an energy loss of U. For the case $U \gg t$ no electrons are able to move on the lattice and therefore the lattice is in an insulating state. The system is then a so-called Mott metal-to-insulator.

In the intermediate regime $U/t = 7.5$ in figure 3.1 we can see three peaks in the spectral function, hence this regime shows a spectral function with a so-called *three-peak structure*.

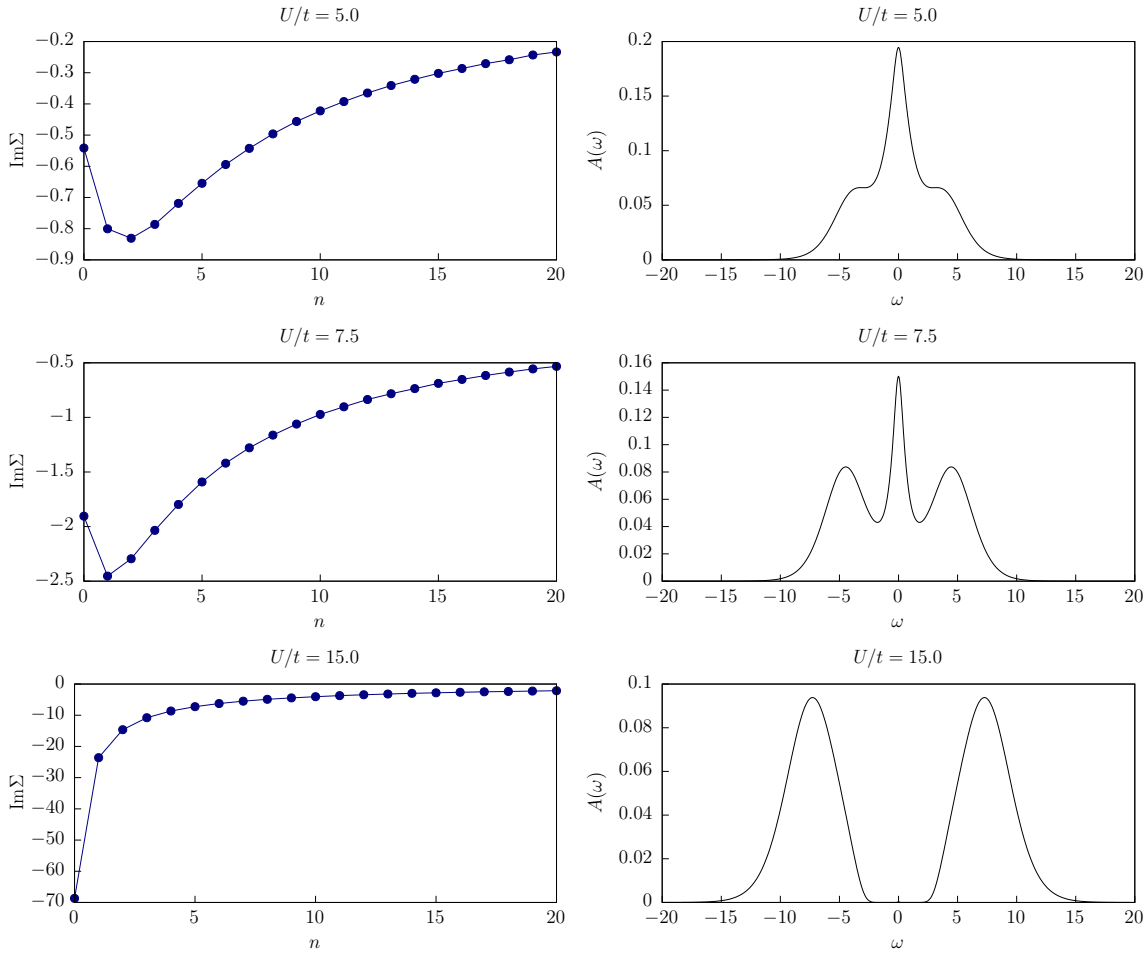

Figure 3.1.: Left: Converged DMFT self-energy data in the Matsubara space for different interaction values U/t. Right: Corresponding local spectral functions obtained by the analytical continuation of the local Green's function. The inverse temperature in all shown cases is $\beta t = 5$.

Besides the distinct quasi-particle peak at $\omega = 0$ we already can see the two Hubbard bands arising.

A look at the spectral function makes it easy to distinguish the metallic and the insulating phase of the Hubbard model via a gap appearing at $A(\omega = 0) = 0$ for the insulating phase. Since the analytical continuation should be treated as an approximation, one can resort back to data directly available solving the self-consistent DMFT equation, i.e. , the local Green's function in imaginary time can be used to approximate the spectral function at the Fermi energy $G_{\mathrm{loc.}}(\tau = \beta/2) \approx A(\omega = 0)$. Since we are dealing with numerical data obtained via Monte-Carlo calculations we are using data including statistical noise. In order to distinguish different phases using observables crossing the value 0 we have to redefine the origin within statistical errorbars. In the case of the shown DMFT calculation it is sufficient to claim that observables are zero while being smaller than 5e−4. This leads to the following selection rule for generating the transition line of the two-dimensional Hubbard model

$$A(\omega = 0), G(\tau = \beta/2) = \begin{cases} > 5\mathrm{e}{-3}, & \text{metallic} \\ < 5\mathrm{e}{-3}, & \text{insulating} \end{cases} . \tag{3.1}$$

Taking a look at figure 3.2 we see that the two-dimensional Hubbard model at half-filling has a

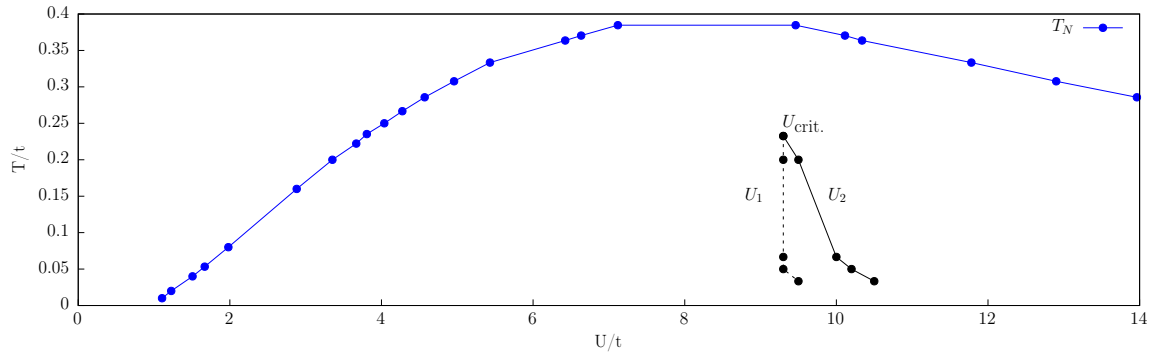

Figure 3.2.: Phase space of the half-filled, two-dimensional Hubbard model, obtained using the DMFT approach. The blue curve indicates the Néel transition temperature. Below this threshold the system goes into an ordered magnetic phase. The black lines indicate the second-order metal to insulator transition obtained by equation (3.1), where the dashed line is calculated by traversing from large to low interaction values U and for the solid lines vice versa.

MIT at around $U/t = 10$. The Mott-metal insulator transition is indicated by two transition lines labeled as U_1 and U_2. Between those two lines the system is in the coexistence regime where we can find metallic and insulating solutions. At the two transition lines U_1 and U_2 the Hubbard model undergoes a first-order phase transition, with both transition lines meeting at a second-order critical point $U_{\text{crit.}}$. As it is known in the theory of phase transitions a first-order transition can show a hysteresis leading to different values of the transition depending on the starting and the ending phase. In the case of figure 3.2 the phase transition line U_2 is found by taking the path from a metallic solution $U \to 0$ and increasing the value of U until the system is insulating according to the selections rules stated in (3.1). For U_1 the procedure is reversed: starting from an insulating solution, slowly lowering the interaction until a metallic solution according to equation (3.1) is found.

It is important to note that the phase diagram in 3.2 is produced for the half-filled case and by forcing the system to stay in the paramagnetic phase. This enforcement is done by taking the mean value of the up and down spin in each DMFT cycle, i.e. ,

$$\Sigma(\mathrm{i}\omega_n)_\uparrow = \Sigma(\mathrm{i}\omega_n)_\downarrow \, .$$

Since the metal-to-insulator transition line is below the Nèel transition temperature we are only able to see the MIT if spin symmetry in each iteration of the self-consistency loop is enforced. If this is not the case, the system will get into a magnetic ordered state leading to an anti-ferromagnetic insulating state.

2. Néel Temperature at half-filling

As stated before the phase diagram of the two-dimensional Hubbard model at half filling will be different if we give the system the freedom to undergo a magnetic ordering. This ordering takes place below a certain temperature, the so-called *Nèel temperature* T_N. This temperature is in fact artificially introduced due to the locality of the DMFT theory, since due to the Mermin-Wagner theorem the transition temperature is $T_N = 0$ for the two-dimensional case. In general the Mermin-Wagner theorem states that a two-dimensional system with short range correlations can not show a spontaneous symmetry breaking for finite temperatures. For the square lattice

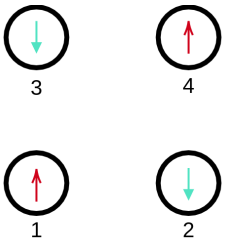

Figure 3.3.: Sketch of enforcing the antiferromagnetic ordering on a 2×2 cluster leading to a 2×2 local Green's function. The spin asymmetry is imposed by choosing the spin indices of the DMFT self-energy according to the antiferromagnetic ordering.

the forbidden symmetry breaking can be interpreted in an absent magnetic ordering for finite temperature.

In the DMFT where the unit cell consists of one site, we have to expand the unit cell in order to distinguish the magnetically ordered, from the disordered state. First of all it should be noted that the two phases are labeled by looking at the local magnetic properties of the lattice sites in consideration by simply calculating the value

$$m = \langle n_\uparrow \rangle - \langle n_\downarrow \rangle \ , \tag{3.2}$$

where the antiferromagnetic and disordered phase are defined by

$$m = \begin{cases} > 0.1, & \text{antiferromagnetic} \\ < 0.1, & \text{unordered magnetic phase} \end{cases} \ . \tag{3.3}$$

The magnetization strength m is calculated on each site of an $X \times X$ cluster. The procedure to calculate the Nèel transition temperature is the following:

1. Create the local Green's function of the $X \times X$ cluster using the DMFT self-energy for each site of the cluster imposing antiferromagnetic ordering.
2. Take the local part of one site of the $X \times X$ cluster as the starting point of the DMFT impurity.
3. Solve the DMFT impurity problem.
4. Calculate the magnetic ordering on each site of the $X \times X$ cluster using the new DMFT self-energy while implying antiferromagnetic ordering.
5. Check the magnetic state of the system according to equation (3.3)
6. Repeat steps 1-5 with the new DMFT self-energy as a starting point.

During the self-consistency it is important to try to force the system into an antiferromagnetic ordering at the level of the local Green's function by alternating the spin of the DMFT self-energy. This is illustrated in the sketch 3.3 for a 2×2 cluster leading to a local Green's function of dimension 4. Taking the example of the 2×2 sketch in figure 3.3 the self-energy of the cluster is created by the DMFT self-energy in the following way

$$\Sigma(\mathrm{i}\omega_n)_\uparrow = \begin{pmatrix} \Sigma^{\mathrm{DMFT}}(\mathrm{i}\omega_n)_\uparrow & 0 & 0 & 0 \\ 0 & \Sigma^{\mathrm{DMFT}}(\mathrm{i}\omega_n)_\downarrow & 0 & 0 \\ 0 & 0 & \Sigma^{\mathrm{DMFT}}(\mathrm{i}\omega_n)_\uparrow & 0 \\ 0 & 0 & 0 & \Sigma^{\mathrm{DMFT}}(\mathrm{i}\omega_n)_\downarrow \end{pmatrix} \tag{3.4}$$

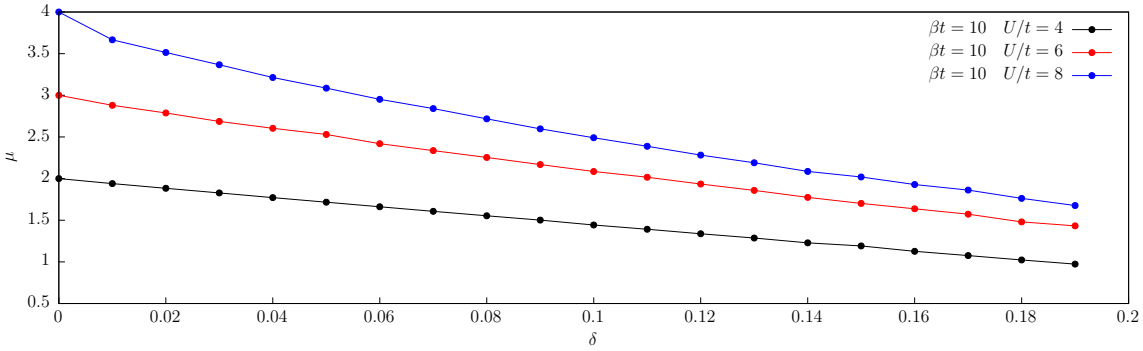

Figure 3.4.: Chemical potential μ as a function of the hole-doping δ for three different interaction values and a constant inverse temperature of $\beta t = 10$.

$$\Sigma(\mathrm{i}\omega_n)_\downarrow = \begin{pmatrix} \Sigma^{\mathrm{DMFT}}(\mathrm{i}\omega_n)_\downarrow & 0 & 0 & 0 \\ 0 & \Sigma^{\mathrm{DMFT}}(\mathrm{i}\omega_n)_\uparrow & 0 & 0 \\ 0 & 0 & \Sigma^{\mathrm{DMFT}}(\mathrm{i}\omega_n)_\downarrow & 0 \\ 0 & 0 & 0 & \Sigma^{\mathrm{DMFT}}(\mathrm{i}\omega_n)_\uparrow \end{pmatrix} \tag{3.5}$$

At this point it should be noted that the procedure of blowing up the dimension of the local Green's function is not the same as solving a whole cluster as an impurity problem. This can be also seen in the structure of the self-energy in (3.4), (3.5) where all off-diagonal parts are set to zero. The Nèel transition temperature together with the results of the MIT are shown in figure 3.2. The antiferromagnetic phase fully covering the transition lines of the first-order phase transition reveals the necessity of forcing the paramagnetic ordering in order to investigate the MIT in the two-dimensional Hubbard model using the DMFT approach.

3. Calculations away from half-filling

Up to now all DMFT results refer to the half-filled case, in this section, DMFT calculations for an average density of $\langle n_\uparrow \rangle + \langle n_\downarrow \rangle \neq 1$ are investigated. The system is called hole-doped if the density per site δ is less than zero and electron-doped if it is larger than zero

$$\delta = 1 - (\langle n_\uparrow \rangle + \langle n_\downarrow \rangle) \,. \tag{3.6}$$

In DMFT the parameter to control the doping of the system is the chemical potential μ. An analytical formula to chose the chemical potential is only known for the half-filled case, hence the chemical potential for a given hole-doping δ is calculated numerically. This can be done by doing a simple bisection of the local Green's function $G_{\mathrm{Loc}}(\mathrm{i}\omega_n, \mu)$ in terms of the chemical potential and an initial guess, for example $\mu = U/2$. Figure 3.4 shows the chemical potential in dependence of the doping δ, where we observe its reduction when the doping is increased.

The doped system exhibit a rich physical behavior. First we investigate how a half-filled system showing an insulating behavior changes when we apply hole doping. In the right panel of figure 3.5 we show the spectral function for the half-filled case ($\delta = 0$) and three different hole-doped cases. For the doped spectral function in figure 3.5 we observe a non-symmetric behavior between hole-like ($\omega < 0$) and particle-like excitations ($\omega > 0$). This symmetry is preserved in the half-filled model but is broken as soon as doping is present [49]. Moreover we observe the asymmetry between hole and particle features in the zero-frequency, i.e. $\omega = 0$,

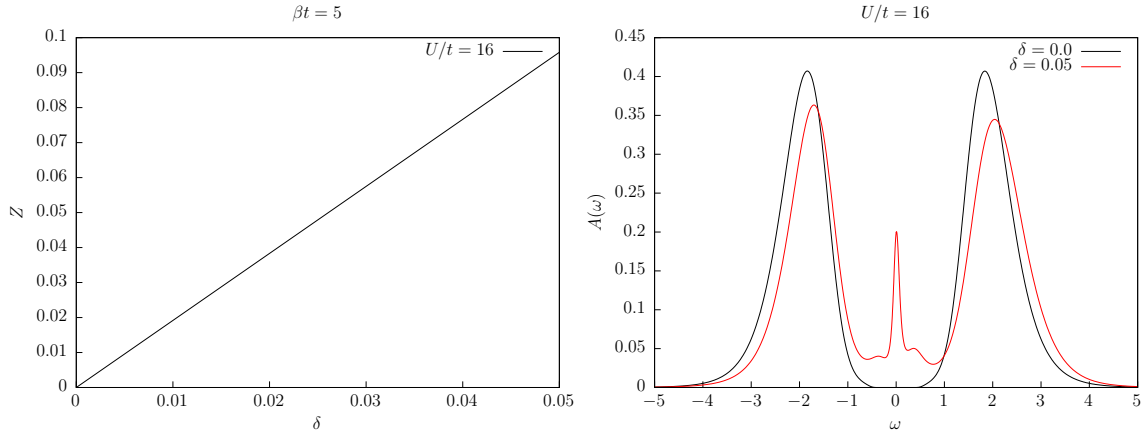

Figure 3.5.: Left: Quasi-particle weight for different doping values and interaction $U/t = 16$ for the inverse temperature $\beta t = 5$. Right: Local spectral function for the two-dimensional square lattice with different doping.

regime, where for the hole sector we see a sharp, convex behavior, while the particle sector around $\omega = 0$ decays more slowly in a concave way.

For the half-filled case we distinguished the insulating states of the system and the metallic ones by comparing the values of the local Green's function at an imaginary time of $G(\tau = \beta/2)$ and then applying the conditions (3.1). While $G(\tau = \beta/2)$ is a good approximation for the spectral function at $A(\omega = 0)$ and can be used for the half-filled case to distinguish quasi-particle peak structures and gaped spectral functions we run into problems while applying this exact thought process to decide weather a doped system is insulating or metallic since sharp excitations close to $A(\omega = 0)$ are visible. Another way to distinguish the two phases can be found by calculating the so-called quasi-particle weight

$$Z = \left(1 - \frac{\partial \mathrm{Im}\Sigma(\mathrm{i}\omega_n)}{\partial \mathrm{i}\omega_n}\Big|_{\mathrm{i}\omega_n \to 0}\right)^{-1} . \tag{3.7}$$

For the metallic case $U \to 0$ the quasiparticle weight is 1, while Z vanishes as the metal-insulator transition is reached. For different temperature and interaction values the quasiparticle weight is shown in the left panel of figure 3.5. A first observation indicates the result that only the half-filled case ($\delta = 0$) is able to show an insulating state, since $Z(\delta \neq 0) \neq 0$. The left panel of Figure 3.5 shows that it is not only possible to switch between metallic and insulating states by changing the interaction U like in the half-filled case but can also be obtained by hole-doping and therefore changing δ.

IV. Cellular Dynamical Mean-Field Theory

In the following we discuss the theory of the cellular dynamical-mean field theory (CDMFT) which is an extension of the DMFT impurity in real-space and apply this approach to solve the two-dimensional Hubbard model. Besides investigating the differences and advantages compared to DMFT we also calculate two-particle response functions.

1. CDMFT self-consistency equation

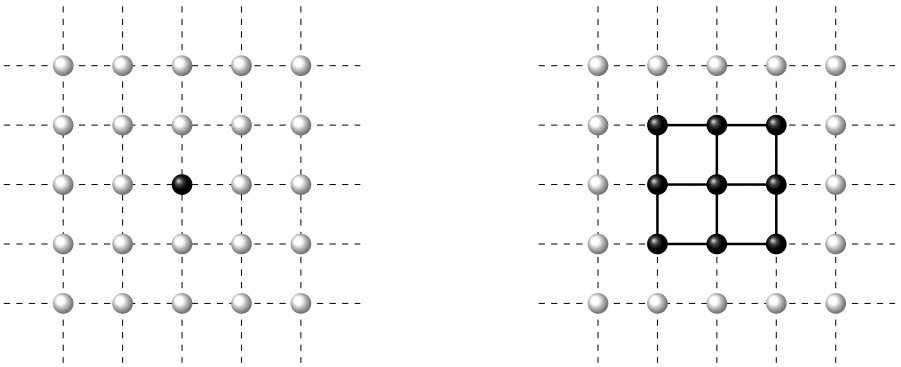

FIGURE 4.1.: Quadratic clusters with N lattice sites. The left panel shows the DMFT case with $N = 1$, whereas the right one corresponds to a 3×3 cluster.

The cellular dynamical mean-field theory uses the idea of expanding the impurity in real-space adding more sites to the local impurity than the single-site approach of DMFT. Even though the theory is still only be able to capture local effects, it includes off-diagonal parts of the self-energy between sites inside the impurity. This will have huge impact on all observables which will be discussed in later parts of this section. In terms of the theoretical description, DMFT and CDMFT are using the same self-consistency equations with the difference that CDMFT treats the self-energy and therefore also the local Green's function as tensor objects. The Weiss field then reads

$$\mathcal{G}^{-1}_{i,j,\sigma}(\mathrm{i}\omega_n) = \sum_k \left[(\mathrm{i}\omega_n + \mu)\delta_{i,j} - \varepsilon_{i,j}(\mathbf{k}) - \Sigma_{i,j,\sigma}(\mathrm{i}\omega_n)\right] + \Sigma_{i,j,\sigma}(\mathrm{i}\omega_n)\ . \tag{4.1}$$

Figure 4.1 shows the transition from a single-site unit cell like in the DMFT case to an 3×3 cluster impurity including multiple sites inside the unit cell. In equation (4.1) a matrix structured dispersion relation $\varepsilon_{i,j}(\mathbf{k})$ appears which cannot be directly replaced by the DMFT dispersion of the two-dimensional square lattice $\varepsilon(\mathbf{k}) = -2t(\cos(k_x) + \cos(k_y)$. In fact the easiest way to obtain the dispersion relation of $\varepsilon_{i,j}(\mathbf{k})$ is to draw the first unit cell and the surrounding neighboring cells and label all possible hopping processes, which in the case of a unit cell with multiple sites leads to two different hopping terms: The ones which are completely local inside the unit cell and the ones who have a connection between the first unit cell and one of the

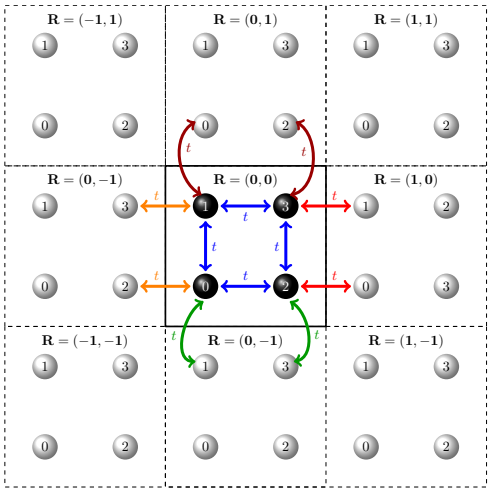

$$\varepsilon(\mathbf{k}) = \begin{pmatrix} 0 & t + te^{-iky} & t + te^{-ikx} & 0 \\ t + te^{iky} & 0 & 0 & t + te^{-ikx} \\ t + te^{-ikx} & 0 & 0 & t + te^{iky} \\ 0 & t + te^{ikx} & t + te^{iky} & 0 \end{pmatrix}$$

Figure 4.2.: Sketch of the dispersion relation of a unit cell of size 2×2 on the square lattice.

surrounding cells. For the 2×2 unit cell the graphical approach, as well as the matrix structure of the dispersion relation is shown in figure 4.2.

2. Periodization schemes

Despite CDMFT being a local theory like DMFT it contains information of correlations inside the impurity manifesting in non-vanishing off-diagonal parts of the self-energy. Besides comparing local quantities of DMFT and CDMFT like the onsite spectral function, we can take a look at the momentum dependent spectral function $A(\omega, k)$ obtained by the analytical continuation of the lattice Green's function

$$G(i\omega_n, \mathbf{k}) = \left[(i\omega_n + \mu) - \varepsilon(\mathbf{k}) - \Sigma(i\omega_n, \mathbf{k})\right]^{-1} . \tag{4.2}$$

It is critical to note that the matrix indices in equation (4.2) are no longer needed compared to the impurity Green's function in equation (4.1) since $G(k, i\omega_n)$ is the lattice Green's function, while the self-energy is treated as a momentum dependent object. For the DMFT approach we would swap the k-dependent self-energy in equation (4.2) with the local one obtained by solving the DMFT selfconsistency, i.e., $\Sigma(k, i\omega_n) \to \Sigma(i\omega_n)$. In CDMFT we still have a purely local self-energy but non-zero off-diagonal parts. The correlation between sites in real-space inside the impurity $\Sigma(R, i\omega_n)$, allow for a Fourier transformation into the momentum space $\Sigma(k, i\omega_n)$. After converging a CDMFT calculation, this procedure is done once as a post process at the end of the self-consistency loop and is called periodization. If one would use the periodization method for every step of the self-consistency loop the self-energy eventually will get into troubles satisfying the causality [50, 51]. In general a periodization of an object Q is done via

$$Q(\mathbf{k}, i\omega_n) = \frac{1}{N} \sum_{i,j}^{N} Q_{i,j}(i\omega_n) e^{-i\mathbf{k}(\mathbf{R}_i - \mathbf{R}_j)} . \tag{4.3}$$

In the literature different physical quantities Q are used to produce a lattice Green's function via equation (4.3). Besides the direct periodization of the self-energy, i.e., $Q = \Sigma$, it is often useful to take the cumulant [52]

$$M(i\omega_n) = \left[i\omega_n + \mu - \Sigma(i\omega_n)\right]^{-1} \tag{4.4}$$

to perform the periodization. Another choice for Q consists of taking the local impurity Green's function but is not discussed in this work.

According to [52] we proceed with the choice of the cumulants M defined in equation (4.4) and investigate how the size $N \times N$ of our impurity affects the results in terms of the lattice Green's function after a periodization. In order to proper visualize our results we show the momentum resolved spectral functions along a closed path in the first Brillouin zone

$$\Gamma = (0,0) \rightarrow X = (\pi,0) \rightarrow M = (\pi,\pi) \rightarrow \Gamma = (0,0)$$

for different impurity cluster sizes $N \times N$, which can be found in figure 4.3. Starting from the DMFT solution in the first row up to cluster sizes $N = 9 \times 9$ in the last row, we can see an evolving local spectral function. While the DMFT solution is still in the metallic phase characterized by a distinct quasi-particle peak at $\omega = 0$, we see a gap opening while enlarging the cluster size. This indicates a Mott metal-to-insulator transition for cluster sizes $N \rightarrow \infty \times \infty$ since a MIT is reflected in the spectral function $A(\omega)$ as a spectral weight transfer from a sharp quasi-particle peak to incoherent Hubbard bands.

So far the discussion of figure 4.3 contains only the information's of the local lattice Green's function. Starting for smaller cluster sizes $N \times N$ with $N = 1, 2, 3, 4$ we see the spectral function crossing the Fermi surface, i.e. $\omega = 0$, at the high symmetry point $X = (0, \pi)$ and at the point $(\pi/2, \pi/2)$. Between $N = 5$ and $N = 7$ the momentum resolved spectral function appears to show a gap opening at X while a crossing of the Fermi surface is still present at the point $(\pi/2, \pi/2)$. This momentum dependent gap opening can hint to the so-called the pseudo-gap phase but is not further investigated in this work. For the largest clusters in consideration, i.e. $N = 8, 9$, the spectra shows also an opening of the gap at the point $(\pi/2, \pi/2)$, leaving the regime of a momentum selective gap opening to the point of an insulating state for every k value.

To complete our analysis about the spectral function in the cumulant periodization scheme we show local Green's function data of a CDMFT calculation with size 7×7 for different inverse temperatures βt and interaction values U/t in figure 4.4. By fixing the cluster size we can observe a clear behavior of the spectral weight at the Fermi energy at $\omega = 0$, while lowering the temperature a gap is opening in the local spectral function (upper panel of figure 4.4). Leaving the temperature constant, an increasing interaction U/t will lower the spectral weight at the Fermi energy ε_F and eventually lead to a gap opening in the spectrum (lower panel). The statement can be adopted for all cluster sizes $N > 1$ and is universal for the cumulant periodized lattice Green's function.

3. Phase diagram at half-filling

The previous section and the discussion of the periodization method set the stage to calculate the phase diagram for the Mott metal-to-insulator transition in the CDMFT framework. Besides comparing the MIT of different cluster sizes $N \times N$ with DMFT we will also investigate the effect of large clusters on the Néel temperature. Using the same procedure as discussed for the DMFT results in the former chapter, we distinguish the metallic and insulating phase by taking a look at the imaginary time local lattice Green's function $G(\tau = \beta/2)$ obtained using the cumulant periodization method. For cluster sizes $N = 2, 4, 6, 8$ and $N = 1$ (DMFT) the phase transition lines are shown in figure 4.5. For $N = 4, 6, 8$ we can find a threefold degenerate point

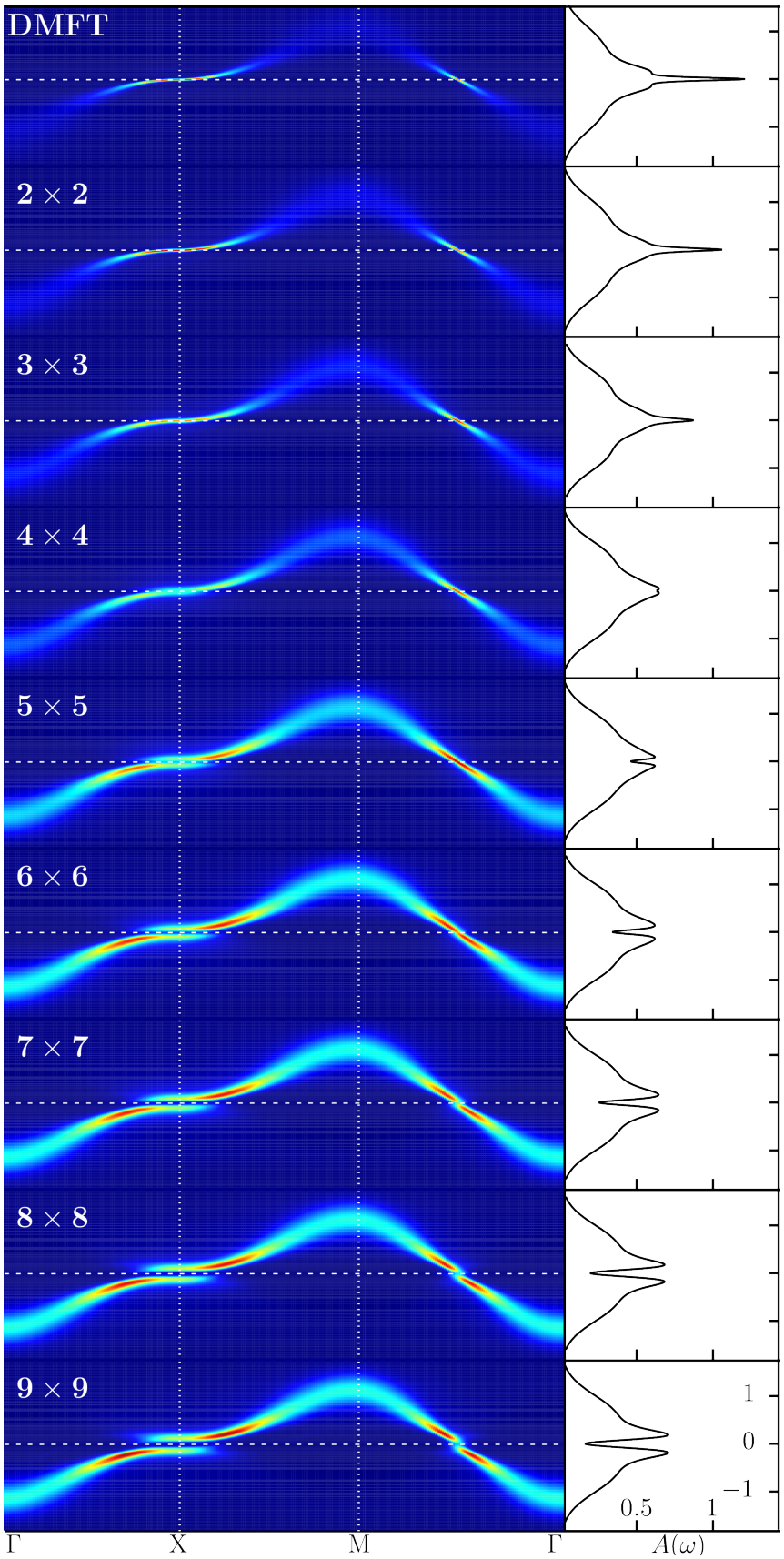

Figure 4.3.: Left panel: Momentum resolved spectral function of the lattice Green's function obtained by using the cumulant (4.4) periodization (4.3). For each k-point along a closed path Γ: $(0,0)$ – X:$(\pi,0)$ – M(π,π) – Γ: (0,0) in the first Brillouin zone a spectral function was produced by the use of the analytical continuation. On the right panel the spectral function of the local lattice Green's function is shown. For all calculation the following parameters are used: $\beta t = 12.5$ and $U/t = 4$ while the different impurity cluster sizes N are indicated at each row as a label.

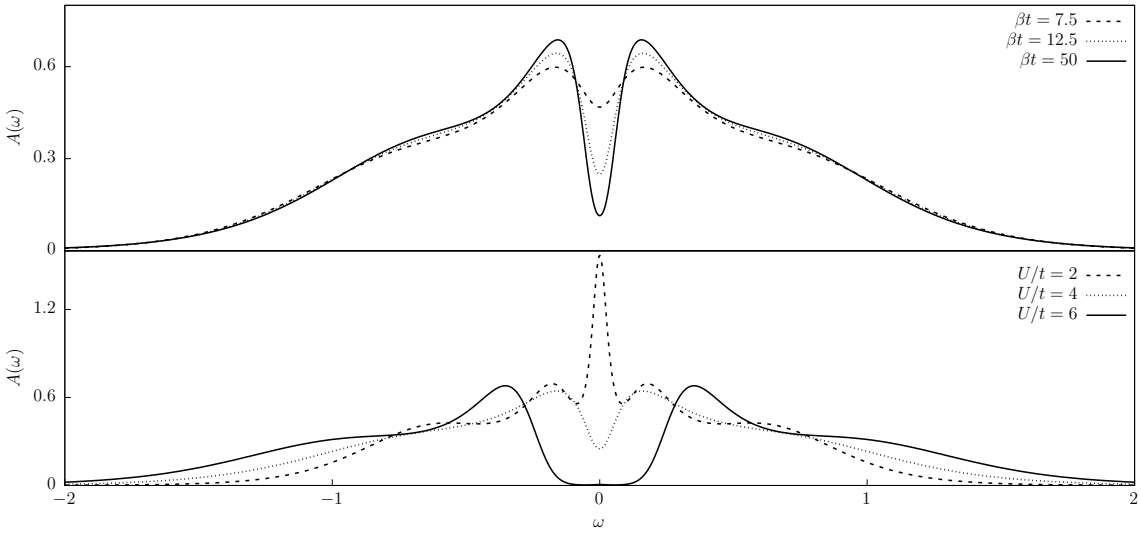

Figure 4.4.: Spectral function of the local lattice Green's function obtained by the cumulant periodization method for $N = 7$, for different inverse temperatures and fixed interaction of $U/t = 4$ (upper panel), and for different values of U and a fixed inverse temperature $\beta t = 12.5$ (lower panel).

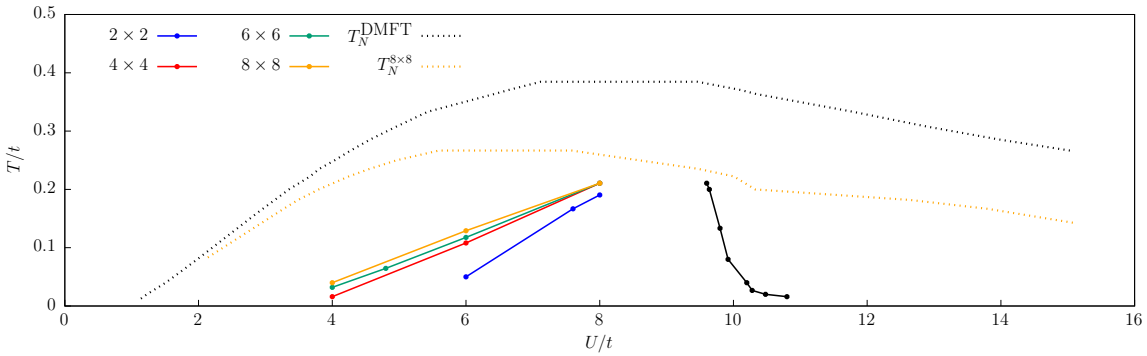

Figure 4.5.: Phase diagram of the MIT for different cluster sizes using a cumulant periodization. Besides the transition lines obtained in a paramagnetic constraint approach, the Neel transition lines for the DMFT and the largest cluster $N = 8$ are shown, indicating an ordered magnetic phase.

at roughly $U/t = 8$ and $T/t = 0.2$ where all cluster sizes show a phase transition. Lowering the temperature we see a variation of the phase transition lines in dependence of the cluster sizes. According to former calculations in the thermodynamic limit $T \to 0$ [53–56], the system undergoes a phase transition at a critical interaction value $U_c = 0$. This is in agreement with our results, where we can observe a lowering of the critical value for increasing the size N. Even the smallest cluster in consideration, i.e. 2×2, shows a completely different transition line compared to the DMFT results. While we find an increasing interaction value U_c for the DMFT calculations for lower temperatures, the behavior of CDMFT inverts the slope.

Even though the phase transition changes drastically for the CDMFT results it is still only possible to find the MIT for calculations done in the paramagnetic forced regime since the dome of a magnetically ordered phase completely enfolds the metall-to-insulator transition lines. The presence of the Nèel transition line in CDMFT is a direct measurable value in comparison to the DMFT calculation, where the impurity is made artificially larger while setting all off diagonal elements of the self-energy to zero, see equations (3.4) and (3.5). For an commensurable two-dimensional cluster impurity, i.e. an even number of N for the cluster size $N \times N$, we allow

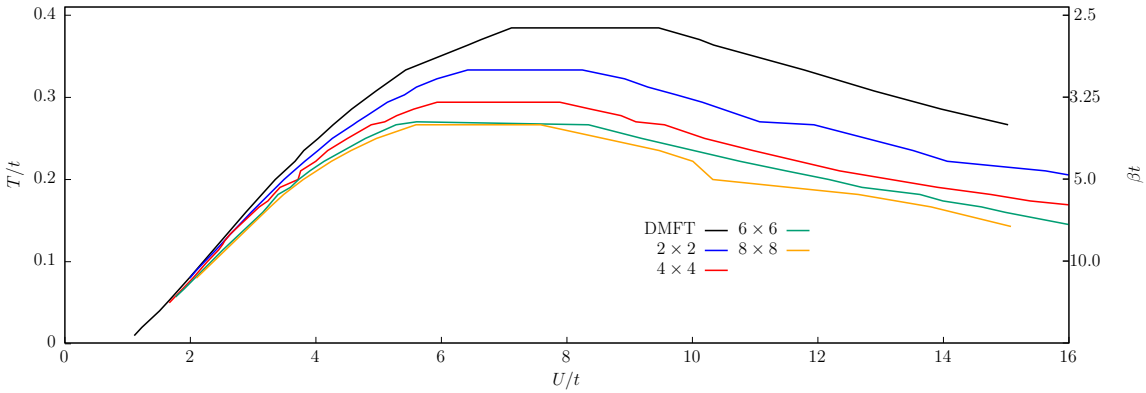

Figure 4.6.: Neel phase diagram indicating the Neel transition temperature for different cluster sizes N in the CDMFT approach. The black line indicates the transition temperature obtained using DMFT.

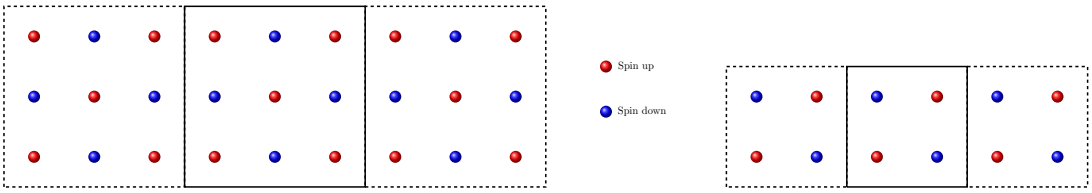

Figure 4.7.: Left: 3×3 representing all clusters with an odd number of total sites and local anti-ferromagnetic ordering. Placing the cluster back as a unit cell into the cluster leads to neighboring sites with same spin, and therefore a destruction of the checkerboard ordering. Right: 2×2 cluster which is the smallest candidate for an even cluster. Placing the antiferromagnetic ordering of the cluster back into the lattice, the checkerboard ordering is preserved.

the impurity to take on a checkerboard ordered magnetic phase, while an odd number of N leads to questions about how the system is able to become magnetically ordered while being frustrated. This is best represented in a visual manner shown in figure 4.7, where a continuous replacement of the whole lattice is done by using the magnetic ordered impurity. This will lead to neighboring sites with same spin occupations. For this reason only calculations with an even number of N are shown in the phase diagram in figure 4.5 as well as in the Neel diagram 4.6. According to the Mermin-Wagner theorem the expectation for a perfect CDMFT calculation with an infinite cluster $N \times N = \infty \times \infty$, representing the exact lattice as an impurity, would lead to a Nèel temperature of $T \to 0$. Even though we can converge CDMFT calculations for cluster sizes up to 8×8, we still are in a regime where the cluster represents an approximation for the whole lattice, manifesting into non-vanishing antiferromagnetic domes in 4.6 while for larger values of U/t the transition temperature is clearly lowered while increasing the cluster size.

4. Symmetry breaking in CDMFT

In the following we discuss the symmetry breaking occurring in the approach of cellular dynamical mean-field theory. By choosing an impurity consisting of multiple sites we in fact break the translation invariance of the original lattice. This can be easily understood if we think of a simple example which in this case is a unit cell of size 3×3 cut out from the original lattice. First we note that this is indeed a unit cell of the whole lattice and preserves the translational symmetry. The breaking of this symmetry arises when we define our impurity

problem as the 3×3 cluster and solve this impurity in the self-consistent CDMFT approach, which in a figurative way means we surround the impurity by an electronic bath allowing hopping processes of electrons from the bath to the impurity and vice versa. Now the eight sites forming the border of the impurity encircling the center site have a direct waypoint to the electronic bath, while the center site can only gain or emit an electron from the thermal bath by an indirect hopping process including at least one of his neighboring sites and therefore we expect a different local behavior on the center site compared to all the other eight sites for the 3×3 impurity. We show the breaking of the translational invariance of the CDMFT approach in figure 4.8 by taking a look at the local spectral function on each site of a CDMFT calculation with the size 8×8. Even though translational invariance is broken in the CDMFT case, we still preserve lattice symmetries like the rotation of the whole problem by $\pi/2$, this is why only the upper right quadrant of the impurity is shown in figure 4.8 where the upper left corner indicates sites with the same local properties due to symmetry reasons by the same color. In figure 4.8 three different types of interaction can be found for the inverse temperature of $\beta t = 12.5$ distinguished by different dashed lines in each panel. Besides a weak coupling interaction value of $U/t = 2$ and a strong coupling $U/t = 12$ we show results of an intermediate interaction regime $U/t = 4$. In this intermediate coupling regime we can clearly see a strong variation for the local spectral function between the center site (bottom left panel) and the edge site (upper right panel). While the edge site still resolves a quasi-particle peak, the center site already transferred his spectral weight to form Hubbard bands which reflects into a gap opening at the Fermi level $\omega = 0$. If we compare this result to the original translational invariance of the lattice, which means in the case of infinite cluster size all sites have to show the same onsite spectral function, we can clearly see a breaking of this symmetry for $U/t = 4$. Thinking back to the discussion of the periodization which indeed assumes that all sites are equal inside the impurity to restore the translational invariance for CDMFT calculation we assess that this method is not a good choice since the local spectral functions clearly show an insulating trend while moving from the border to the center of the cluster in figure 4.8, at least if we are in the intermediate coupling regime of $U/t = 4$.

To show how our CDMFT calculations are affected by edge effects, we can define a value which is a measure of the deviation of the local spectral functions on each site compared to the center site at the energy $\omega = 0$

$$A_v(|\mathbf{R}|) = |A(\omega = 0, \mathbf{R} = \mathbf{0}) - A(\omega = 0, \mathbf{R})| \ . \tag{4.5}$$

This value is shown in figure 4.9 for three different inverse temperatures $\beta t = 2.5, 5.0, 12.5$ and interaction values of $U/t = 2, 4, 6$ for CDMFT calculations of size $N \times N$ with $N = 4, 6, 8$, providing a measure of the breaking of the translational invariance. The different cluster sizes are indicated by a color coding, while for each row the inverse temperature is constant varying the interaction value from left to right in ascending order. In all shown cases we can see that the edge site shows a non-zero value by the definition of A_v in (4.5). In the following we define the so-called border variance A_v^B by the value of $A_v(|\mathbf{R}_{\max}|)$ with the maximum distance $|\mathbf{R}_{\max}|$ available. For the weak coupling regime $U/t = 2$ (first column) the border variance A_v^B does not differ much while decreasing the temperature. Comparing the absolute values of $U/t = 2$ for every temperature with the ones of larger interaction also gives an insight that the symmetry breaking for the small coupling regime is negligible. The central column representing the intermediate coupling regime of $U/t = 4$ possesses a large value for A_v^B at each temperature shown. The border variance becomes visible larger for the cluster sizes 6×6 and 8×8 by

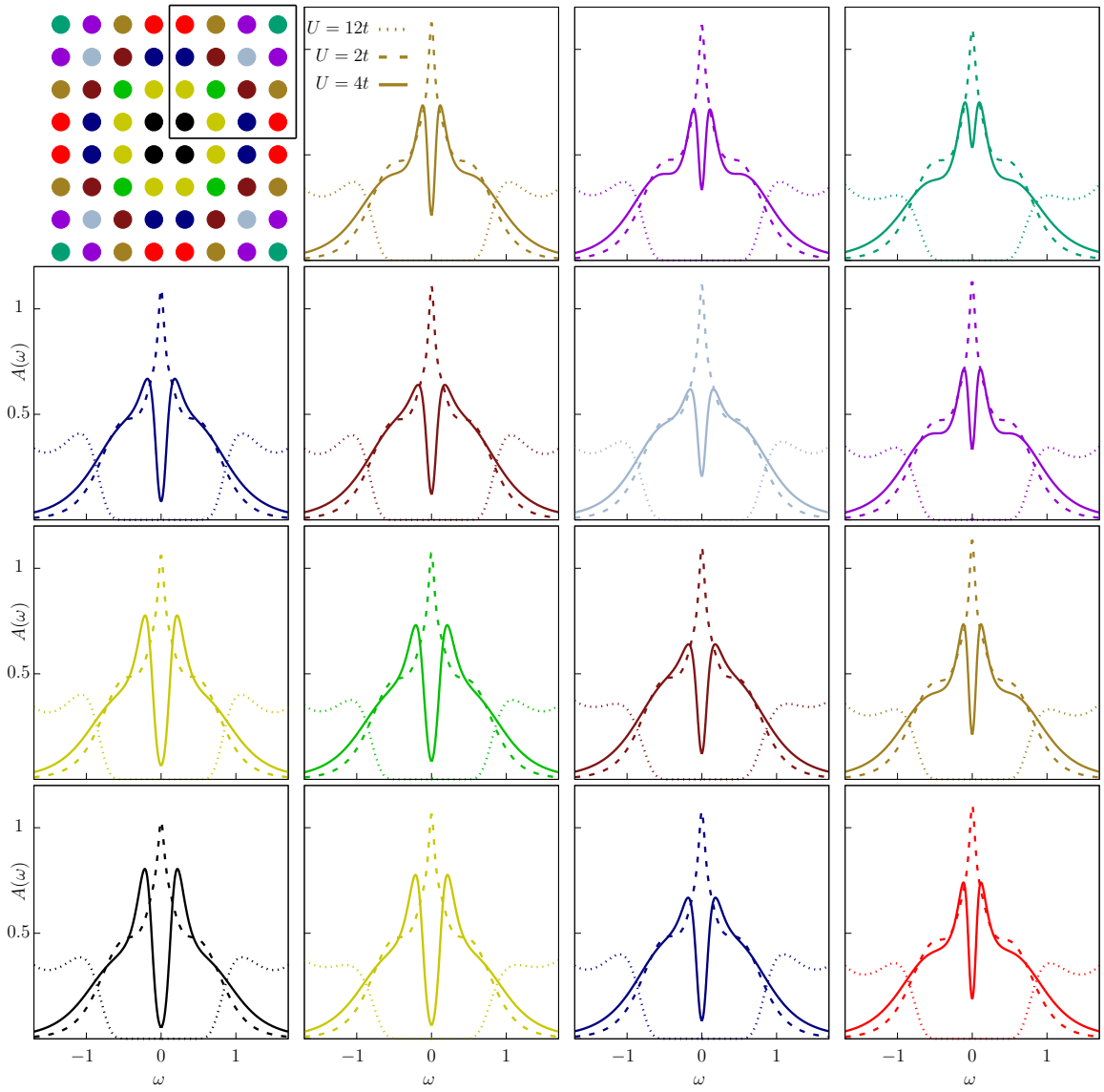

Figure 4.8.: Local spectral functions for the cluster size of 8×8, three different interaction values U/t and an inverse temperature of $\beta t = 12.5$. The upper left panel shows a color coding for the shown sites, where same sites due symmetry reasons are indicated by the same color. For the intermediate interaction value $U/t = 4$ a clear trend towards an insulating state is visible while moving from the border to the center.

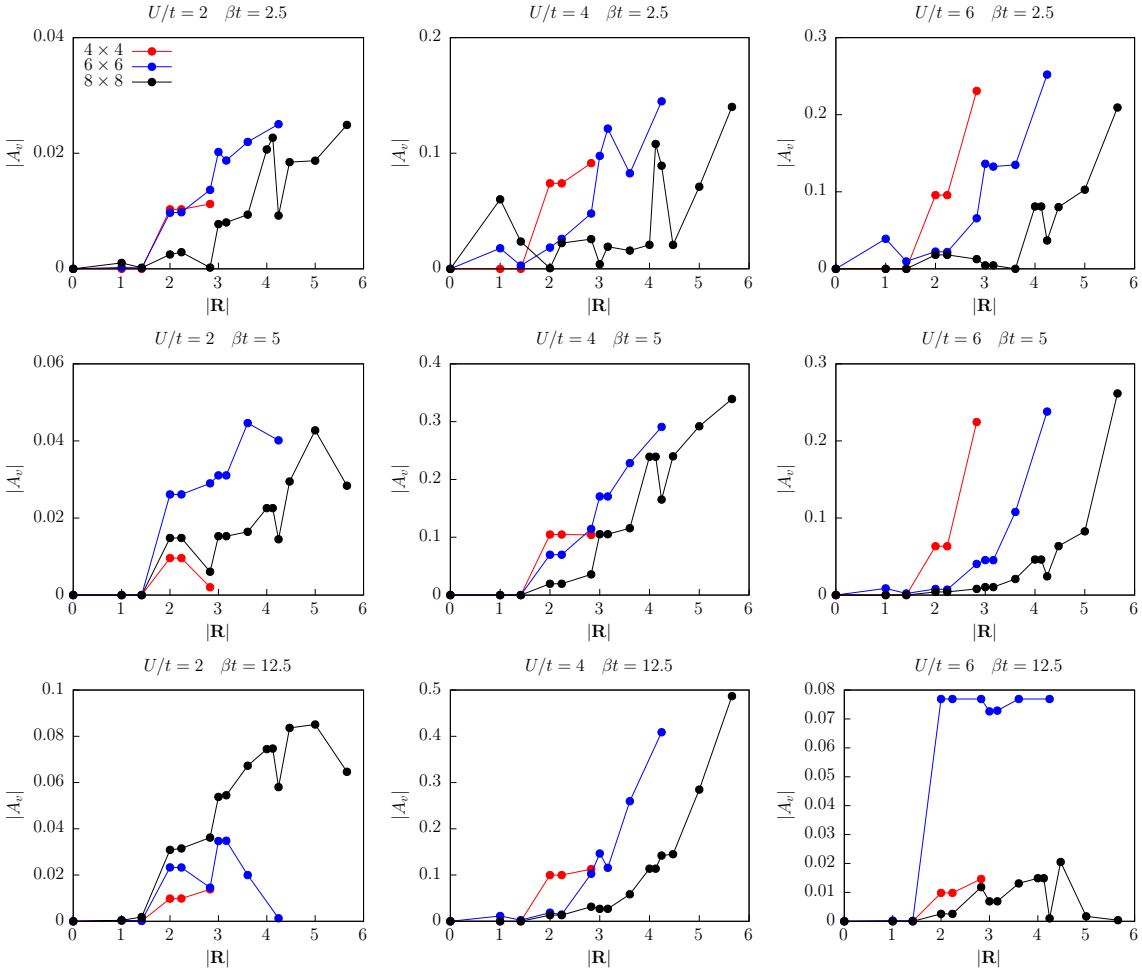

Figure 4.9.: Difference of the local spectral function inside the cluster $|A_v|$ defined in equation (4.5). Each column represents a different interaction value in ascending order $U/t = 2, 4, 6$, while every row indicates a different inverse temperature of $\beta t = 2.5, 5, 12.5$.

decreasing temperature (from top to bottom). The 4×4 cluster also shows a non-vanishing value for distances $|R| > \sqrt{2}$ but also appears to be much less temperature dependent. The third row representing a strong coupling regime of $U/t = 6$ shows the same behavior for the inverse temperatures of $\beta t = 2.5, 5$ as for the $U/t = 4$ case, while for the parameters $U/t = 6, \beta t = 12.5$ (right lower panel) the definition of A_v breaks down. The expected behavior for the border variance in this case would be an increase of the absolute value, or at least the same value as for higher temperatures, this assumption is not met for every cluster size. One explanation for this unexpected behavior could be that the self-energy for the parameters in consideration does not decay to zero inside the impurity cluster and therefore leads to mean-field like behavior of the system. This will be discussed more in details in a later section of this work. In general we can state that for each panel (excluding $U/t = 6, \beta t = 12.5$) the real-space range where A_v is small is dependent on the cluster size. This can be interpreted by labeling only the border of the cluster as *bad* sites, which violate the translational invariance of the cluster. Of course, we find more sites not violating the symmetry of the lattice in CDMFT calculations for larger cluster sizes $N \times N$. At this point we mention that A_v in equation (4.5) does not make a statement on the site-dependence of the local spectral function.

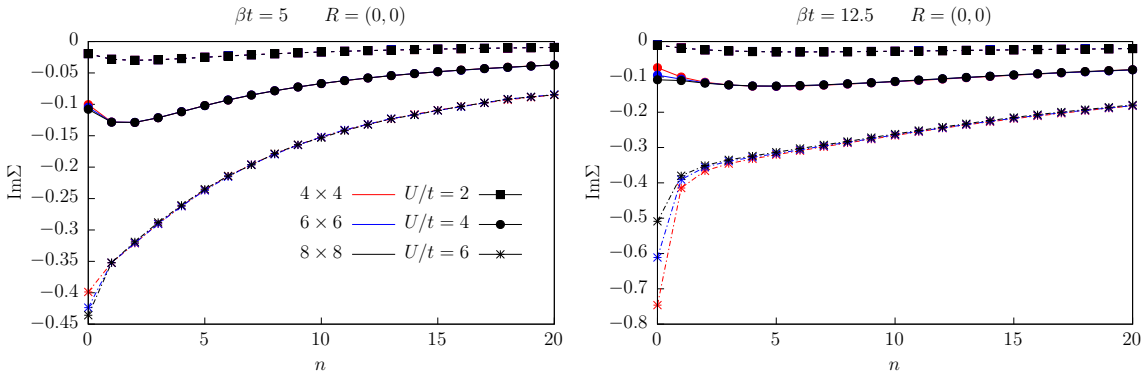

Figure 4.10.: Onsite self-energy for three different cluster sizes of the center site $R = (0,0)$ of the cluster, for two different inverse temperatures $\beta t = 5$ (left) and $\beta t = 12.5$ (right) and three different interactions of $U/t = 2, 4, 6$.

5. Extrapolation of the self-energy

In this section we investigate the extrapolation of the self-energy for infinite cluster sizes by taking results for calculations performed with $N = 4, 6, 8$. In all discussed CDMFT results up to this point we could detect a cluster-size dependence of a certain observable. In the case of the self-energy we first check more carefully how the cluster size N influences the self-energy. To do this, we plot the onsite self-energy of the center site $R = (0,0)$ for different cluster sizes $N \times N$, two different inverse temperatures $\beta t = 5, 12.5$ and interactions of $U/t = 2, 4, 6$, which can be seen in figure 4.10. A first observation leads to the conclusion that for the high frequency part of the self-energy the different cluster sizes $N \times N$ are indistinguishable and therefore only the low frequency regime is of interest. This is true for all shown interaction values as well as for both temperatures. Focusing on the first Matsubara frequency $n = 0$ we see that the self-energies are clearly dependent on the cluster size for $U/t = 4$ and $U/t = 6$. For the small coupling regime $U/t = 2$ in both displayed temperatures the results look converged in terms of cluster size. Excluding the small coupling regime $U/t = 2$ in the following part of the discussion, we state that for a constant interaction value the difference of the first Matsubara frequency in dependence of the cluster size become larger, the lower the temperature gets. This is an expected behavior since we know that long range correlation become more important in low temperature regimes leading to problems for smaller clusters since there the self-energy is not fully decayed within the cluster.

So far we have discussed that the low frequency regime of the self-energy can exhibit a dependence of the cluster shown, while for large Matsubara frequencies $n > 10$ the data appear to be converged in the cluster size. The lowest Matsubara frequency for $U/t = 6$ and $\beta t = 12.5$ (dashed stars in lower panel of figure 4.10) provides a good visual example. While the lowest cluster size 4×4 has a value of ≈ -0.75 the self-energy takes a values of ≈ -0.6 for 6×6 and gets even closer to zero for 8×8 showing a value of ≈ -0.5. Taking this observation to the next level we plot the values for each size N of a given Matsubara point n and check the functional dependence of the two variables. For the two lowest frequencies $n = 0, 1$ at an inverse temperature $\beta t = 12.5$ and an interaction of $U/t = 6$ this behavior is shown in figure 4.11. As it can be seen, the results of the self-energy plotted over the inverse cluster size $1/N$ show a linear behavior. We hence extrapolate our results, following the spin-wave theory of finite-size correlations scale with $1/N$ [57] which seems to be also applicable for the two-dimensional Hubbard model dominated by antiferromagnetic spin fluctuations, in this case the self-energy

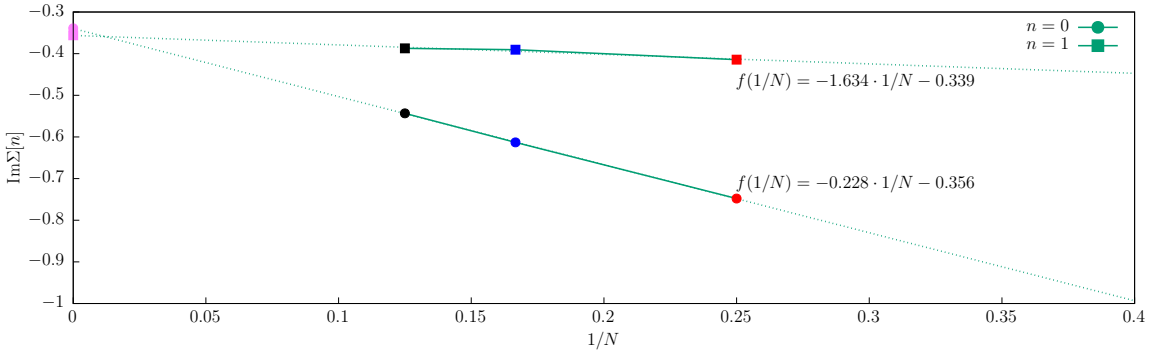

Figure 4.11.: The two lowest positive Matsubara frequencies of different cluster sizes $N \times N$ indicated by a color code plotted over the inverse size $1/N$ for the parameters of $\beta t = 12.5$ and $U/t = 6$. A linear fit can be done to extract the self-energy for $N \to \infty$ which is represented by the crossing point of the linear fit and the y-axis.

for each Matsubara frequency, to cluster sizes $N \times N = \infty \to \infty$ which is done in the following procedure:

1. Take the self-energy of CDMFT calculations for $N \times N$ with $N = 4, 6, 8$ at the same real-space position (in reference to the cluster center).

2. For each Matsubara frequency fit a linear function

$$f(1/N) = \frac{a}{N} + b \,, \tag{4.6}$$

on the data points and take the fit parameter b in equation (4.6) as the self-energy value for a cluster size of $\infty \times \infty$.

It should be noted that the imaginary and real parts of the self-energy should be treated separately, in which case we have to do two independent linear fits for each Matsubara point. In all discussions the smallest cluster with an even number of sites, i.e. 2×2, is dropped out in the procedure of fitting the data (these are simply to small to be cast in the form of the fit function). In the following we will treat the extrapolated self-energy as an 8×8 matrix. Since the largest cluster available for the extrapolation in this work is 8×8 we have to elaborate how to generate an extrapolated self-energy in more detail. We start by noting that all real-space distances of the 4×4 cluster are available in CDMFT calculation for sizes of 6×6 which on the other hand has real-space distances within the 8×8 case. Since the extrapolation is a procedure of taking a linear fit for $1/N$ we can do the extrapolation of all real-space distances inside the 4×4 cluster for three points, while all sites outside the 4×4 cluster but within the 6×6 cluster can be still extrapolated to an infinite size with the linear fit using the data points of the sizes $N = 6, 8$. In the case of real-space coordinates only available in the largest 8×8 cluster, an extrapolation is not possible, since only one data point is directly accessible. In this case we use the approximation of $\Sigma^{\mathrm{ext}} = \Sigma^{8\times 8}$. It is important that the extrapolation is not limited to onsite self-energies but also usable for all off-diagonal parts $\Sigma_{i,j}$ for $i \neq j$. A schematic sketch of the extrapolation procedure is shown in figure 4.12.

In order to estimate how good our extrapolation method works, we are showing CDMFT data for the extrapolated self-energy, as well as the self-energy for 8×8 cluster together with numerically exact DiagMC calculations [28, 55] for an interaction $U/t = 4$ and an inverse temperature $\beta t = 5$ for the center onsite self-energy $\Sigma[n, R = (0, 0)]$ as well as the nearest

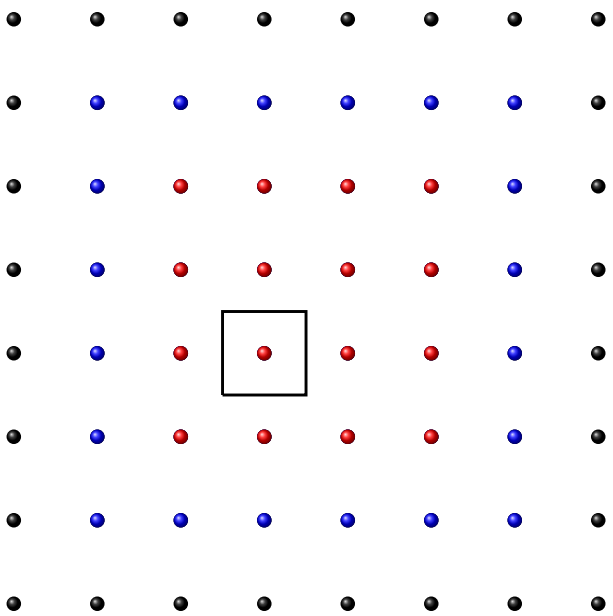

Figure 4.12.: Schematic sketch of the procedure to obtain the extrapolated self-energy with maximum real-space distances available in CDMFT calculations with the maximum size of 8×8. The center site is encircled by a square. All sites of the 4×4 cluster are indicated by a red coloring, blue indicate sites outside of 4×4 but inside the 6×6 cluster and the black sites are only available within the 8×8 cluster. For all inner (red) sites we have three data points to do the extrapolation, in the blue regime we still can do an extrapolation with two data points and for the black sites we approximate the extrapolated self-energy by the 8×8 cluster.

neighbor correlation $\Sigma[n, R = (1, 0)]$. For the onsite part of the self-energy we can see an agreement of the numerically exact results of DiagMC and the extrapolated self-energy inside errorbars, while the largest CDMFT self-energy of the 8×8 cluster still shows a clear deviation to the exact data. In CDMFT errorbars are calculated by comparing two or more measurements of converged solutions only differing in the random number seed chosen and therefore the difference of each measurement in relation to the mean-value of all measurements can be seen as a statistical noise originating from the QMC approach which is only exact in the limit of infinite sampling numbers.

In figure 4.14 an example of an extrapolated self-energy for the first 40 Matsubara points is shown for an inverse temperature of $\beta t = 12.5$ and an interaction value of $U/t = 4$. Even though the onsite self-energy for the center site extracted by the extrapolation method signals a way different behavior for the first Matsubara frequency (left panel), the corresponding spectral function (right panel) differs not too much from the ones of the finite cluster sizes and is not in a completely different phase regime as it may be expected from comparing only the first Matsubara frequency. To understand why the huge effect of the extrapolated onsite self-energy does not lead to a significant difference in the spectral function part we have to remember that the spectral function is done by an analytical continuation of the local Green's function in Matsubara space. To get the local Green's function the inverse of the self-energy comes into play, connecting the onsite matrix elements of the local Green's function also to off-diagonal parts of the self-energy.

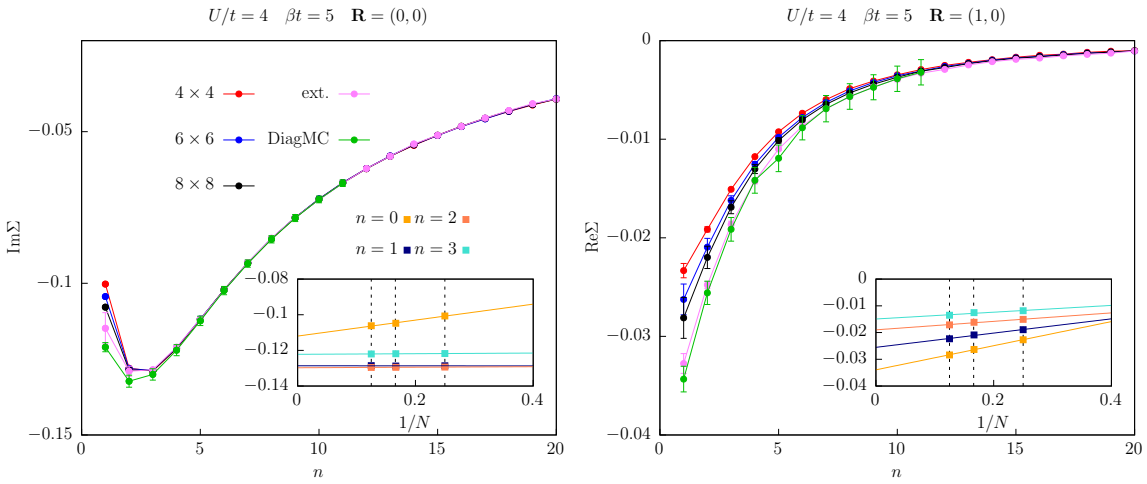

FIGURE 4.13.: Matsubara frequency dependence of the self-energy of the central site (left) at $R = (0,0)$ and of the neighboring one (right) at $R = (1,0)$. Besides the CDMFT calculation for cluster sizes $N \times N$ with $N = 4, 6, 8$ the extrapolated self-energy, as well as the self-energy calculated via the DiagMC method is shown. The inset in each panel shows the linear fit to obtain the extrapolated self-energy for the first four Matsubara frequencies.

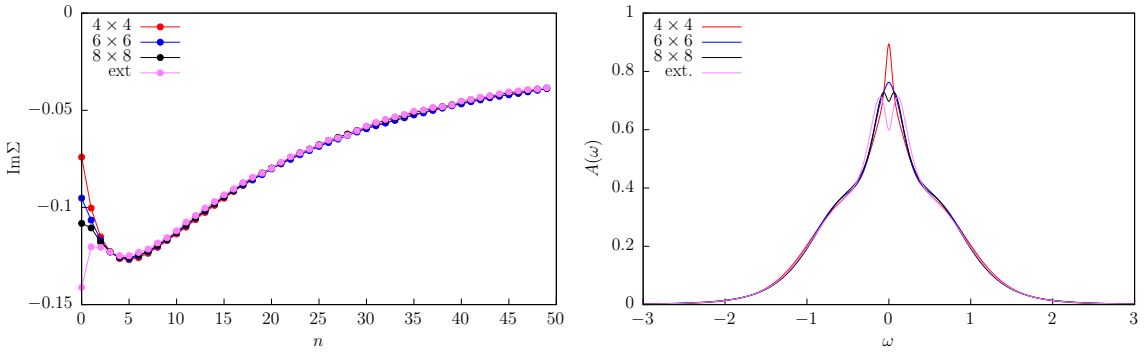

FIGURE 4.14.: Left: Onsite self-energy of the 4×4, 6×6, 8×8 and the extrapolated cluster for the center site, an inverse temperature of $\beta t = 12.5$ and an interaction of $U/t = 4$. A different behavior of the extrapolated self-energy for the first Matsubara frequency is clearly visible. Right: Onsite spectral functions for the center size of each cluster.

6. Center-focused extrapolation

In the previous section we discussed the extrapolation of the self-energy to infinite cluster sizes by using a linear fit in $1/N$ of our finite CDMFT calculations. In the following we combine this extrapolation with a center-focused method to gain better results of lattice properties using converged CDMFT solutions.

In section 4 we discussed the breaking of the translational invariance of the lattice by analyzing the local spectral function on the impurity. This leads to problems when performing a periodization scheme as it is described in section 2 since it is a method to restore the translational invariance by taking the mean-value over all sites inside the impurity. We now suggest a new method, by retaining the real-space dependence of the self-energy and focusing on the center site and the distances with respect to it to obtain the lattice self-energy

$$\Sigma(\mathrm{i}\omega_n, \mathbf{k}) = \sum_{i=0}^{N} \Sigma_{c,i}(\mathrm{i}\omega_n) \mathrm{e}^{-\mathrm{i}\mathbf{R}_i\mathbf{k}} \,. \tag{4.7}$$

Here the index c is labeling the center site and $\mathbf{R}_i$ is the real-space distance of impurity site

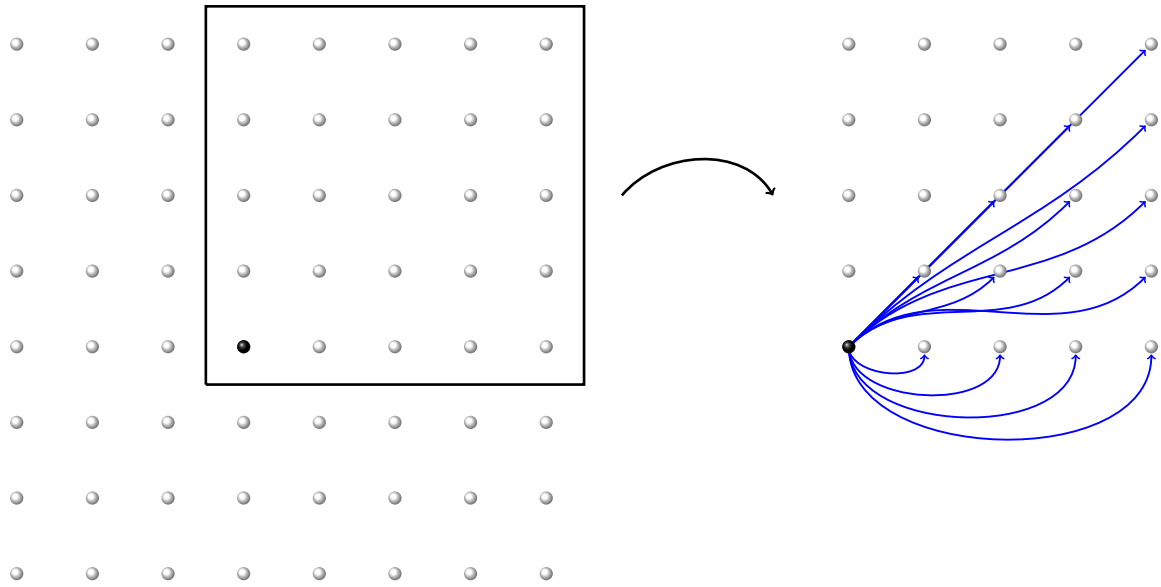

Figure 4.15.: Sketch for the center-focused method of the 8×8 cluster. The first step consists of dividing the whole cluster into a subpart where all topological invariant distances measured from the center site (color coded by black) are under consideration to extract the full momentum dependent self-energy according to equation (4.7).

i with respect to the center which can be always set to $\mathbf{R}_c = (0,0)$. We call the self-energy in equation (4.7) as the center-focused (cf) self-energy and note that (4.7) does not restore the translational invariance of the lattice but avoids taking into account the self-energy correlations between border sites of the impurity when creating a lattice property. By considering only the real-space distances measured from the center we get a maximum real-space correlation of

$$R_{\max} = \sqrt{(N/2)^2 + (N/2)^2} = \frac{N}{\sqrt{2}}$$

for the self-energy in the case of even N. The idea of the center-focused method is illustrated in figure 4.15 and consists of two major steps: First we only take into consideration distances of lattice sites with respect to the center with positive x and y values, which means we only cut out the top right part of the cluster (compare sketch in figure 4.15). Secondly we can create all real-space distances available in the cluster measured from the center by using the symmetry operations

$$x \to -x \qquad y \to -y \qquad x \to y\,. \tag{4.8}$$

By calculating CDMFT up to cluster sizes of 8×8 we can capture self-energy correlations with the center-focused method with a maximum real-space distance of $R_{\max} = \sqrt{32} \approx 5.65$.

To get to even better approximations of the lattice self-energy we can combine the before discussed method of extrapolating the self-energy to cluster sizes $N \times N = \infty \to \infty$ and the above mentioned center-focused method. The procedure of the so-called center-focused extrapolation (cfe) method is straight forward applicable to the cf-method, we simply exchange the impurity self-energy in equation (4.7) by the extrapolated one

$$\Sigma(\mathrm{i}\omega_n, \mathbf{k}) = \sum_{i=0}^{N} \Sigma_{c,i}^{\mathrm{ext}}(\mathrm{i}\omega_n)\mathrm{e}^{-\mathrm{i}\mathbf{R}_i\mathbf{k}}\,. \tag{4.9}$$

For interaction values of $U/t = 2,3,4$ the lattice self-energy on a given path of the first Brillouin zone obtained via cfe is shown in figure 4.16 for the inverse temperature of $\beta t = 5$.

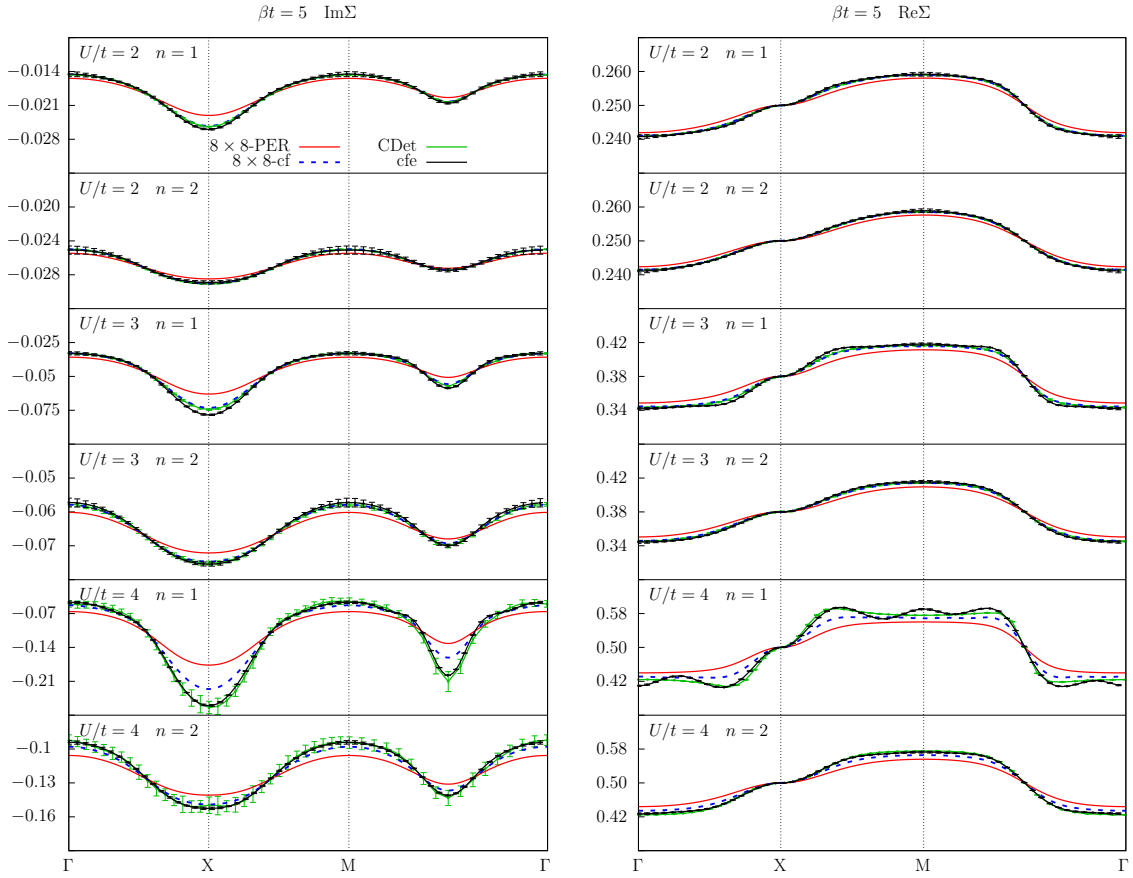

FIGURE 4.16.: Imaginary (left) and real (right) part of the momentum dependent lattice self-energy $\Sigma(k)$ at the first ($n = 0$) and second Matsubara frequency ($n = 1$) along a path in the first Brillouin zone, for an inverse temperature $\beta t = 5$ and different values of the interaction U/t. We plot the lattice self-energy obtained by conventional periodization of the 8×8 cluster self-energy (red), the cf-method for the 8×8 cluster (blue), the cfe method using an extrapolated 8×8 real-space self-energy (black), and the numerically exact DiagMC data (green).

Besides comparing the cfe method to a lattice self-energy obtained by a normal periodization procedure for 8×8 data (PER), we also show results of the cf method for the 8×8 cluster and exact numerical data obtained by DiagMC calculations [28]. First we note that the normal periodization of the self-energy even for a large CDMFT calculation with a size of 8×8 performs very poorly for every interaction value of U/t shown in figure 4.16. For the weak-coupling regime of $U/t = 2$ the difference between the normal cf and the cfe-method is very hard to observe, indicating that the extrapolated self-energy in real-space does not vary much compared to the local impurity self-energy of the CDMFT calculation. The extrapolated self-energy is equal to its largest counterpart used in the fit procedure when all cluster sizes used are already converged in terms of a decay of the self-energy which vanishes inside the cluster extension. In the case of $U/t = 3$ we see some deviation of the cfe method especially in the high-symmetry point $X = (0, \pi)$ and at $(\pi/2, \pi/2)$. It should be noted that in the case of $U/t = 3$ as well as $U/t = 2$ all results of the cfe and in fact also the cf method are within errorbars of the exact data obtained by DiagMC calculations. For the interaction of $U/t = 4$ we observe pronounced differences of all three methods shown in figure 4.16, where the difference in the imaginary part is most prominent once again at the high-symmetry points $X = (0, \pi)$ and $(\pi/2, \pi/2)$. We can hence conclude that the center-focused extrapolation should be the way to go in order to

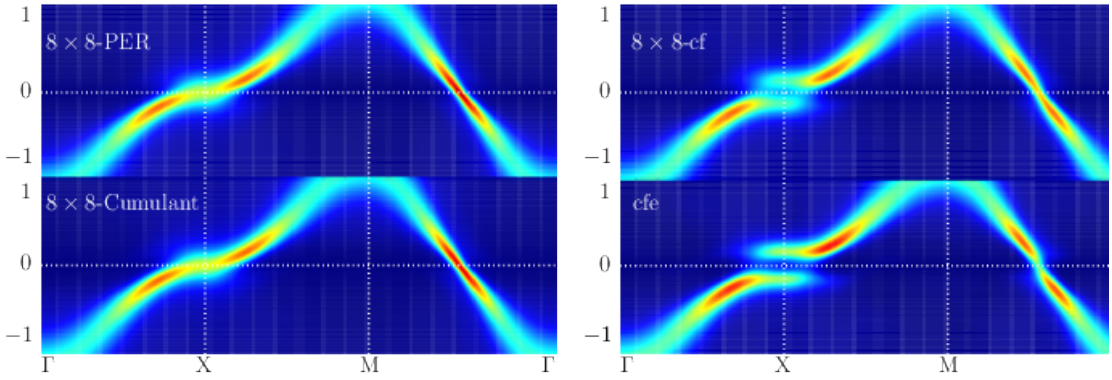

Figure 4.17.: Spectral function of the lattice Green's function along a closed path in the first Brillouin zone obtained with the normal periodization method of the self-energy (top left panel), the cumulant (lower left panel), the center-focused method, all for the 8×8 self-energy (upper right panel) and the lattice Green's function obtained by the center-focused extrapolation (lower right panel). For all shown results the inverse temperature is $\beta t = 5$ and the interaction $U/t = 4$.

produce lattice self-energies from converged CDMFT solutions. Since DiagMC is not able to produce reliable results for lower temperatures figure 4.16 contains the best possible comparison between our newly established method and available exact numerical data.

Another way to illustrate how impacting the cfe-method is compared to other periodization methods is to take the momentum dependent self-energy $\Sigma(\mathrm{i}\omega_n, \mathbf{k})$ defined in equation (4.9) and create a lattice Green's function $G(\mathrm{i}\omega_n, \mathbf{k})$ according to equation (4.2). Figure 4.17 contains the spectral function covering a closed path of the first Brillouin zone for four different lattice Green's functions at an inverse temperature of $\beta t = 5$ and an interaction $U/t = 4$. Every lattice Green's function differs in the way the momentum dependent self-energy is produced, where the first column contains the normal periodization (upper panel) of the self-energy and the cumulant periodization (lower panel), whereas the second column the lattice Green's function obtained for the center-focused self-energies for the 8×8 (upper panel) and the extrapolated case (lower panel). The difference of the momentum dependent self-energy is most visible on the high-symmetry point $X = (\pi, 0)$ and the point $(\pi/2, \pi/2)$. At X the normal periodization of the self-energy and the cumulant show spectral weight at the Fermi surface while the center-focused methods are already in a gaped state. The 8×8 center-focused method shows a pseudogap phase, whereas the corresponding calculation with the extrapolated self-energy shows a small gap opening at the point $(\pi/2, \pi/2)$.

7. Decay of the self-energy

In the last section we applied the center-focused extrapolation method to access lattice self-energies which are within errorbars of numerically exact DiagMC data (compare figure 4.16). As stated the comparison is restricted to the inverse temperature of $\beta t = 5$ which makes it unable to answer the question of how well the cfe-method compares to DiagMC in lower temperature regimes. Nevertheless we can estimate how good the cfe approach should perform by looking at the real-space decay of the extrapolated self-energy. Taking the insight of former discussions we know that the first Matsubara frequency should tell us if the self-energy drops

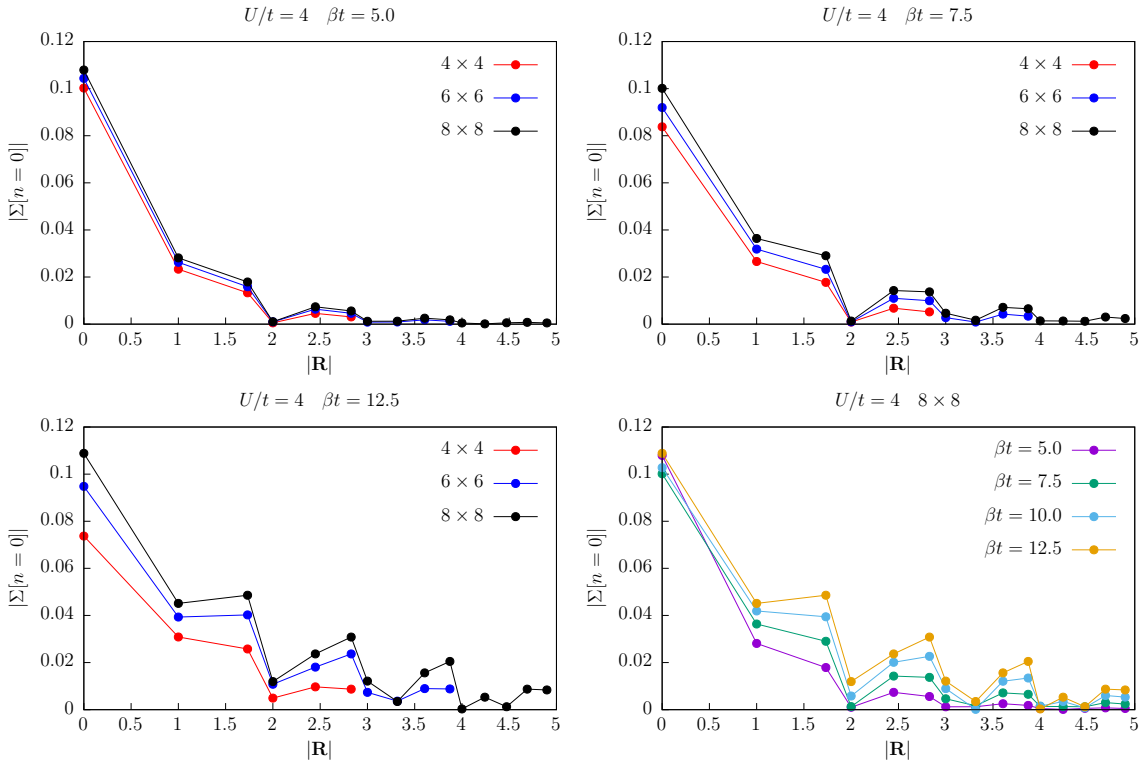

Figure 4.18.: Absolute value for the first Matsubara frequency of the real-space self-energy correlations for the different cluster sizes $N \times N$ with $N = 4, 6, 8$. Besides three different inverse temperatures of $\beta t = 5, 7.5, 12.5$ a temperature dependent self-energy decay for the 8×8 cluster is shown in the lower right panel. The self-energy decay of the upper left panel is used to produce the results shown in the lower two panels of figure 4.16. For the lowest temperature $\beta t = 12.5$ the cluster of size 8×8 is visibly not decayed within the cluster.

down to zero inside the impurity cluster. Results of the self-energy decay for different inverse temperatures and interaction values are shown in figure 4.18. The upper left panel corresponds to the ones used to perform the cfe method in the lower two panels of figure 4.16, where we observe an agreement of the cfe-method with the DiagMC data within errorbars. Going back to the decay we see that the self-energy for the cluster size of 8×8 goes to zero inside the cluster. Reminding that for the longest real-space distances of the size 8×8 it is not possible to perform an extrapolation since there is only one data point available, the extrapolated self-energy is in fact estimated in this regime by the pure 8×8 data. By performing a Fourier transformation of the extrapolated self-energy we also take into account long-range modes corresponding to the pure 8×8 data, which should lead to problems for the momentum dependent cfe self-energy if those long-range modes are not decayed in the 8×8 cluster. We can check this statement by considering the same closed path inside the first Brillouin zone as in figure 4.16 for the parameter set of $\beta t = 12.5, U/t = 6$, for which the self-energy decay is represented in the lower left panel of figure 4.18 and is visibly not decayed. For the first two Matsubara frequencies the momentum dependent self-energy using the cfe-method is show in figure 4.19. By comparing the normal periodization of the self-energy (red curve) with the ones obtained by the cf-methods using the pure 8×8 self-energy (blue) and the extrapolated self-energy (black) we see a clear deviation of the two techniques. Comparing the cfe method with the normal periodization and the lower panel of figure 4.16 we observe many oscillations. These oscillations stem from the fact that real-space modes are missing when performing the Fourier transformation. These

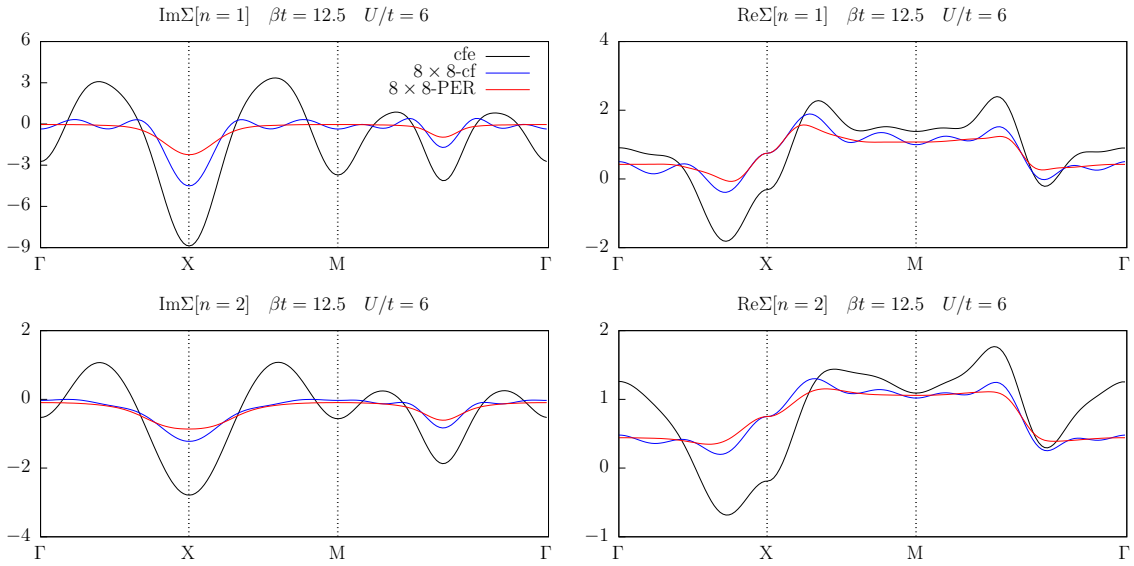

FIGURE 4.19.: Imaginary (left) and real (right) part of the momentum dependent lattice self-energy $\Sigma(k)$ at the first ($n = 0$) and second Matsubara frequency ($n = 1$) along a path in the first Brillouin zone, for an inverse temperature $\beta t = 12.5$ and $U/t = 6.0$. Besides the periodization of the 8×8 cluster self-energy (red), the cf-method of the 8×8 self-energy cluster (blue) and the extrapolated self-energy (black) are shown. For the central-focused lines we observe more oscillation compared to the self-energy of the standard periodization method, indicating missing modes in the Fourier transformation of the cf-method.

missing modes would become available if we are able to increase the cluster size until the self-energy decays to zero inside the local impurity. We can assume that for intermediate to strong coupling regimes $U/t > 4$ and low temperature calculations $\beta t > 15$ the CDMFT extrapolated self-energies for cluster sizes up to 8×8 are not sufficient to create a momentum dependent self-energy using the cfe-method which would be inside errorbars of exact numerical DiagMC data.

8. Two-particle quantities

In the last sections we mainly discussed the one-particle self-energy, be it local or the transformation to a lattice object, in the CDMFT approach. We now move to two-particle quantities and in particular two-particle properties which are local in terms of the impurity. Generally a two-particle Green's function is defined as

$$\chi^{\sigma_1,\sigma_2,\sigma_3,\sigma_4}_{i,j,k,\ell}(\tau) = \left\langle c^\dagger_{i,\sigma_1}(0) c_{j,\sigma_2}(0) c^\dagger_{k,\sigma_3}(\tau) c_{\ell,\sigma_4}(\tau) \right\rangle \ . \tag{4.10}$$

Differently to the one-particle quantities we cannot formulate a self-consistent equation for the quantity (4.10) in a DMFT respective CDMFT approach

$$\chi_{\text{imp}}(\mathrm{i}\omega_n) \neq \chi_{\text{loc.}}(\mathrm{i}\omega_n) = \sum_{\mathbf{q}\in BZ} \chi(\mathrm{i}\omega_n, \mathbf{q}) \ . \tag{4.11}$$

First we mention that the two-particle Green's function (4.10) is a bosonic object and therefore the first Matsubara frequency is in fact $\mathrm{i}\omega_n = 0$ for the index $n = 0$. Even though the inequality of equation 4.11 holds true for CDMFT calculations on a finite cluster, for clusters of infinite

size we reproduce the whole lattice problem and the left and the right side of equation (4.11) are equal. We here focus on two correlation functions, namely the spin-spin susceptibility

$$\chi^S(\tau, \mathbf{R}_i - \mathbf{R}_j) = \left\langle [n_{i,\uparrow}(0) - n_{i,\downarrow}(0)][n_{j,\uparrow}(\tau) - n_{j,\downarrow}(\tau)] \right\rangle \tag{4.12}$$

and the charge-charge susceptibility defined on the impurity as

$$\chi^C(\tau, \mathbf{R}_i - \mathbf{R}_j) = \left\langle [n_{i,\uparrow}(0) + n_{i,\downarrow}(0)][n_{j,\uparrow}(\tau) + n_{j,\downarrow}(\tau)] \right\rangle \ . \tag{4.13}$$

To capture only the dynamical part of the charge-charge susceptibility it is convenient to correct the correlation by the equal-time term, i.e.

$$\begin{aligned} \chi^C(\tau, \mathbf{R}_i - \mathbf{R}_j) = &\left\langle [n_{i,\uparrow}(0) + n_{i,\downarrow}(0)][n_{j,\uparrow}(\tau) + n_{j,\downarrow}(\tau)] \right\rangle \\ &- \left\langle n_{i,\uparrow} \right\rangle \left\langle n_{j,\uparrow} \right\rangle - \left\langle n_{i,\uparrow} \right\rangle \left\langle n_{j,\downarrow} \right\rangle - \left\langle n_{i,\downarrow} \right\rangle \left\langle n_{j,\uparrow} \right\rangle - \left\langle n_{i,\downarrow} \right\rangle \left\langle n_{j,\downarrow} \right\rangle \ , \end{aligned} \tag{4.14}$$

which will lead to the correction of 1 in the case of half filling. For the correlation function in frequency space this will lead to a correction of β for the $\Omega_n = 0$ Matsubara frequency.

By performing two-particle measurements of the type (4.12) and (4.13) on converged 8×8 CDMFT solutions, we are able to capture a wide real-space range of correlations on the cluster impurity. All measures of the correlation functions (4.12) and (4.13) are performed in the imaginary time framework. Since it is very numerically challenging to calculate one τ point for two-particle correlation functions, the amount of total time steps in $\tau \in [0, \beta]$ is kept to an absolute minimum, leading to a poor resolution in the Matsubara space after doing a Fourier transformation. In the following we discuss the dynamics of the two-particle objects in the imaginary time space and restrict discussions of results in the frequency space to the zero frequency $n = 0$ which is very stable against low τ resolution. This statement was checked by slowly increasing the total imaginary time points τ_p from 2 up to 200 for some example calculations, where a convergence of the zero Matsubara frequency is found for $\tau_p = 36$, leading to a total resolution of 11 frequency points in Matsubara space.

8.1. Compressibility

In the following we show that the compressibility of the system can be extracted from the charge-charge correlation function is connected to the compressibility of the system.

The compressibility κ of a system is defined by using the charge-charge correlator

$$\kappa = \frac{1}{N} \sum_{i,j} \chi^C(\Omega_n = 0, \mathbf{R}_i - \mathbf{R}_j) \ , \tag{4.15}$$

where N is the total number of impurity sites. The compressibility calculated in (4.15) is also connected to one-particle properties [58] via the variation of the density induced by varying the chemical potential

$$\kappa = \frac{\mathrm{d}n}{\mathrm{d}\mu} = \frac{1}{N} \sum_{i,j} \chi^C(\Omega_n = 0, \mathbf{R}_i - \mathbf{R}_j) \ . \tag{4.16}$$

Analogously to the single-particle quantities, we adapt the calculation of the compressibility in (4.15) to include only the center site

$$\kappa = \sum_{i} \chi^C(\Omega_n = 0, \mathbf{R}_{cs} - \mathbf{R}_i) \ , \tag{4.17}$$

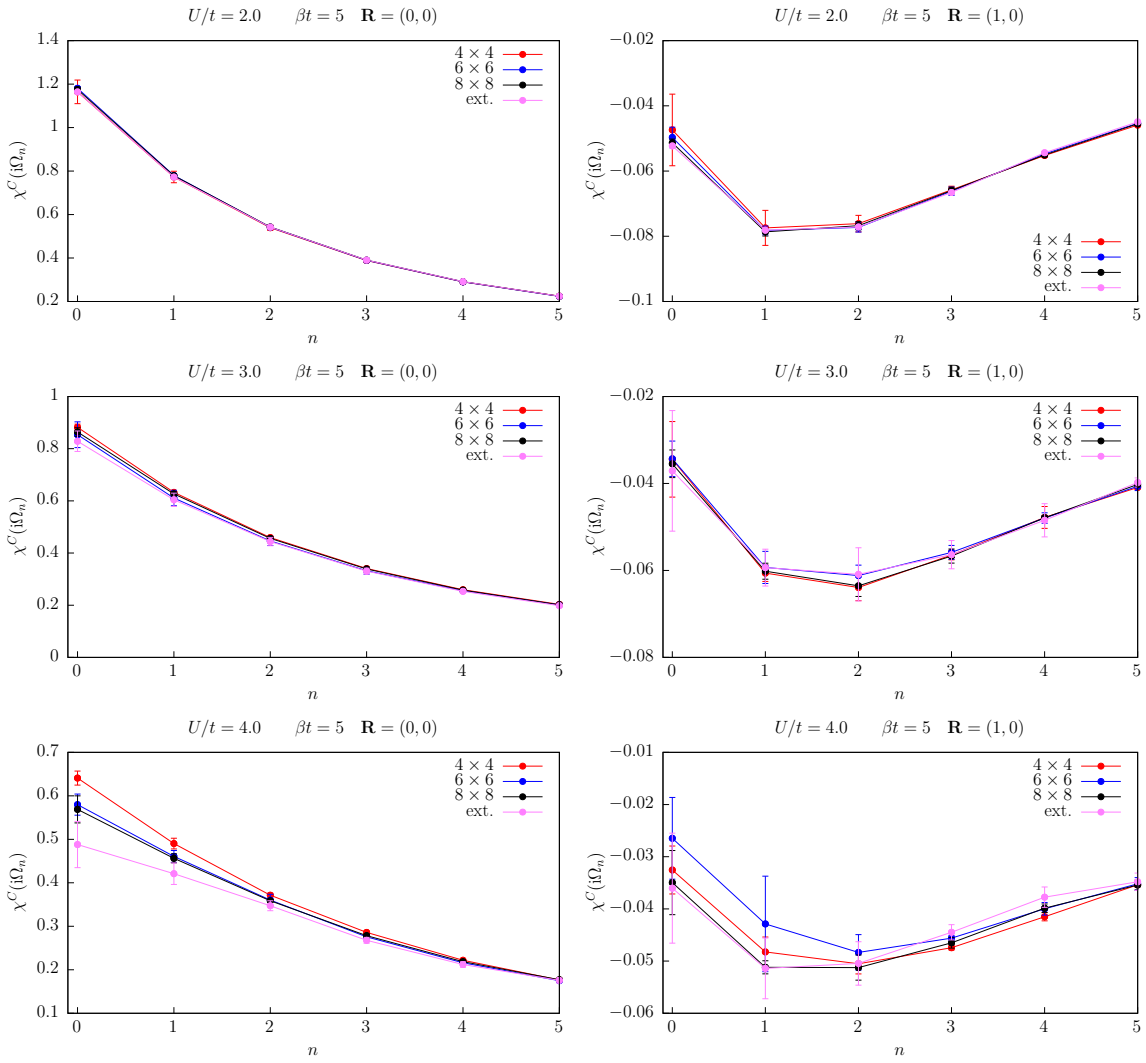

Figure 4.20.: Onsite (left panel) and nearest neighbor (right panel) charge-charge susceptibility of the first 6 Matsubara frequencies for the three different interactions $U/t = 2, 3, 4$ and an inverse temperature of $\beta t = 5$.

in order to avoid unwanted rim effects of the impurity. Before discussing further details of the compressibility we show raw data of the charge-charge two-particle correlation function for the local center and the non-local nearest neighbor correlation in figure 4.20. Results of the compressibility can be found in figure 4.21, where we present results of the center site compressibility for interaction values of $U/t = 2, 3, 4$ using equation (4.17) together with the one-particle calculation (4.16). The derivative of the density with respect to the chemical potential is also evaluated for the largest cluster (orange solid lines) and only for the center-site (orange dashed lines) in figure 4.21. For the computation of the derivative, we consider three densities for the chemical potential of $\mu = U/2 - 0.05, U/2, U/2 + 0.05$ (we note that the densitiy for the chemical potential $n(U/2) = 1$ is already known). Fitting a linear function to the three data points makes it easy to extract the derivative. First we indeed notice a good agreement between the two possible methods to calculate the compressibility for the example calculation of $U/t = 2$ and the 8×8 cluster. Besides the results for cluster sizes of 4×4 (red), 6×6 (blue) and 8×8 (black) the extrapolated (orchid) results for κ are shown. To interpret the extrapolated results it is important to notice that the direct results for κ are used for the extrapolation, rather

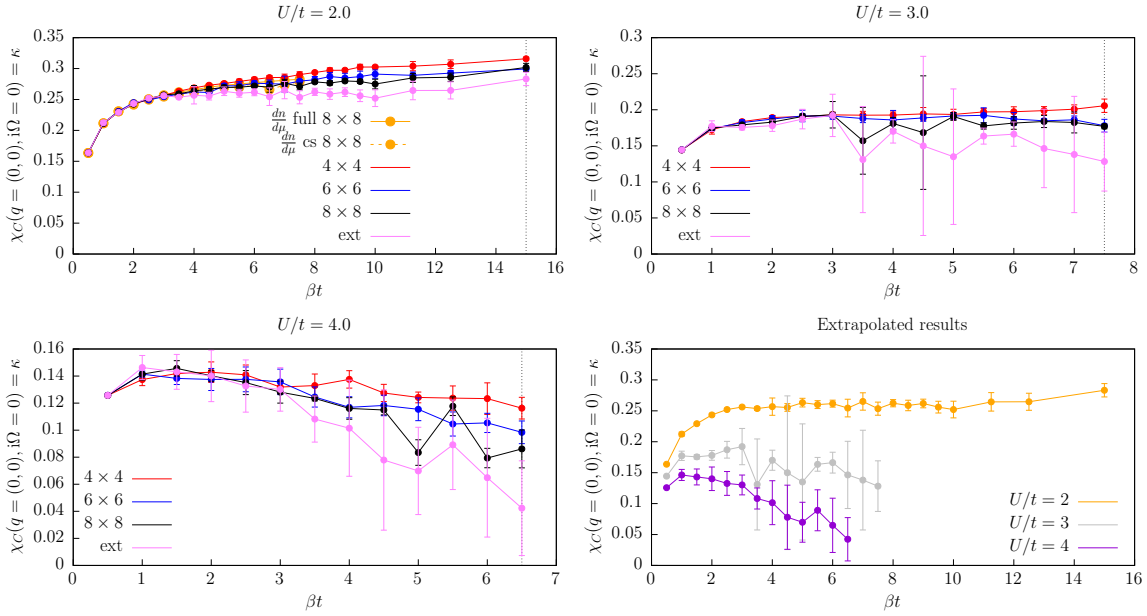

FIGURE 4.21.: Compressibility for the interaction values of $U/t = 2, 3, 4$ plotted over different inverse temperatures βt. Besides the results of the 4×4 (red), 6×6 (blue) and 8×8 (black) cluster, the extrapolated (orchid) compressibility is also shown. In the lower right panel the extrapolated results for different interaction values are shown together in one plot.

than the extrapolation of every single real-space two-particle correlation $\chi_C(\Omega_n = 0, \boldsymbol{R})$. Since the absolute values of the compressibility are of the order 10^{-2} and the statistical noise of the order of 10^{-3}, error bars of almost 10% on the real-space two-particle correlation function $\chi_C(\Omega_n = 0, \boldsymbol{R})$ appear in figure 4.21. Taking a look at the extrapolated results for the interaction values of $U/t = 2, 3, 4$ in the lower right panel of figure 4.21 we can observe a maximum of the compressibility for $U/t = 3$ and $\beta t = 3$, as well as $U/t = 4$ and $\beta t = 2$. The large errorbars and the small temperature resolution makes it hard to accurately determine the maximum of the extrapolated results. All calculations shown are produced in the paramagnetically forced framework, where the anti-ferromagnetic transition line of the 8×8 cluster is indicated by a vertical dashed line. For smaller cluster sizes we know from former single-particle results that the transition line for the magnetic ordering is found at higher temperatures (compare section 3, which means that all clusters are in the ordered phase while crossing the dashed line. In general the compressibility has to vanish in the vicinity of the Mott metal-to-insulator transition since changing the chemical potential inside the bandgap does not affect the density. We note that the insulating state for larger cluster is reached at higher temperatures and therefore a dip in the compressibility can be interpreted as approaching the transition point. In consideration of the visible differences between the cluster sizes we investigate the role of the non-local two-particle correlations by dividing the total compressibility into two terms

$$\kappa = C_{\text{loc}} + C_{\text{Nloc}} = \chi^C(\Omega_n = 0, \mathbf{R}_{cs} - \mathbf{R}_{cs}) + \sum_{i \neq cs} \chi^C(\Omega_n = 0, \mathbf{R}_{cs} - \mathbf{R}_i) \; . \tag{4.18}$$

For different interaction values U/t the local and non-local parts of the compressibility are shown as a function of temperature in figure 4.22. The first observation is a different sign for the magnitude of local (negative) and non-local (positive) contributions where the absolute values get larger for the local as well as the non-local parts while lowering the temperature. Even though we only calculated very few data points along the interaction axis U, we are able

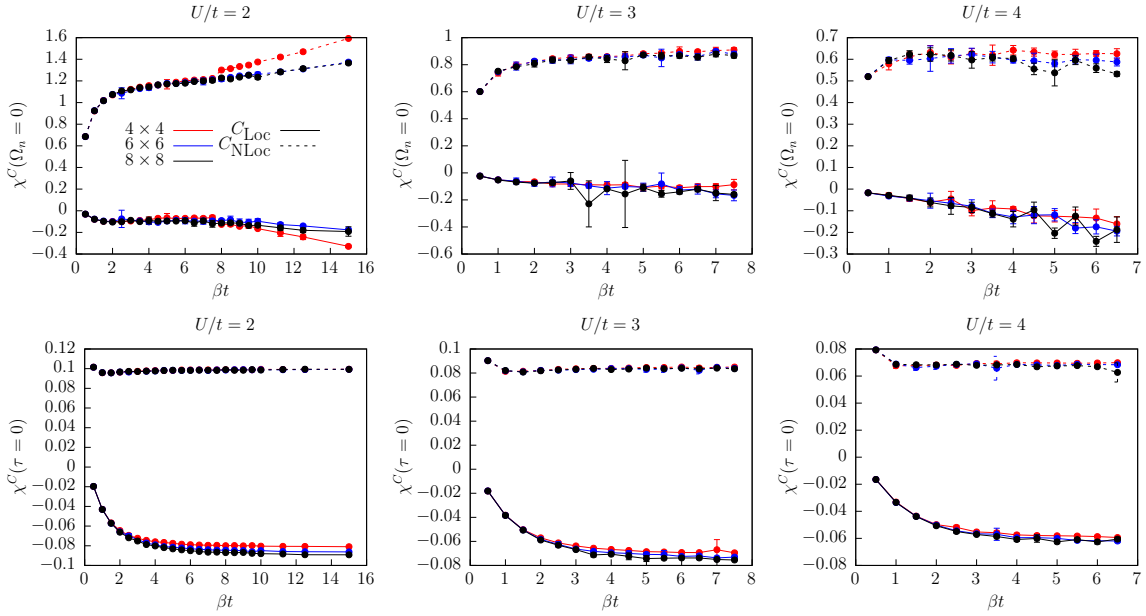

FIGURE 4.22.: Local and non-local part of the static and equal time charge-charge correlation for three different interaction values of $U/t = 2, 3, 4$ plotted over the inverse temperature βt.

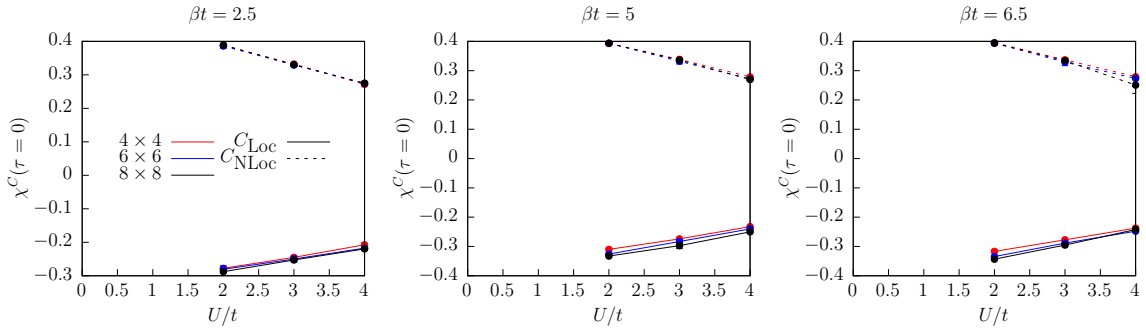

FIGURE 4.23.: Local and non-local part of the equal time charge-charge correlations in dependence of the interaction for three different constant inverse temperatures βt.

to also take a look at the local and non-local behavior of the charge-charge correlations as a function of the interaction (at constant temperatures). These results are shown in figure 4.23 where we detect a reduction with increasing interaction. This is in agreement with the behavior of the compressibility discussed above, which is the sum of local and non-local part and should vanish while entering the Mott metal-to-insulator regime.

8.2. Spin susceptibility

We start by showing data for the onsite and nearest-neighbor spin-spin correlation function for the first 6 Matsubara frequencies in figure 4.24 Besides the compressibility κ defined via the two-particle charge-charge correlation, we analogously define the uniform spin susceptibility via

$$\chi^S_{\mathrm{uni}} = \chi^S(\boldsymbol{q} = 0, \Omega_n = 0) \equiv \zeta = \sum_i \chi^S(\Omega_n = 0, \mathbf{R}_{cs} - \mathbf{R}_i) \,. \tag{4.19}$$

Results of the uniform spin susceptibility for three different interactions $U/t = 2, 3, 4$ are shown in figure 4.25. At high temperatures the uniform susceptibility ζ has to follow the $1/T$ Curie's

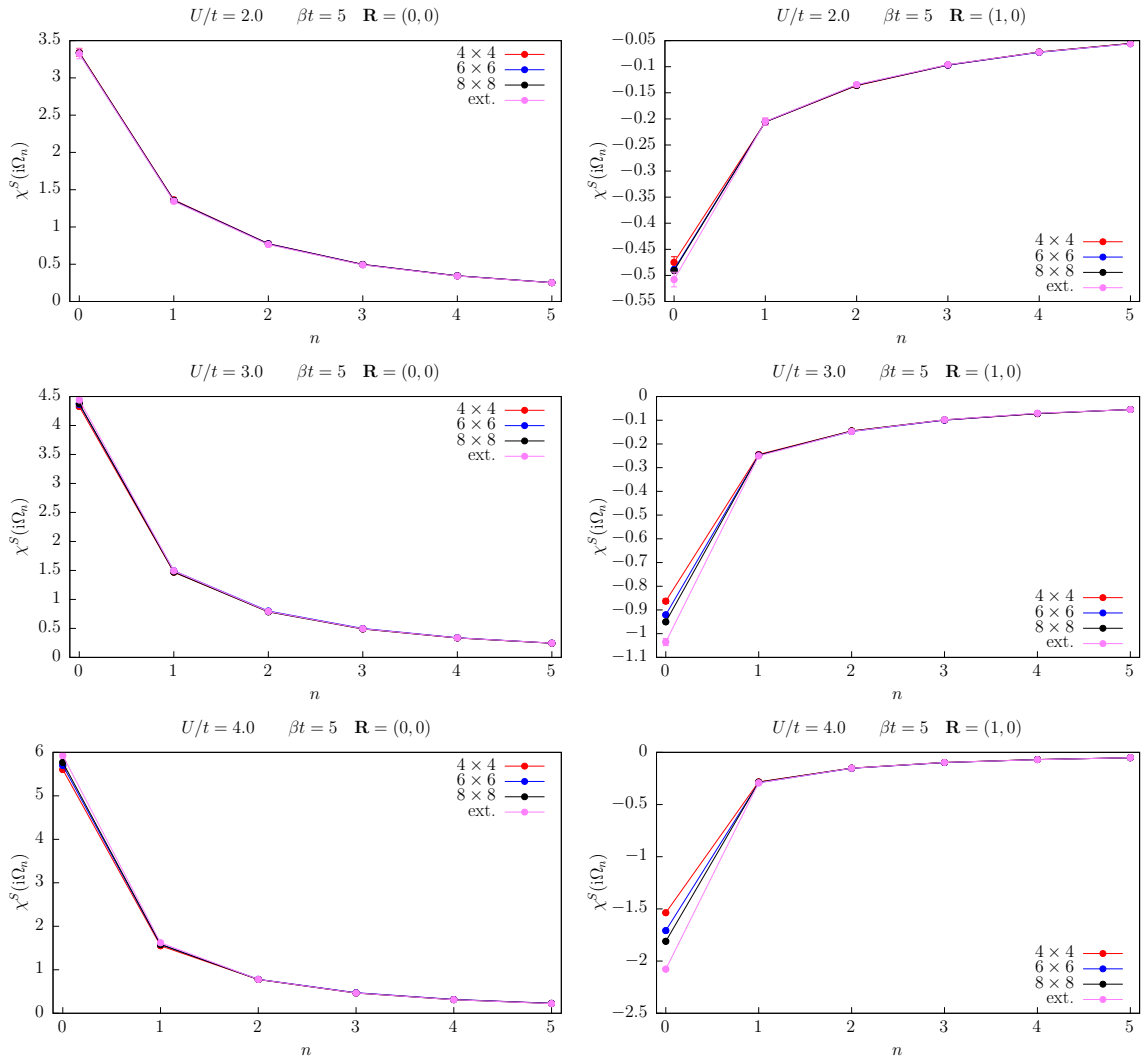

Figure 4.24.: Onsite (left panel) and nearest neighbor (right panel) spin-spin susceptibility of the first 6 Matsubara frequencies for the three different interactions $U/t = 2, 3, 4$ and an inverse temperature of $\beta t = 5$.

law. Going to lower temperatures we again see a clear cluster-size dependence. We note that all calculations are done in the paramagnetically forced framework and the Nèel transition line of the 8×8 cluster is indicated as a dashed vertical line. For the largest interaction of $U/t = 4$ shown in figure 4.25 the extrapolated results exhibit a distinct maximum for the uniform spin susceptibility ζ at roughly $T/t = 0.25$ which is in a temperature regime way above the phase transition and can therefore be accessed without problems using the extrapolation method. The clear deviation from the $1/T$ Curie law can be interpreted as strong non-local magnetic fluctuations inside the cluster. While finding a visible maximum at $U/t = 4$, the weak coupling regime $U/t = 2$ only shows a Curie behavior over the whole temperature regime and for all cluster. In the intermediate regime of $U/t = 3$ it seems that the different cluster sizes are still following a $1/T$ behavior even at low temperatures, but the extrapolated results clearly deviate from it, even though its relatively hard to find a distinct maximum in the extrapolated uniform spin susceptibility.

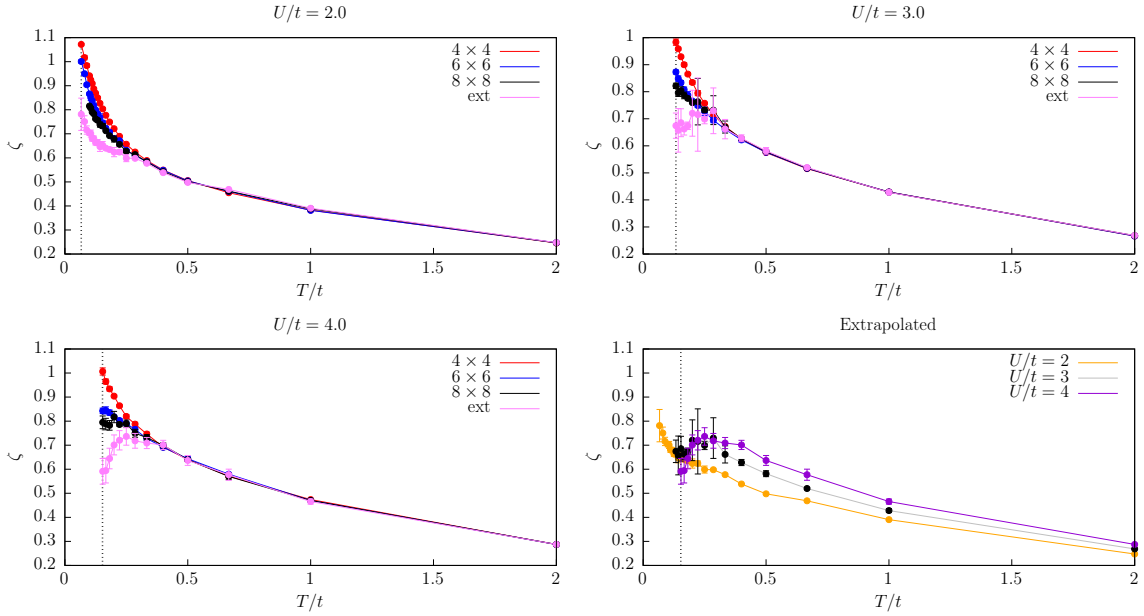

Figure 4.25.: Uniform spin susceptibility for the interaction value of $U/t = 2, 3, 4$ plotted over different temperatures T/t.

8.3. Correlation length and real-space decay

In the following we investigate the real-space decay of the self-energy, the charge-charge correlation and the spin-spin susceptibility. A simple visualization is obtained by using a colorplot as shown in figure 4.26 For the interaction of $U/t = 4$ the inverse temperature $\beta t = 6.5$ correspons to the anti-ferromagnetic transition temperature in the 8×8 case and we expect the self-energy to show the largest real-space expansion inside the paramagnetic phase. Taking a look at the last row of figure 4.26 which represents the real-space decay of the 8×8 cluster, we can clearly see that the self-energy is decayed inside the cluster. For the charge-charge correlation it seems that only the two nearest neighbors are actually important, while the correlation between the center and all other sites is basically zero. The colorplot clearly reveals that the spin-spin correlation has the longest correlation length. Investigating the spatial real-space dependence of the self-energy and the spin-spin susceptibility we identify a radial decay in the latter, while the former shows a non-zero value on the diagonal axis while the correlation along the axis decays much faster.

The uniform real-space decay behavior of the spin-spin correlation allows to extract the correlation length χ with the help of the Ornstein-Zernike formula [59], which reads in real-space

$$\chi^S(R) = A\frac{\xi}{R}\mathrm{e}^{-\frac{R}{\xi}}\,, \tag{4.20}$$

where A and the correlation length ξ are fit parameters. The extracted correlation length ξ is shown in figure 4.27. Besides the cluster sizes of 4×4 (red), 6×6 (blue) and 8×8 (black) the extrapolated (orchid) correlation length is shown. For all values of the interaction, one can clearly note a difference of the correlation length while varying the cluster size, especially going to lower temperatures. In all cases the extrapolated quantity shows the largest correlation length, reaching values greater than the 8×8 cluster at the Nèel transition temperature for $U/t = 4$. Calculating correlation lengths only in the paramagnetic regime does not lead to

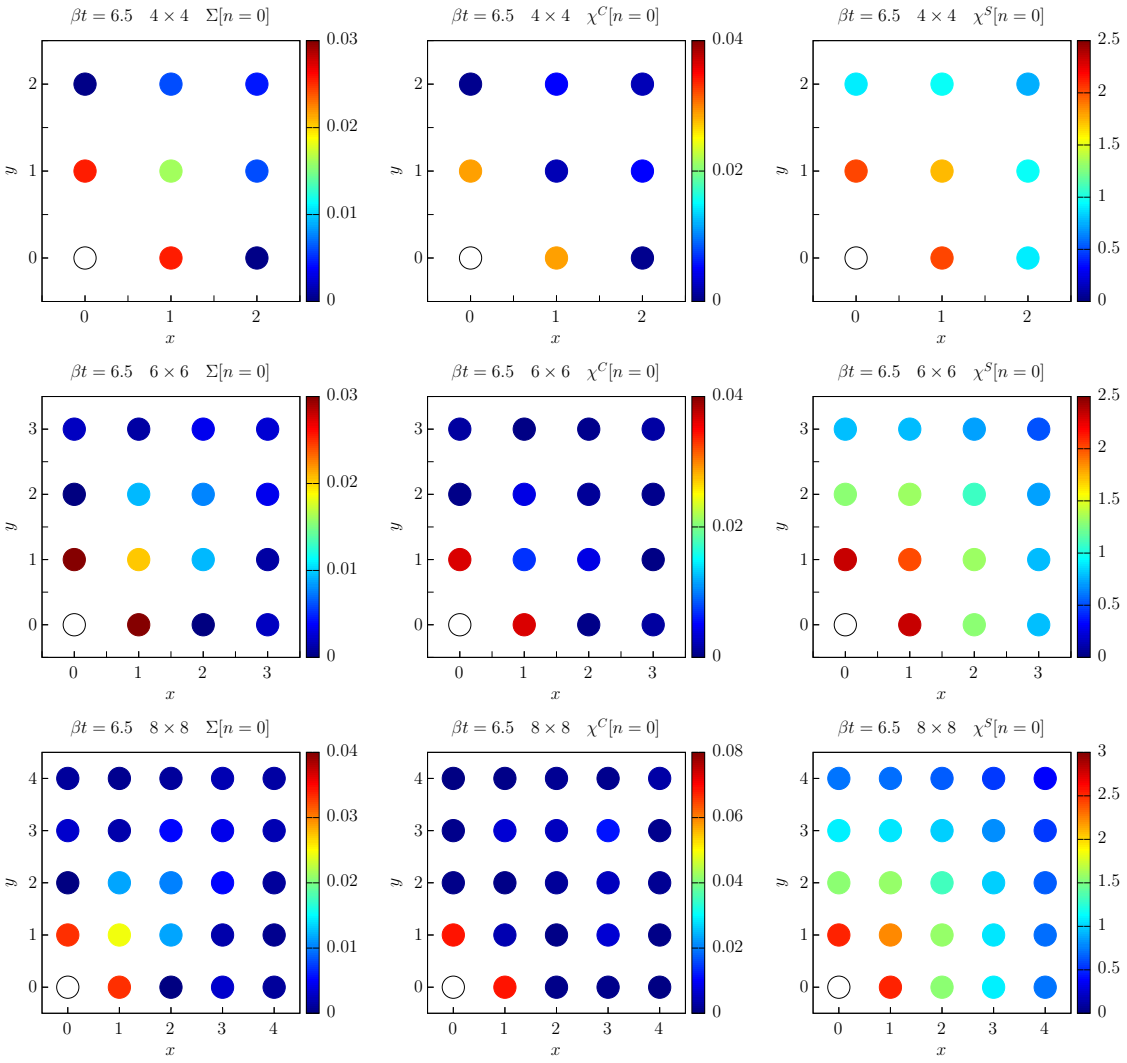

Figure 4.26.: Real-space decay for the self-energy (first column), the charge-charge correlation (second column) and the spin-spin correlation (third column) using an interaction of $U/t = 4$ for cluster sizes of 4×4 (first row), 6×6 (second row) and 8×8 (third row). Due to visualization reasons the onsite site is set to zero in order to not influence the color scale.

correlation lengths exceeding the length of the actual cluster. For the interaction of $U/t = 4$ the extrapolated correlation length clearly shows an exponential behavior which is best shown as linear function for lower temperatures using a logscale (right panel in figure 4.27). For $U/t = 2$ the correlation length seems to converge to a constant while lowering the temperature. This odd behavior of the weak coupling regime can be explained by the following observation: The spin-spin suscpetibility is already close to zero for distances larger than the nearest neighbor making it difficult to use the Ornstein-Zernike fit function in real-space. In particular, the latter is only valid for real-space distances $R \to \infty$.

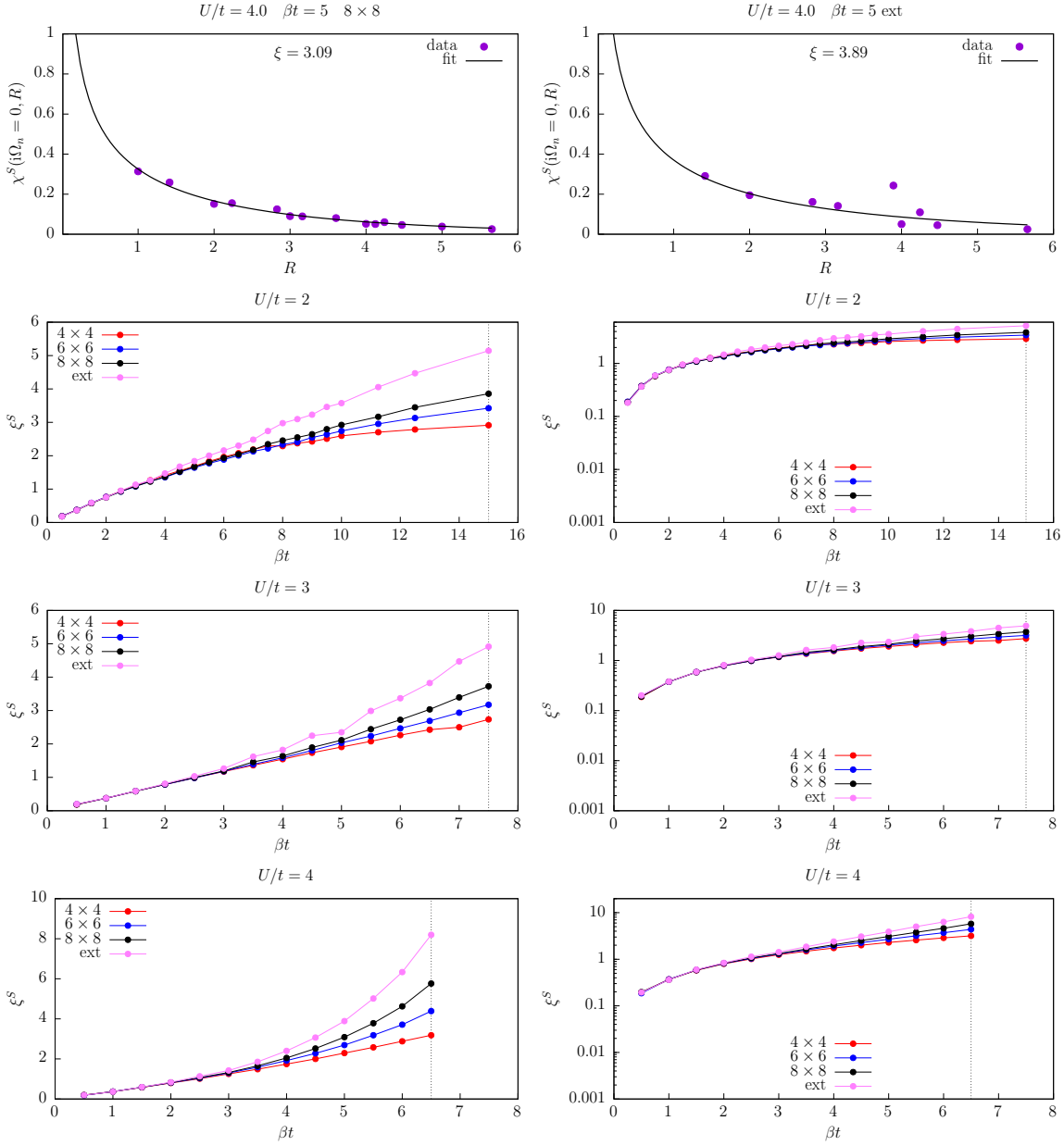

Figure 4.27.: Top column: Example procedure of extracting the correlation length using normalized real-space spin-spin correlations for a cluster size of 8×8 (left) and the extrapolated susceptibility (right) and the parameters $U/t = 4, \beta t = 5$. The other rows show the correlation length for the interactions of $U/t = 2, 3, 4$ for a linear y-axis (left panels) and a logscale version (right panels). The anti-ferromagnetic transition line is always indicated as a vertical dashed line.

V. The Triangular Lattice: A CDMFT approach

In this chapter we investigate the Hubbard model on a two-dimensional triangular lattice. Besides discussing DMFT results we calculate results for an impurity including $N = 7$ sites.

1. The Triangular Lattice

This section will shortly review the model in use in this part of this work. Like before we take the Hubbard model in two dimensions as the model of choice, but this time on a triangular lattice instead of a square lattice. A schematic scheme of the triangular lattice and the unit cells including one site (red) and 7 sites (blue) are shown in figure 5.1. Unlike before we introduce a frustration of t_p. The system shown in figure 5.1 is called geometrically frustrated, since there is no magnetization of the spin 1/2 particles on a triangular lattice such that the total spin vanishes. This leads to a large variety of interesting questions of this lattice geometry. Besides the investigation of finding a Mott metal-to-insulator transition in the triangular lattice forced in the paramagnetic case (every site has a total magnetization of $m_i = 0$), the question arises if this transition survives in the magnetically ordered phase.

The dispersion relation of the red triangular lattice unit cell in figure 5.1 including a frustration of t_p reads

$$\varepsilon(\mathbf{k}) = -2t_p \cos(k_x) - 2t \left[\cos\left(\frac{k_x}{2} + \frac{\sqrt{3}}{2} k_y \right) + \cos\left(\frac{k_x}{2} - \frac{\sqrt{3}}{2} k_y \right) \right] . \tag{5.1}$$

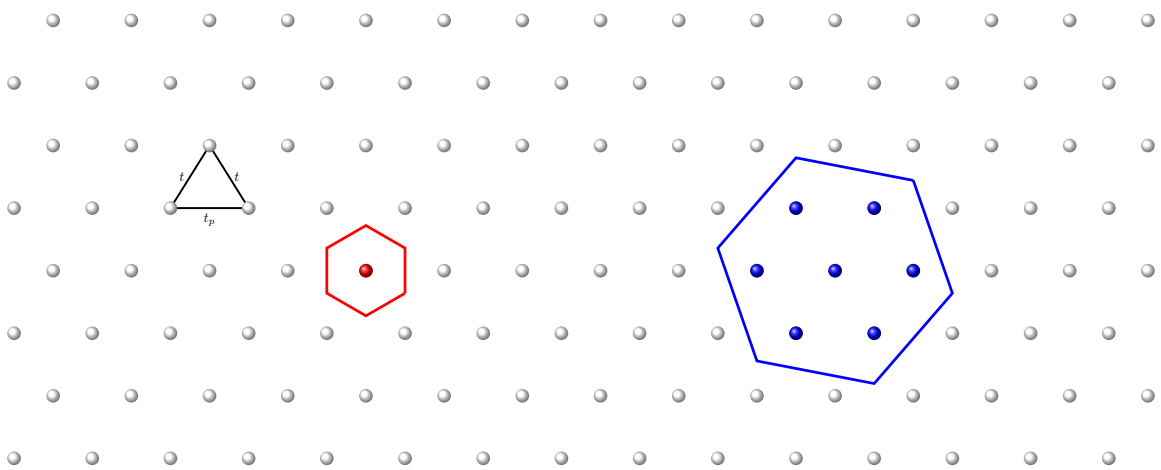

FIGURE 5.1.: Sketch of the triangular lattice in two dimensions. All lattice sites are indicated by points. The red area represents the Wigner-Seitz cell of the single-site unit cell, whereas the seven-site unit cell is shown in blue.

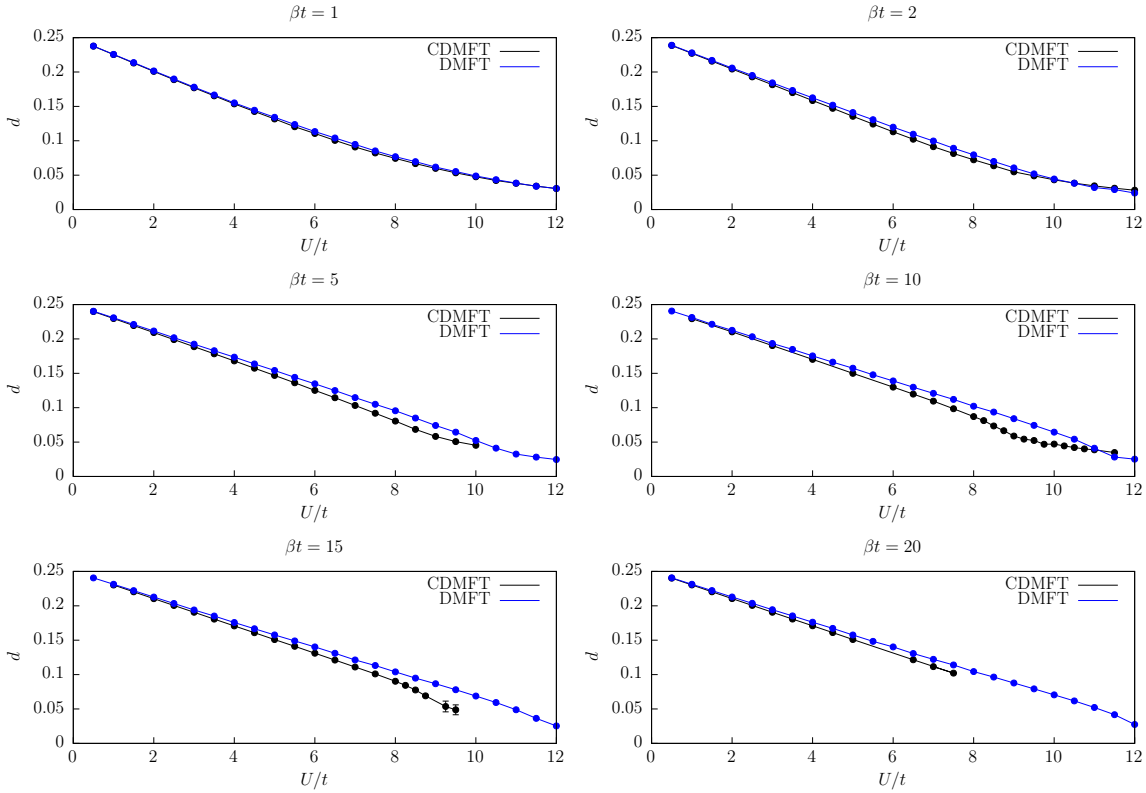

Figure 5.2.: Double occupancy for the single site calculation (blue) and the center site for the seven-site cluster (black) for different temperatures.

2. Results

In this part we discuss the results of the triangular lattice as obtained by CDMFT for an impurity including 7 sites (compare figure 5.1).

The first physical observable we investigate is the double occupancy of the center site

$$d = \left\langle n_{c,\uparrow} n_{c,\downarrow} \right\rangle \ , \tag{5.2}$$

which has 6 local neighbors in the 7-site cluster. The double occupancy d can be seen as a measure of the insulating behavior for the system. For the case of $U = 0$ the double occupancy is $d = 0.25$ and for large values of U we find an insulating state with no double occupancy $d \to 0$. Results for the double occupancy of the DMFT and CDMFT approach are shown in figure 5.2. Even though we are only able to calculate a 7-site cluster, i.e. the center site and one surrounding shell, the differences between DMFT and CDMFT results are clearly visible for low temperatures. The CDMFT presents lower values of the double occupancy, leading to a Mott metal-to-insulator transition at lower U values compared to the DMFT results, similiary to the findings for the square lattic. In addition to the double occupancy as an indicator for the Mott metal-to-insulator transition, also the value of the quasi-particle weight Z introduced in equation (3.7) is of the interest. We show Z for different temperatures in figure 5.3. For the case of $\beta t = 10$ we observe a negative value for $U_C = 9.25$ which is an indication for the breakdown of Landau's Fermi liquid theory in presence of the transition from the metallic state into an insulating one. Nearby, at $U = 9.5$ we again observe a change in the sign of Z which strengthen the point that the transition of Mott metal-to-insulator transition is in the

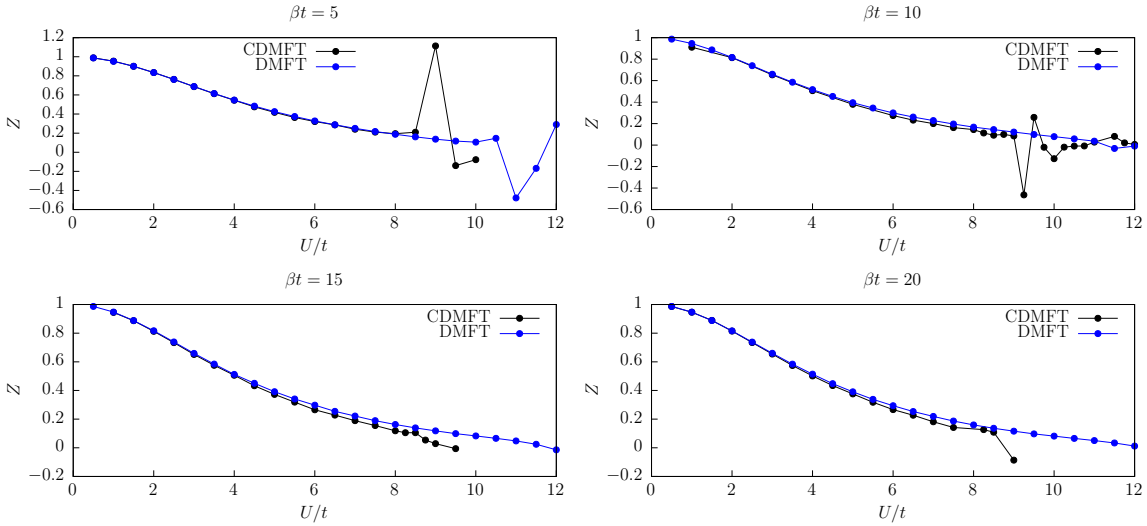

Figure 5.3.: Quasi-particle weight Z of DMFT (blue) and the center site for the seven site cluster (black) for different temperatures.

vicinity. For large interaction values we expect the system to be completely insulating with a quasi-particle weight of 0, which indeed can be observed in figure 5.3. It is clearly visible that the non-local correlations in the seven site cluster are non-vanishing, since otherwise DMFT and CDMFT results would be the same for every interaction. Also here one can see that the quasi-particle weight points to a Mott metal-to-insulator transition appearing at a smaller interaction compared to DMFT.

As stated before the difference of the double occupation d and quasi-particle weight Z between DMFT and CDMFT is directly connected to the non-local correlations in the CDMFT calculation. Non-local in this case means off-diagonal elements of the impurity self-energy. One way to measure the influence of the non-local correlations is to plot the self-energy and the impurity Green's function. Due to symmetry reasons we only show one off-diagonal element of the center to one of his neighbors in figure 5.4. A clear increase in magnitude of the first Matsubara frequency can be seen while lowering the temperature and increasing the interaction U. This result is not surprising, since we expect non-local correlations to be more important in the low temperature regime and the strongly correlated case. For the low temperature calculations $\beta \leq 10$ using interactions U above or in the vicinity of the critical U_c we detect large sign problems, leading to iterations where only $1-5\%$ of the data points can be used to obtain the self-energy during the self-consistency loop. This leads to strong numerical noise, which is especially visible in the off-diagonal part of the self-energy (compare rows for $\beta t = 15, 20$ in figure 5.4). One possible solution to overcome the sign problem is to increase the number of Monte-Carlo cycles in each self-consistency iteration and afterwards measure the self-energy for the converged Weiss field. Nevertheless there is a limit of how low we can go in temperature. The limit is to be found at $\beta t = 20$ at the current state, while for lower temperatures the sign problem gets even worse leading to non-physical negative densities in the first self-consistency loop which makes it impossible to even continue the self-consistency procedure. Besides the off-diagonal part, which has no direct counterpart in the DMFT approach, we can compare the onsite self-energy of the innermost site of the seven site cluster with the (onsite) self-energy found in DMFT. Results are shown in figures 5.5, 5.6 and 5.7.

In general, performing CDMFT calculations on the two-dimensional triangular lattice is

numerically very challenging in terms of computation time. Moreover, the sign problem does not allow for a systematic study of the cluster size dependence. Two-particle properties on the level of the seven-site cluster are in general possible to compute, but are very time consuming and therefore not calculated in this work. In the future it would be an interesting question to address, what will happen if the cluster size increases to the point that the center site is not only surrounded by one shell of neighbors but by two or even three.

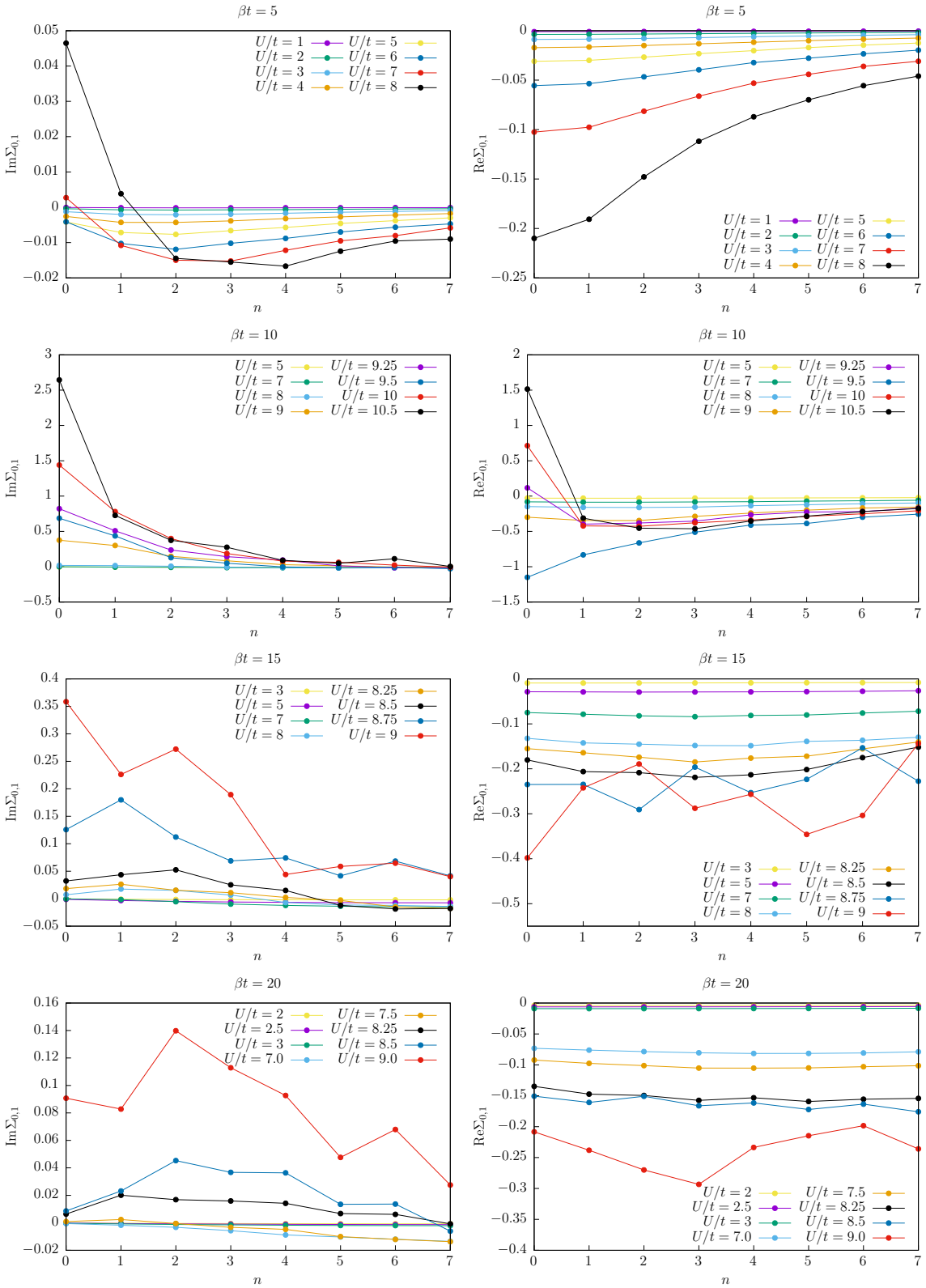

FIGURE 5.4.: Real and imaginary part of the self-energy off-diagonal element $\Sigma_{0,1}$ for the first 8 Matsubara points. Different interaction values U are plotted for the inverse temperatures of $\beta t = 5, 10, 15, 20$.

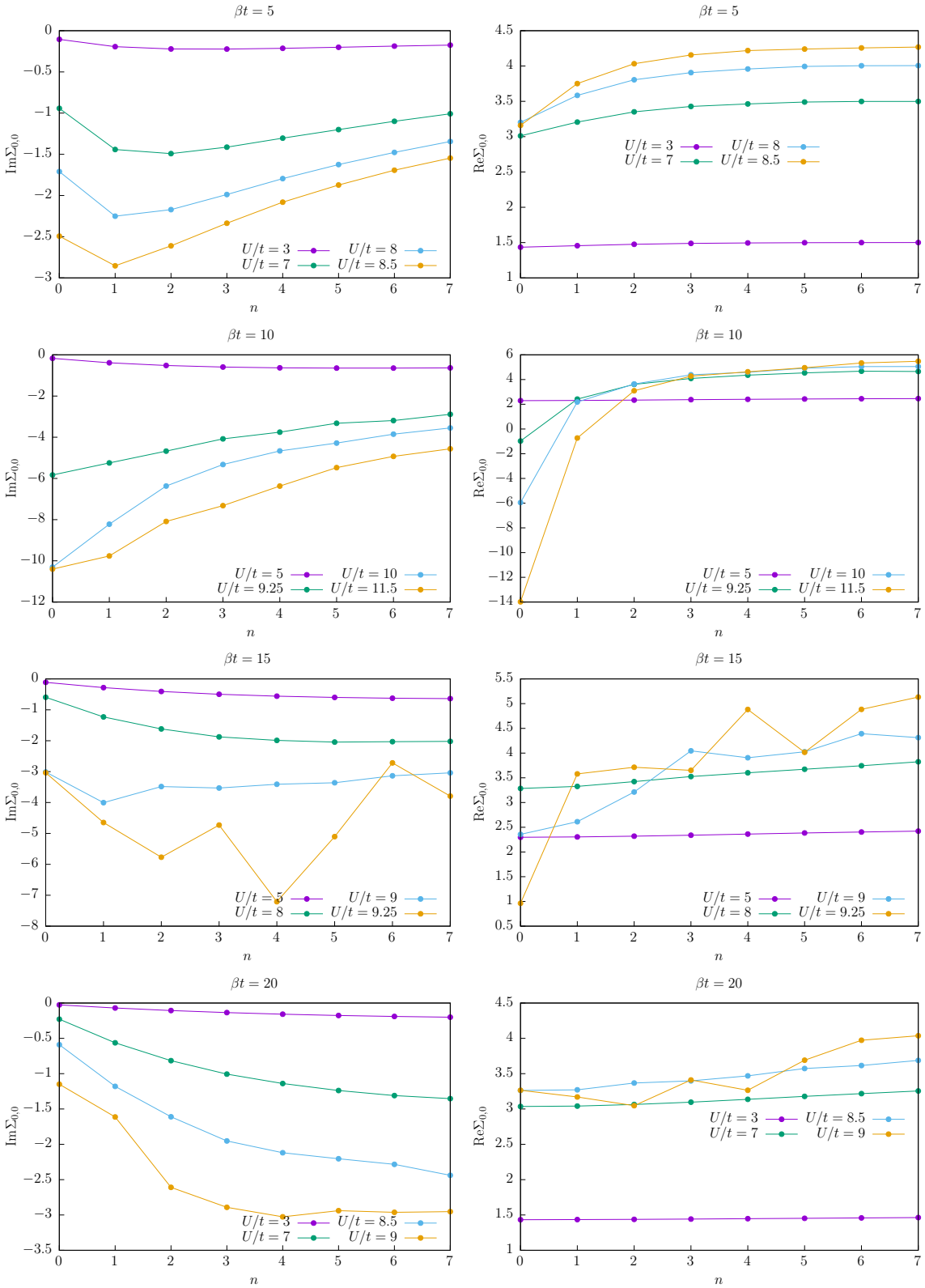

Figure 5.5.: Real and imaginary part of the onsite self-energy element $\Sigma_{0,0}$ for the first 8 Matsubara points. Different interaction values U are plotted for the inverse temperatures of $\beta t = 5, 10, 15, 20$.

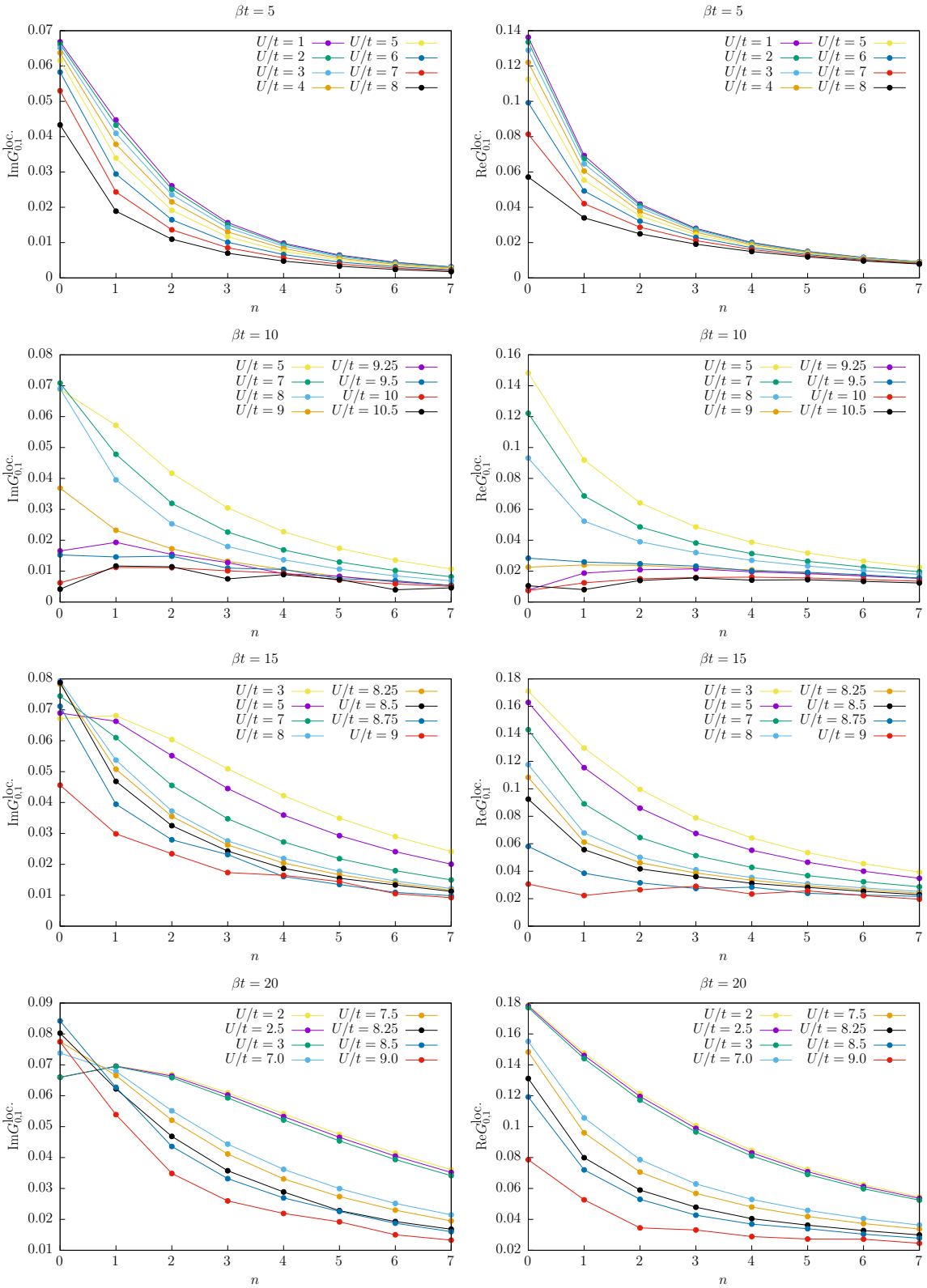

FIGURE 5.6.: Real and imaginary part of the off-diagonal local Green's function $G^{\text{loc.}}_{0,1}$ for the first 8 Matsubara points. Different interaction values U are plotted for the inverse temperatures of $\beta t = 5, 10, 15, 20$.

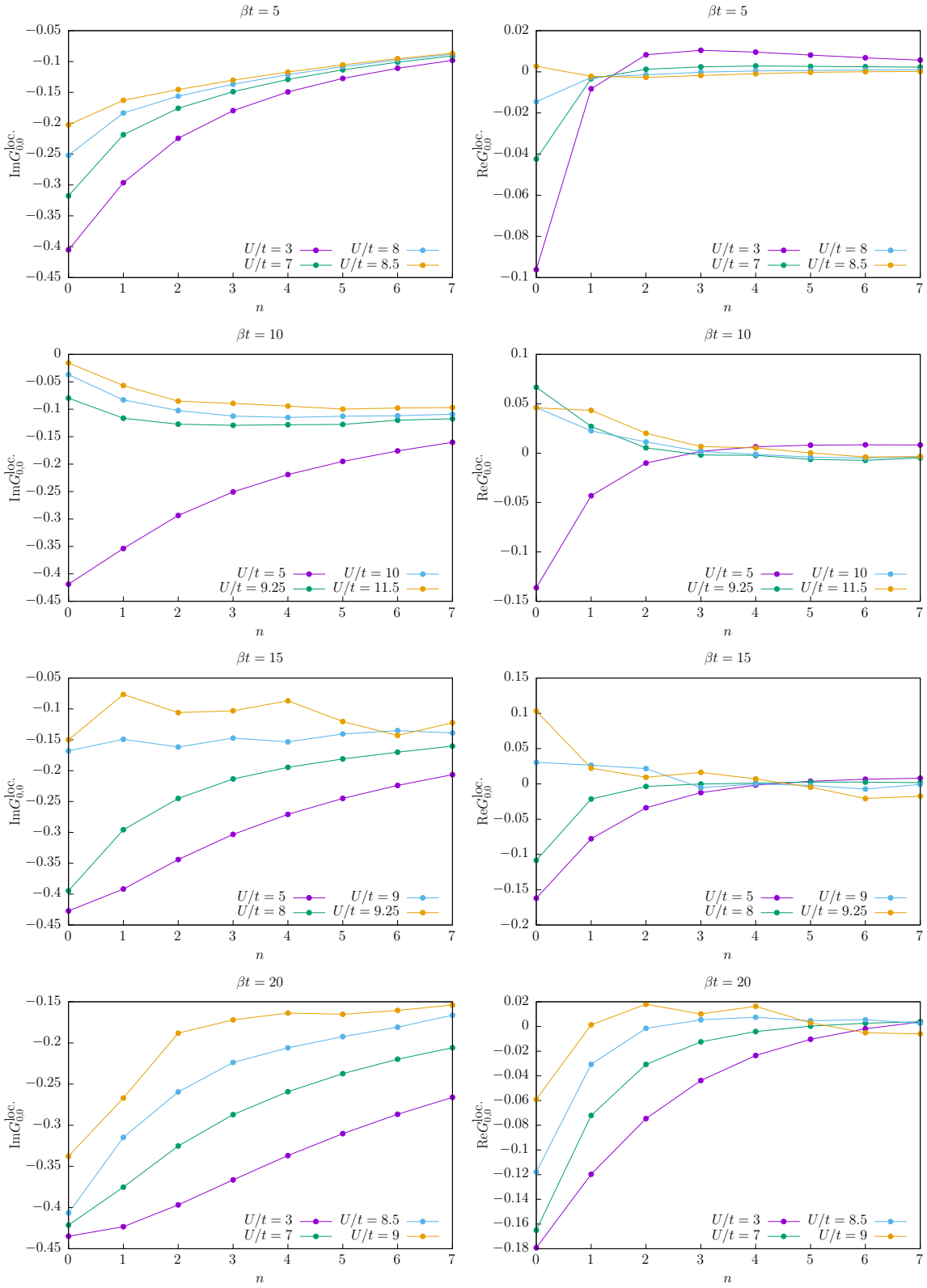

FIGURE 5.7.: Real and imaginary part of the onsite local Green's function $G^{\text{loc.}}_{0,0}$ for the first 8 Matsubara points. Different interaction values U are plotted for the inverse temperatures of $\beta t = 5, 10, 15, 20$.

VI. Summary and outlook

In this work the real-space extension of the DMFT method, namely the cellular dynamical mean-field theory (CDMFT), was used in order to calculate one and two-particle Green's functions. In the first part of this work the classical DMFT method and some general results of the two-dimensional Hubbard model on the square lattice, like the Mott metal-to-insulator transition as well as the artificially arising Nèel temperature are discussed on a single-particle level. Since the DMFT is known to be only an approximate solution in finite dimensions neglecting non-local correlations, we the introduce the CDMFT method. Using different cluster sizes up to 64 total sites, different single-particle quantities like the local spectral function or the self-energy have been computed. Besides their cluster size dependence, also the real-space dependence within the cluster can be assessed. Using a newly developed continuous time interaction (CT-INT) solver of the TRIQS package [60] provides also the possibility to compute dynamic two-particle correlation functions. For the computation of both one- and two-particle quantities, the new idea presented in this work consists in extracting physical quantities for infinite cluster size by introducing the so-called center-focussed extrapolation (cfe). Measuring the real-space distances with respect to the centtral site, the proposed scheme accounts for the broken translational invariance and yields a more accurate lattice Green's function than other known periodization schemes. This has been shown by benchmarking the obtained cfe results with numerically exact diagrammetic Monte Carlo data. Concerning the two-particle quantities the direct measurements of real-space correlations leads to new insights of how the local and non-local parts of correlation functions change while varying the temperature or the interaction value. The last part of this work deals with the two-dimensional triangular lattice in a CDMFT framework, where results for the self-energy and the double occupation are compared with conventional DMFT, illustrating the influence of the non-local self-energy correlations included in CDMFT.

For the future, the newly developed extrapolation method and the access of large clusters hopefully contributes to a renaissance of the CDMFT approach. For the investigation of doped systems, it is further necessary to address the infamous sign problem for the numerical feasability of larger cluster sizes. Besides pushing the numerical aspect of solving the CDMFT self-consistency equation, the CDMFT approach can also be applied to simulate real-space magnetic correlations inside Cu-O planes of the cuprates which exhibit high-T_C superconductivity.

TRIQS CDMFT: A Python application for numerical CDMFT calculations using TRIQS

In the following we provide some details on the numerical implementation of CDMFT. In the beginning of this part we note that the current description of the Python extension is valid for TRIQS versions 2.X and can lead to errors if a former version 1.X or newer versions are used. Besides accessing the TRIQS package [60] the currently not publicly available CT-INT solver is in use, as well as the TRIQS application of the maxent [35]. The following Python packages (which are not directly needed to use the python interface of TRIQS) have to be also installed:

1. SciPy [61]
2. Pandas DataFrame [62, 63]

To use the application in your own Python script you have to source the directory where the python files of TRIQS CDMFT can be found.

```
import sys
sys.path.append('PATH_TO_TRIQS_CDMFT_APPLICATION')
from squarelattice import *
from cfe import *
```

Performing a CDMFT calculation

Up to now this program package only supports CDMFT calculations (of any $N \times N$ cluster) for the two-dimensional square lattice, other lattice geometries are planned but not yet implemented. For every CDMFT calculation one pre processing procedure has to be done, this is to tell the program how the cluster looks. If the grid is not explicitly set by the users the code will take

```
grid = np.arange(N*N).reshape(N,N)
```

as the grid. For the example of $N = 4, 6, 8$ will translate to the following grid structure:

$$g^4 = \begin{bmatrix} 0 & 1 & 2 & 3 \\ 4 & 5 & 6 & 7 \\ 8 & 9 & 10 & 11 \\ 12 & 13 & 14 & 15 \end{bmatrix} \quad g^6 = \begin{bmatrix} 0 & 1 & 2 & 3 & 4 & 5 \\ 6 & 7 & 8 & 9 & 10 & 11 \\ 12 & 13 & 14 & 15 & 16 & 17 \\ 18 & 19 & 20 & 21 & 22 & 23 \\ 24 & 25 & 26 & 27 & 28 & 29 \\ 30 & 31 & 32 & 33 & 34 & 35 \end{bmatrix} \quad g^8 = \begin{bmatrix} 0 & 1 & 2 & 3 & 4 & 5 & 6 & 7 \\ 8 & 9 & 10 & 11 & 12 & 13 & 14 & 15 \\ 16 & 17 & 18 & 19 & 20 & 21 & 22 & 23 \\ 24 & 25 & 26 & 27 & 28 & 29 & 30 & 31 \\ 32 & 33 & 34 & 35 & 36 & 37 & 38 & 39 \\ 40 & 41 & 42 & 43 & 44 & 45 & 46 & 47 \\ 48 & 49 & 50 & 51 & 52 & 53 & 54 & 55 \\ 56 & 57 & 58 & 59 & 60 & 61 & 62 & 63 \end{bmatrix}$$

Using the default grid, the minimal code to start an $N \times N$ CDMFT calculation is given by:

```
dim = N
lattice = squarelattice(dim)
lattice.do_DMFT(beta,U)
```

Besides the size of the cluster N the function do_DMFT takes the two parameters of the inverse temperature β and the interaction U. There are many more optional parameters that can be given to the function

```
do_DMFT(beta,U,DensPerSite=1.0,n_iw = 1050,n_tau=10*1050,
        cont_calc=None,loops=20,delta = 0.1,warmup_cycles = 5000,
        cycles = 100000,Hint = 'Onsite',save_filename=None,
        para=True,symmetry=True,spins=["up","down"],
        length_cycle=150,mixing=0.8,random_seed=[3478,928374],
        max_time = -1,use_double_insertion=True,
        change_delta=True,fix_mu=None):
```

- DensPerSite: Density per site. Default is half-filled, i.e. 1.
- n_iw: Number of Matsubara frequency points used by the solver.
- n_tau: Number of imaginary time points used by the solver. Has to be $n_{\text{iw}} \leq 6 \cdot n_{\text{tau}}$
- cont_calc: Continue calculation from a former calculation. Takes the filename as a string as input and sets the initial self-energy to the most converged self-energy found in the input file.
- loops: Number of self-consistency iterations.
- delta: CT_INT solver parameter δ.
- warmup_cycles: Warmup cycles per iteration.
- cycles: Monte-Carlo cycles per iteration.
- Hint: Interaction Hamilton. Up until now only "Onsite" is available, which represents the onsite Hubbard-interaction of value U on each site.
- save_filename: Setting this to a string S with ending of ".h5" will save the results into the file S. If this parameter is None than the filename consists of "U[U]-beta[beta]-dp[DensPerSite]-[N]x[N].h5".
- para: If true: Enforces paramagnetic self-energy after each iteration ($\Sigma_\uparrow = \Sigma_\downarrow$).
- symmetry: If true: Use rotational symmetry of the cluster to take the mean values of the self-energy matrix which has to be the same in order to preserve the rotational symmetry. Only works if para == True.
- spins: Name of spins used.
- length_cycle: Length cycle used in the CT_INT solver.

- mixing: Mixing factor mix. The self-energy after one iteration is calculated by the following equation:
$$\Sigma = \text{mix} \cdot \Sigma + (1 - \text{mix})\Sigma_{\text{old}} ,$$
where Σ_{old} is the self-energy of the previous iteration (or zero after the first iteration).
- random_seed: Random seed used in the CT_INT solver. In general the random seed for each iteration and rank is calculated by
$$\text{random\_seed}[0] + \text{random\_seed}[1] \cdot (\text{rank} \cdot (\text{iteration} + 1)) .$$
- max_time: Maximum time in seconds for each iteration. Default -1 means unlimited time for one iteration.
- use_double_insertion: Use double_insertion inside the CT_INT solver.
- change_delta: Dynamically change the parameter δ after each iteration if the average sign is bad.
- : fix_mu: Takes a float μ as input. Do a full self-consistency loop with a fixed chemical potential μ.

We now assume that the calculation was successful and the results are saved in the filename "results.h5". We can check the saved results by loading the ".h5" file in a new script.

```
R = HDFArchive("results.h5",'r')
print R
  converged : subgroup
  general_info-converged : subgroup
  info-converged : subgroup
  it0 : subgroup
  it1 : subgroup
  it10 : subgroup
  it11 : subgroup
  it12 : subgroup
  it13 : subgroup
  it2 : subgroup
  it3 : subgroup
  it4 : subgroup
  it5 : subgroup
  it6 : subgroup
  it7 : subgroup
  it8 : subgroup
  it9 : subgroup

print R["converged"]
  HDFArchive with the following content:
  chemical_potential : data
  sigma : subgroup
```

As we can see, every iteration has is own subgroup, inside the subgroup the self-energy and the chemical potential is saved. For the last iteration the "converged" subgroup is created which makes it easier to obtain the converged results without knowing the exact iteration number used in the calculation. Besides the iterations saved in the subgroups "it[loop]" two panda DataFrames are saved. These two data frames are loaded via

```
DF_info   = pd.read_hdf('results.h5',key="info-converged")
DF_general_info   = pd.read_hdf('results.h5',key="general_info-converged")

print DF_general_info.columns.values
['chemical_potential' 'delta' 'iteration' 'sign' 'time']
print DF_general_info.head()
   chemical_potential  delta  iteration  sign        time
0                0.25    0.1        0.0   1.0  119.496750
1                0.25    0.1        1.0   1.0  121.794164
2                0.25    0.1        2.0   1.0  123.067060
3                0.25    0.1        3.0   1.0  121.752869
4                0.25    0.1        4.0   1.0  122.830106


print DF_info.columns.values
['iteration' 'Site' 'Spin' 'Density' 'tau=beta/2' 'Z' 'ScatRate'
'Difference in SE']
print DF_info.head()
  iteration  Site  Spin  ...  Z  ScatRate  Difference in SE
0         0     0    up  ...  1.033558  0.043027          0.237983
1         0     0  down  ...  1.033558  0.043027          0.237983
2         0     1    up  ...  1.034255  0.043425          0.238688
3         0     1  down  ...  1.034255  0.043425          0.238688
4         0     2    up  ...  1.033997  0.043233          0.238675
```

and can be used and manipulated like normal panda DataFrames. In the "general-info" DataFrame the following parameters of each iteration are saved

- Chemical potential μ.
- δ.
- Average sign.
- Time in seconds for each iteration.

The DataFrame "info" contains the following information for each iteration, each spin value and each site

- Density.
- Value of the onsite Green's function at the imaginary time $\tau = \beta/2$ which is an approximation of the spectral function at $\omega = 0$.
- Quasi-particle weight Z.

- Scattering rate Γ.
- Maximum value in difference of the onsite self-energy compared to the former iteration.

Before starting a CDMFT calculation the user can set the starting condition of the self-consistency iterations by either continuing the calculation using a former result, or by setting the self-energy in the beginning by hand in the following way.

```
import sys
sys.path.append('PATH_TO_TRIQS_CDMFT_APPLICATION')
from squarelattice import *
from cfe import *

#example of a 4x4 user defined grid
grid = np.asarray([[4,5,1,2],[3,9,8,10],[0,15,14,13],[6,7,11,12]])
lattice = squarelattice(dim)
lattice.set_grid(grid)
lattice.set_sigma(sigma)
lattice.do_DMFT(beta,U)
```

It is important that the self-energy has the same inverse temperature β, size and lives on the same grid as the following CDMFT calculation. If the grid differs from the default one used in the do_DMFT function, the user is also able to set his default grid.

After successfully converging a self-consistency condition, it is often helpful, especially for large clusters, to measure the self-energy afterwards in order to minimize the numerical noise. Measuring in this sense consists of multiple iterations of calculating the self-energy using the same Weissfield (or self-energy) as input, but varying the random seed in each iteration. A measuring of the self-energy can be obtained with the use of the function:

```
measure_sigma(beta,U,DensPerSite=1.0,n_iw = 1050,n_tau=10*1050,
              cont_calc=None,loops=5,delta = 0.1,warmup_cycles = 5000,
              cycles = 100000,Hint = 'Onsite',para=True,symmetry=True,
              length_cycle=150,mixing=0.8,random_seed=[3478,928374],
              max_time = -1,use_double_insertion=True,fix_mu=None):
```

Where all input parameters are already discussed in the do_DMFT function. In order to use the measure_sigma function it is important to set the parameter "cont_calc" to a file, in which a "converged" subgroup including a self-energy exists.

Measuring two-particle properties

Besides calculating the self-energy using a self-consistency loop it is also possible to calculate two-particle properties in the TRIQS CDMFT package. In particular the spin χ^S_{ij} and charge susceptibility χ^C_{ij}, which can be done in the following way:

```
import sys
sys.path.append('PATH_TO_TRIQS_CDMFT_APPLICATION')
from squarelattice import *
from cfe import *
```

```
lattice = squarelattice(dim)
lattice.set_sigma(sigma)
lattice.two_particle_measure(beta,U,method='center_unique',
                             cont_calc=None,measures=5,
                             delta=0.1,n_iw2 = 11,n_tau2 = 100,
                             warmup_cycles = 5000, cycles = 50000,
                             random_seed=[3478,928374],
                             length_cycle = 150,DensPerSite = 1.0,
                             use_double_insertion = True,
                             max_time = 24*60*60,
                             Hint = 'Onsite',savename=None):
```

Besides the known parameters which are already discussed for the do_DMFT function, a variable called "method" can be set. Up to now they are three possible strings that the parameter "method" can take

- full: Calculate the susceptibility on the whole cluster
$$\sum_{i,j} \chi^{S/C}_{i,j} .$$
- center: Calculate the susceptibility by keeping one site fixed to the center site of the cluster:
$$\sum_{j} \chi^{S/C}_{cs,j} .$$
- center_unique: Calculate the susceptibility by keeping one site fixed to the cluster, but neglect all sites ℓ which would be calculated multiple times due to rotational symmetry of the cluster.
$$\sum_{j\neq\ell} \chi^{S/C}_{cs,j} ,$$

The results gathered during the call of the two_particle_measure are saved for each measurement. The measurements are done by creating the Weiss field using the self-energy given via the input set_sigma. For each measurement the same Weiss field is used, while the random seed is varied. In the output file for each measurement a subgroup is created which includes the following objects:

```
R = HDFArchive("results-chi.h5",'r')
print R

  info2 : subgroup
  it0 : subgroup
  it1 : subgroup
  it2 : subgroup

print R["it2"]
  chi_iw_C : subgroup
  chi_iw_S : subgroup
```

```
  chi_iw_mean_C : subgroup
  chi_iw_mean_S : subgroup
  chi_tau_C : subgroup
  chi_tau_S : subgroup
  chi_tau_mean_C : subgroup
  chi_tau_mean_S : subgroup



DF_info  = pd.read_hdf('results-chi.h5',key="info2")
print DF_info.columns.values
   ['measure' 'site1' 'site2' 'Omega0_C' 'Tau0_C' 'Omega0_S' 'Tau0_S']
```

All objects with the extension of mean are the mean values of all former iterations. Inside the pandas DataFrame one can find information for the susceptibility and the zero frequency value and the zero time point, which can be directly used to calculate the compressibility κ or the static spin-susceptibility.

Post Processing procedures

In the following we show post processing procedures obtained in the TRIQS CDMFT package. We start with the build-in maxent function calling the TRIQS maxent application.

```
do_maxent(g_tau,sigma_error,w_min,
          w_max,w_p,a_p,verb)
```

- g_tau: Imaginary time scalar Green's function. Does not take a Block Green's function nor a matrix valued Green's function as input.
- sigma_error: Error of the input Green's function. Has to be a scalar and is constant for every imaginary time point.
- w_min: Minimum ω value.
- w_max: Maximum ω value.
- a_p: Alpha parameter used inside the maxent application.
- verb: If True then show output information of maxent. If False no output is given during the process of obtaining the spectral function.

Besides producing a local spectral function one can also produce lattice self-energies for converged cluster self-energies

```
def get_lattice_gf(sigma,grid,kx,ky,mu,method='cf',
                   e=0.0,t=-0.25,tp=0.0):
```

for different methods. Each method takes the self-energy and the grid on which this self-energy was calculated as input. The methods which can be used to get the lattice self-energy are

the "default" periodization of the self-energy, the "cumulant" periodization and the so-called center-focused periodization "cf" which includes only the center-site and all the real-space connections to the center-site.

Since it is often interesting to look at the spectral function of the lattice Green's function on a given k-path, there exists a function, which is parallelized to obtain this k-dependent spectral function:

```
get_spectral_function_kpath(sigma, grid, mu, k_path, n_tau=10000,
                            method='cf', e=0.0, t=-0.25, tp=0.0,
                            sigma_error=1e-3, w_min=-5.0, w_max=5.0,
                            w_p=751, a_p=30, verb=False, save=None):
```

The parameters in use are self explanatory, where "k_path" is a list of all k-points of the following shape:

$$\text{k\_path} = [[k_x^0, k_y^0, 0], \ldots, [k_x^N, k_y^N, N]]$$

The additional parameter N, is the count which is used to identify the N-th (k_x, k_y)-point. An example code for the 4×4 cluster, using the parameters of $\beta = 20, U = 1$ and choosing the "cf" method, is shown

```
get_spectral_function_kpath(sigma, grid, mu, k_path, n_tau=10000,
                            method='cf', e=0.0, t=-0.25, tp=0.0,
                            sigma_error=1e-3, w_min=-5.0, w_max=5.0,
                            w_p=751, a_p=30, verb=False, save=None):
```

which leads to the output figure of

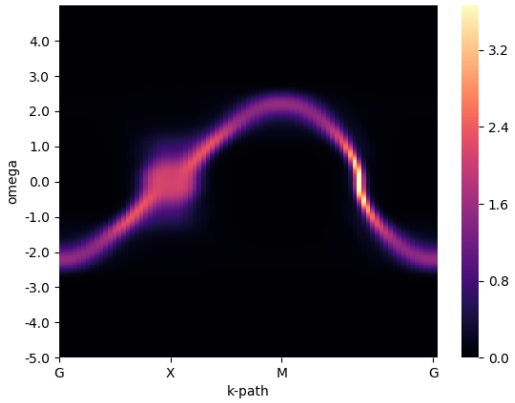

In order to extrapolate self-energies and susceptibilities (or any other object), as function called do_extrapolation_full is available. This function is fully parallelized using mpi4py.

```
do_extrapolation_full(GFs, grids, npoints=None)
```

The input of the function can be either a bosonic or fermionic, matrix valued Green's function (no block Green's function can be given as an input parameter). It is important that for the fermionic case the extrapolation function assumes that the two spin directions $\uparrow, \downarrow$ exist and are equal. In general the input parameters are the following:

- GFs: List of (at least two) bosonic/fermionic matrix valued Green's function (does not work for block Green's functions).

- grids: List of grids. The entries of the list has to be in the same order as in the GFs list.
- npoints: If None, do the extrapolation for all frequencies
- Returns: For a fermionic input returns a block Green's function of the maximum grid size given in the grids input, where the spin indices $\uparrow, \downarrow$ are assumed to be equal. For a bosonic input of Green's function returns a bosonic Green's function with the maximum grid size found in grids.

Bibliography

[1] A. Georges, G. Kotliar, W. Krauth, and M. J. Rozenberg, "Dynamical mean-field theory of strongly correlated fermion systems and the limit of infinite dimensions", Rev. Mod. Phys. **68**, 13–125 (1996).

[2] G. Kotliar and D. Vollhardt, "Strongly Correlated Materials: Insights From Dynamical Mean-Field Theory", Physics Today **57**, 53–59 (2004).

[3] T. A. Maier, M. Jarrell, T. Pruschke, and M. H. Hettler, "Quantum cluster theories", Rev. Mod. Phys. **77**, 1027–1080 (2005).

[4] A. Toschi, A. A. Katanin, and K. Held, "Dynamical vertex approximation: a step beyond dynamical mean-field theory", Phys. Rev. B **75**, 045118 (2007).

[5] A. A. Katanin, A. Toschi, and K. Held, "Comparing pertinent effects of antiferromagnetic fluctuations in the two- and three-dimensional hubbard model", Phys. Rev. B **80**, 075104 (2009).

[6] G. Rohringer, A. Toschi, A. Katanin, and K. Held, "Critical properties of the half-filled hubbard model in three dimensions", Phys. Rev. Lett. **107**, 256402 (2011).

[7] T. Schäfer, F. Geles, D. Rost, G. Rohringer, E. Arrigoni, K. Held, N. Blümer, M. Aichhorn, and A. Toschi, "Fate of the false mott-hubbard transition in two dimensions", Phys. Rev. B **91**, 125109 (2015).

[8] T. Schäfer, A. Toschi, and K. Held, "Dynamical vertex approximation for the two-dimensional hubbard model", Journal of Magnetism and Magnetic Materials **400**, 107–111 (2016).

[9] A. N. Rubtsov, M. I. Katsnelson, and A. I. Lichtenstein, "Dual fermion approach to nonlocal correlations in the hubbard model", Phys. Rev. B **77**, 033101 (2008).

[10] H. Hafermann, G. Li, A. N. Rubtsov, M. I. Katsnelson, A. I. Lichtenstein, and H. Monien, "Efficient perturbation theory for quantum lattice models", Phys. Rev. Lett. **102**, 206401 (2009).

[11] S.-X. Yang, H. Fotso, H. Hafermann, K.-M. Tam, J. Moreno, T. Pruschke, and M. Jarrell, "Dual fermion dynamical cluster approach for strongly correlated systems", Phys. Rev. B **84**, 155106 (2011).

[12] E. A. Stepanov, E. G. C. P. van Loon, A. A. Katanin, A. I. Lichtenstein, M. I. Katsnelson, and A. N. Rubtsov, "Self-consistent dual boson approach to single-particle and collective excitations in correlated systems", Phys. Rev. B **93**, 045107 (2016).

[13] G. Rohringer, A. Toschi, H. Hafermann, K. Held, V. I. Anisimov, and A. A. Katanin, "One-particle irreducible functional approach: a route to diagrammatic extensions of the dynamical mean-field theory", Phys. Rev. B **88**, 115112 (2013).

[14] J. P. Hague, M. Jarrell, and T. C. Schulthess, "Fluctuation-exchange supplemented quantum monte carlo approach to the hubbard model", Phys. Rev. B **69**, 165113 (2004).

[15] C. Taranto, S. Andergassen, J. Bauer, K. Held, A. Katanin, W. Metzner, G. Rohringer, and A. Toschi, "From infinite to two dimensions through the functional renormalization group", Phys. Rev. Lett. **112**, 196402 (2014).

[16] C. Slezak, M. Jarrell, T. Maier, and J. Deisz, "Multi-scale extensions to quantum cluster methods for strongly correlated electron systems", Journal of Physics: Condensed Matter **21**, 435604 (2009).

[17] T. Ayral and O. Parcollet, "Mott physics and spin fluctuations: a unified framework", Phys. Rev. B **92**, 115109 (2015).

[18] T. Ayral and O. Parcollet, "Mott physics and spin fluctuations: a functional viewpoint", Phys. Rev. B **93**, 235124 (2016).

[19] T. Ayral and O. Parcollet, "Mott physics and collective modes: an atomic approximation of the four-particle irreducible functional", Phys. Rev. B **94**, 075159 (2016).

[20] J. Vu či čevi ć, T. Ayral, and O. Parcollet, "Trilex and *gw*+edmft approach to *d*-wave superconductivity in the hubbard model", Phys. Rev. B **96**, 104504 (2017).

[21] T. Ayral, J. Vu či čevi ć, and O. Parcollet, "Fierz convergence criterion: a controlled approach to strongly interacting systems with small embedded clusters", Phys. Rev. Lett. **119**, 166401 (2017).

[22] M. H. Hettler, A. N. Tahvildar-Zadeh, M. Jarrell, T. Pruschke, and H. R. Krishnamurthy, "Nonlocal dynamical correlations of strongly interacting electron systems", Phys. Rev. B **58**, R7475–R7479 (1998).

[23] M. H. Hettler, M. Mukherjee, M. Jarrell, and H. R. Krishnamurthy, "Dynamical cluster approximation: nonlocal dynamics of correlated electron systems", Phys. Rev. B **61**, 12739–12756 (2000).

[24] K. Aryanpour, M. H. Hettler, and M. Jarrell, "Analysis of the dynamical cluster approximation for the hubbard model", Phys. Rev. B **65**, 153102 (2002).

[25] A. I. Lichtenstein and M. I. Katsnelson, "Antiferromagnetism and d-wave superconductivity in cuprates: a cluster dynamical mean-field theory", Phys. Rev. B **62**, R9283–R9286 (2000).

[26] G. Kotliar, S. Y. Savrasov, G. Pálsson, and G. Biroli, "Cellular dynamical mean field approach to strongly correlated systems", Phys. Rev. Lett. **87**, 186401 (2001).

[27] A. Liebsch, H. Ishida, and J. Merino, "Multisite versus multiorbital coulomb correlations studied within finite-temperature exact diagonalization dynamical mean-field theory", Phys. Rev. B **78**, 165123 (2008).

[28] M. Klett, N. Wentzell, T. Schäfer, F. S. IV, O. Parcollet, S. Andergassen, and P. Hansmann, *Real-space cluster dynamical mean-field theory: center focused extrapolation on the one- and two particle level*, 2020.

[29] J. Hubbard, "Electron correlations in narrow energy bands", Proceedings of the Royal Society of London. Series A, Mathematical and Physical Sciences **276**, 238–257 (1963).

[30] N. Marzari, A. A. Mostofi, J. R. Yates, I. Souza, and D. Vanderbilt, "Maximally localized wannier functions: theory and applications", Rev. Mod. Phys. **84**, 1419–1475 (2012).

[31] G. H. Wannier, "The structure of electronic excitation levels in insulating crystals", Phys. Rev. **52**, 191–197 (1937).

[32] E. Gull, A. J. Millis, A. I. Lichtenstein, A. N. Rubtsov, M. Troyer, and P. Werner, "Continuous-time monte carlo methods for quantum impurity models", Rev. Mod. Phys. **83**, 349–404 (2011).

[33] A. N. Rubtsov, V. V. Savkin, and A. I. Lichtenstein, "Continuous-time quantum monte carlo method for fermions", Phys. Rev. B **72**, 035122 (2005).

[34] M. Troyer and U.-J. Wiese, "Computational complexity and fundamental limitations to fermionic quantum monte carlo simulations", Phys. Rev. Lett. **94**, 170201 (2005).

[35] G. J. Kraberger, R. Triebl, M. Zingl, and M. Aichhorn, "Maximum entropy formalism for the analytic continuation of matrix-valued green's functions", Phys. Rev. B **96**, 155128 (2017).

[36] R. N. Silver, D. S. Sivia, and J. E. Gubernatis, "Maximum-entropy method for analytic continuation of quantum monte carlo data", Phys. Rev. B **41**, 2380–2389 (1990).

[37] J. E. Gubernatis, M. Jarrell, R. N. Silver, and D. S. Sivia, "Quantum monte carlo simulations and maximum entropy: dynamics from imaginary-time data", Phys. Rev. B **44**, 6011–6029 (1991).

[38] F. Bao, Y. Tang, M. Summers, G. Zhang, C. Webster, V. Scarola, and T. A. Maier, "Fast and efficient stochastic optimization for analytic continuation", Phys. Rev. B **94**, 125149 (2016).

[39] C. E. Creffield, E. G. Klepfish, E. R. Pike, and S. Sarkar, "Spectral weight function for the half-filled hubbard model: a singular value decomposition approach", Phys. Rev. Lett. **75**, 517–520 (1995).

[40] L.-F. Arsenault, R. Neuberg, L. A. Hannah, and A. J. Millis, "Projected regression method for solving fredholm integral equations arising in the analytic continuation problem of quantum physics", Inverse Problems **33**, 115007 (2017).

[41] A. W. Sandvik, "Stochastic method for analytic continuation of quantum monte carlo data", Phys. Rev. B **57**, 10287–10290 (1998).

[42] K. S. D. Beach, *Identifying the maximum entropy method as a special limit of stochastic analytic continuation*, 2004.

[43] A. S. Mishchenko, N. V. Prokof'ev, A. Sakamoto, and B. V. Svistunov, "Diagrammatic quantum monte carlo study of the fröhlich polaron", Phys. Rev. B **62**, 6317–6336 (2000).

[44] S. Fuchs, T. Pruschke, and M. Jarrell, "Analytic continuation of quantum monte carlo data by stochastic analytical inference", Phys. Rev. E **81**, 056701 (2010).

[45] A. W. Sandvik, "Constrained sampling method for analytic continuation", Phys. Rev. E **94**, 063308 (2016).

[46] K. S. D. Beach, R. J. Gooding, and F. Marsiglio, "Reliable padé analytical continuation method based on a high-accuracy symbolic computation algorithm", Phys. Rev. B **61**, 5147–5157 (2000).

[47] J. Skilling, *Maximum entropy and bayesian methods* (Springer, 1989).

[48] P. Wölfle, "Quasiparticles in condensed matter systems", Reports on Progress in Physics **81**, 032501 (2018).

[49] R. Žitko, D. Hansen, E. Perepelitsky, J. Mravlje, A. Georges, and B. S. Shastry, "Extremely correlated fermi liquid theory meets dynamical mean-field theory: analytical insights into the doping-driven mott transition", Phys. Rev. B **88**, 235132 (2013).

[50] G. Biroli, O. Parcollet, and G. Kotliar, "Cluster dynamical mean-field theories: causality and classical limit", Phys. Rev. B **69**, 205108 (2004).

[51] A. Fuhrmann, S. Okamoto, H. Monien, and A. J. Millis, "Fictive-impurity approach to dynamical mean-field theory: a strong-coupling investigation", Phys. Rev. B **75**, 205118 (2007).

[52] S. Sakai, G. Sangiovanni, M. Civelli, Y. Motome, K. Held, and M. Imada, "Cluster-size dependence in cellular dynamical mean-field theory", Phys. Rev. B **85**, 035102 (2012).

[53] T. Schäfer, A. Toschi, and K. Held, "Dynamical vertex approximation for the two-dimensional hubbard model", Journal of Magnetism and Magnetic Materials **400**, Proceedings of the 20th International Conference on Magnetism (Barcelona) 5-10 July 2015, 107–111 (2016).

[54] T. Schäfer, F. Geles, D. Rost, G. Rohringer, E. Arrigoni, K. Held, N. Blümer, M. Aichhorn, and A. Toschi, "Fate of the false mott-hubbard transition in two dimensions", Phys. Rev. B **91**, 125109 (2015).

[55] F. Šimkovic, J. P. F. LeBlanc, A. J. Kim, Y. Deng, N. V. Prokof'ev, B. V. Svistunov, and E. Kozik, "Extended crossover from a fermi liquid to a quasiantiferromagnet in the half-filled 2d hubbard model", Phys. Rev. Lett. **124**, 017003 (2020).

[56] A. J. Kim, F. S. IV, and E. Kozik, "Spin and charge correlations across the metal-to-insulator crossover in the half-filled 2*d* hubbard model", 10.1103/PhysRevLett.124.117602 (2019).

[57] S. R. White, D. J. Scalapino, R. L. Sugar, E. Y. Loh, J. E. Gubernatis, and R. T. Scalettar, "Numerical study of the two-dimensional hubbard model", Phys. Rev. B **40**, 506–516 (1989).

[58] M. P. Das, K. I. Golden, and F. Green, "Compressibility sum rule for the two-dimensional electron gas", Phys. Rev. E **64**, 012103 (2001).

[59] T. Schäfer, N. Wentzell, F. Š. IV, Y.-Y. He, C. Hille, M. Klett, C. J. Eckhardt, B. Arzhang, V. Harkov, F.-M. L. Régent, A. Kirsch, Y. Wang, A. J. Kim, E. Kozik, E. A. Stepanov, A. Kauch, S. Andergassen, P. Hansmann, D. Rohe, Y. M. Vilk, J. P. F. LeBlanc, S. Zhang, A. .-M. S. Tremblay, M. Ferrero, O. Parcollet, and A. Georges, "Tracking the footprints of spin fluctuations: a multi-method, multi-messenger study of the two-dimensional hubbard model", (2020).

[60] O. Parcollet, M. Ferrero, T. Ayral, H. Hafermann, I. Krivenko, L. Messio, and P. Seth, "Triqs: a toolbox for research on interacting quantum systems", Computer Physics Communications **196**, 398–415 (2015).

[61] P. Virtanen, R. Gommers, T. E. Oliphant, M. Haberland, T. Reddy, D. Cournapeau, E. Burovski, P. Peterson, W. Weckesser, J. Bright, S. J. van der Walt, M. Brett, J. Wilson, K. Jarrod Millman, N. Mayorov, A. R. J. Nelson, E. Jones, R. Kern, E. Larson, C. Carey, İ. Polat, Y. Feng, E. W. Moore, J. Vand erPlas, D. Laxalde, J. Perktold, R. Cimrman, I. Henriksen, E. A. Quintero, C. R. Harris, A. M. Archibald, A. H. Ribeiro, F. Pedregosa, P. van Mulbregt, and S. 1. 0. Contributors, "SciPy 1.0: Fundamental Algorithms for Scientific Computing in Python", Nature Methods **17**, 261–272 (2020).

[62] T. pandas development team, "Pandas-dev/pandas: pandas", version latest, 10.5281/zenodo.3509134 (2020).

[63] W. McKinney, “Data Structures for Statistical Computing in Python”, edited by S. van der Walt and J. Millman, 56–61 (2010).